RICE UNIVERSITY

Measuring Dynamic Membrane Mechanical Properties Using a Combined Microfabricated Magnetic Force Transducer-Microaspiration System

by

Daniel Joshua Benedict Stark

A Thesis Submitted
in Partial Fulfillment of the
Requirements for the Degree

Doctor of Philosophy

Approved, Thesis Committee:

Thomas C. Killian, Chair
Professor of Physics and Astronomy

Robert M. Raphael, Thesis Advisor
Associate Professor of Bioengineering

Jason H. Hafner
Associate Professor of Physics and Astronomy and Associate Professor of Chemistry

---

Christy F. Landes
Norman Hackerman-Welch Young Investigator Assistant Professor of Chemistry

Houston, Texas

August, 2011

Abstract

Measuring Dynamic Membrane Mechanical Properties Using a Combined Microfabricated Magnetic Force Transducer-Microaspiration System

by

Daniel Joshua Benedict Stark

This thesis examines the dynamics of the formation of tethers, which are tubes of lipids $20 - 200\,\text{nm}$ in diameter. In particular, this work investigates how the loading rate affects the observed threshold force at which a tether forms from a vesicle membrane. Tether dynamics are important to a myriad of biological processes such as signaling when white blood cells adhere to the walls of healthy and diseased blood vessels, or in the transport of intracellular material between neighboring cells. To understand the dynamics of tether formation in such systems more fully, the studies presented in this thesis focus on the dependence of the force needed to create a tether on the rate of force change. To conduct these experiments, I combined, for the first time, a microfabricated magnetic force transducer, or a microscale device that generates well-controlled and localized magnetic fields, and microaspiration, a technique to apply known tension to a lipid membrane. Using the combined global and local mechanical control of the joint system, I discovered a strong correlation

between the threshold force of tether formation and the applied force ramp. An energy model, based upon that used to describe membrane rupture, characterized the observed dependencies and provided a mechanism to examine physically relevant quantities within the system. The usefulness of this combined approach was further substantiated by determining the influence of membrane modulators, including cholesterol, tension, adhesion site concentration, and phosphatidylserine, on the dependence seen between force threshold and force rates. Additionally, application of the experimental technique developed in this thesis led to the calculation of the interlayer drag coefficient between membrane leaflets and to the first measurements of the thermal expansivity in aspirated 1-stearoyl-2-oleoyl-*sn*-glycero-3-phosphatidylcholine vesicles. This new tool for dynamic studies of membrane mechanics may further be extended to study how tethers form off of flowing cells or how phase regimes, induced by the presence of cholesterol, influence membrane dynamics.

To my loving family and dear friends.

Acknowledgements

I thank my God always when I remember you in my prayers, because I hear of your love and of the faith which you have toward the Lord Jesus and all the saints, and I pray that the sharing of your faith may promote the knowledge of all the good that is ours in Christ. - Phil 1:4-7 [1, p. 411]

ACKNOWLEDGEMENTS are the one section of the PhD dissertation fit for expressing gratitude for all the support received while preparing a PhD thesis. Below, I intend to take advantage of this honor since I have enjoyed much help over the years. Much help indeed.

First and foremost, I owe much to G__, in all three persons: the Father, the Son, and the Holy Spirit. The Father created me; the Son redeemed me; and the Spirit renewed me. Saint Benedict of Nursia, my patron saint, has, by the Lord, helped to bring *pax* and *ora et labora* to my life. I pray that the Lord will help me find the peace to hear His Word, the Wisdom to understand, and the strength to follow.

I also owe much to Professors Thomas Killian and Robert Raphael, my co-advisors. Not only have both had great patience with me, but both have also given good advice in the scientific and personal realms. They have driven me to do my best. Further, I am immensely grateful that they have diverted so much of their time, consideration, energy, and money to my several projects. Addiitonally, I would like to thank the rest of the members of my committees: Professors Jason Hafner, Christy Landes, and

Matthew Baring. Professors Hafner and Landes have provided useful guidance on this thesis, and Professors Hafner and Baring have both given good advice over the years as members of my departmental committee.

My parents, Josh and Susan Stark, have encouraged me over the years and given me strength whenever needed. During my brief visits to Chicago, Los Angeles, Covedale, and Cocoa Beach, the rest of my family—my sister Sarah, aunts Jean, Mary, and Nancy, uncles Alan and Henry, and cousins Alexandra, Christopher, Nicholas, and Rebecca, grandparents Gustav, Rita, Roland, Vera—heartened my heart, mind, and soul and amplified the joy in my life. Regardless of how lonely I could get, I have felt loved by my family, and for that, I am truly thankful.

Providing support, great conversations, and adventures, my close friends have been essential to my sanity. Sarah Nagel has always been concerned and acted as a sounding board. She also introduced me to her relatives, including Dave and Jonathan, and some very interesting and fun friends of hers, such as Alexis, Chad and DeeDee, Mr. Jerry, and Amy and Jason. I wish her a very happy life. Pascal Mickelson is a wonderful conversationalist and has been there when I have needed him, without question. He has also involved me in his life, including adventures with linguists and botanists. He is a good man. Jan-Willem van de Meent, Sharon Doku, and Fei Xu let me vent to them. Michael Foss, Leonard Chan, Russell Schafer and Scott Esterholm ensured I understood the value of fraternal friendship. William Rice, Kristjan Stone, Luke Boyer, Michael Dirk, Jared Day, Jayme Yeo, and Yuan Ji remembered me, even

when I was doing my best to be anti-social. Finally, Anna Cragin née Stupina and Yunchiu Chang made being ten fun again, with some slight help of Dave and Buster.

In addition to those above that supported me proactively, many others have also fortified me throughout the years. The other students in Physics, notably Britain Willingham, Victoria Astley, and Asher Pembroke, gave humor and support throughout the years. Additionally, several organizations endured my rather inconsistent attendance with ever-welcoming grins and grounded me in at least some aspects of the rest of society. Those at the Catholic Student Association worked to expand my faith and community. The Graduate Student Association and Rotaract of River Oaks provided an outlet for me to give back to society while also appreciating who I am. The members of the Southeast Texas/Houston Chapter of the Fulbright Association imparted perspective, wisdom, and international connections. The last organization I would like to thank is the Rice Sailing Team for sharing the excitement of the waves and the wind with me the occasional times I was able to partake.

I also wish to express my gratitude to the administrators in both the Physics and Bioengineering Departments and the Gulf Coast Consortia for not only handling all the paperwork involving me, which I know was complicated given my delocalized nature between the two departments and the Consortia, but also for being generous with friendly smiles. Chiefly, Maria Melendez, Lisa Boykin, Barbara Braun, Bridgitt Ayers, Umbe Cantú, Angela Collman, Melissa Gluck, and Amy Jackson were especially gregarious.

In addition to the social support I have received over the past few years. I have also had much scientific support. The members of both the Killian Lab and the Raphael Lab have helped me tremendously. My lab-mates in the Killian Lab—Jose Castro, Brian DeSalvo, Hong Gao, Priya Gupta, Sampad Laha, Natali Martinez, Patrick McQuillen, Pascal Mickelson, Sarah Nagel, Clayton Simien, and Mi Yan—contributed greatly to helping me pass several of Rice's physics courses, to developing the electronic supply used for the devices outlined in this thesis, to implementing some key functionality in the LabView control program, and in machining parts. My lab-mates in the Raphael Lab—Guillaume Duret, Emily Glassinger, Jenni Greeson, Ramsey Kamar, Ryan McGuire, Chance Mooney, Louise Organ, Imran Quraishi, and Yong Zhou—have educated me in several microscopic techniques and helped with discussions over membrane mechanics and experimental interpretation. My work at Rice furthermore received much assistance from various collaborators. Professor Lisa Biswal in Chemical Engineering facilitated my learning of microfluidics and has been a consistent confidante throughout the years. Doctors Laurence Cooper and Dean Lee in Pediatric Oncology at M. D. Anderson Cancer Center elucidated flow cytometry along with motivating the electroporation project*. Professors Ka-Yiu San and Joel Moake graciously gave access to their respective flow cytometers for poration studies. Finally, I wish to thank David Lee and Doctors Souza and Carly Levin of Nano3D Biosciences for involving me in their exciting magnetic levitation cell culturing project

*The electroporation and magnetic levitation cell culturing projects are not reviewed in this thesis.

and for so much moral support.

My multiple projects would have come to no avail without funding. Luckily, multiple organizations have seen fit to provide monies for my work. The National Science Foundation gave support through the Graduate Research Fellowship; and the Hamill Innovation Grant—initially drafted by Doctor David Holtzclaw—funded much of the preliminary supplies and equipment. The National Institutes of Health financed my work through two training grants: the Nanobiology Training Program (NIH Grant No. T90 DK70121) and the Houston Area Membrane Biophysics Program (T90 DK70121-04), both of which were administered by the W. M. Keck Center for Interdisciplinary Bioscience Training of the Gulf Coast Consortia. In addition to the funding, the people I have met through these programs, particularly Carmen Reznik and Nam Tonthat, have let to my greater understanding of biophysics.

And last but certainly not least, I would like to express my deepest gratitude to the graduate student and undergraduate students that progressed my projects while working directly under me. Their hard work, good ideas, and companionship certainly sped my projects along. Nan Du and Laura Timmerman assisted tremendously on the electroporation project. Shinji Strain was a model summer student that drove the magnetic studies on membrane projection. Finally, Peter Borden pushed at the end to investigate the last interesting results, many of which are included in this work.

To all those that have helped me during my tenure at Rice University, *thank you*.

Contents

Abstract ii

Acknowledgements iv

Table of Contents x

List of Tables xvii

List of Figures xviii

List of Equations xxi

Nomenclature xxv

1 An Introduction 1

2 A Membrane Mechanics Primer 6

2.1 Membrane Composition 6

2.1.1 Non-lipid Membrane Components 7

2.1.2 Lipids 7

2.2 Mechanical Properties of Membrane 12

2.2.1 Normal and Gaussian Curvatures 14

2.2.2 Spontaneous Curvature 18

2.2.3 Compressibility 23

2.2.4 Mechanics Applied to Microaspiration 26

2.2.5 Tether Mechanics 28

2.3 Translating Energy Surfaces into Observables 33

2.4 Summary 41

3 Review of Various Magnetic Force Applicators 43

3.1 Macroscopic Permanent Magnets 43

3.2 Macroscopic Magnetic Tweezers 45

3.3 Microfabricated Magnetic Tweezers 48

3.4 Microfabricated Electromagnet Wires 51

4 Microfabrication of a Magnetic Force Transducer 53

4.1 Materials 54

4.1.1 Resists 54

4.1.2 Substrate 55

4.1.3 Metals 56

4.1.4 Photolithographic Mask 56

4.1.5 Fluid Chamber 58

4.1.6 Electrical Connections 58

4.2 Methods 59

4.2.1 Cleaning the Substrate 59

4.2.2 Evaporating 60
4.2.3 Spinning 63
4.2.4 Soft-baking 64
4.2.5 Exposing 64
4.2.5.1 Alignment 66
4.2.5.2 Timing 67
4.2.6 Post-Exposure Bake 68
4.2.7 Developing 70
4.2.8 Electroplating 70
4.2.9 Lift-off and Etch 73
4.3 The MFT Device 75

5 A Microfabricated Magnetic Force Transducer-Microaspiration System for Studying Membrane Mechanics 78

5.1 Abstract 78
5.2 Introduction 79
5.3 Materials and Methods 82
5.3.1 Magnetic Force Transducer Fabrication 82
5.3.2 Vesicle Formation 84
5.3.3 Magnetic Bead Composition 85
5.3.4 Vesicle Aspiration 86
5.3.5 Force Calibration of MFT 86

5.3.6 Thermal Characterization of the MFT 89
5.3.6.1 Finite Element Modeling 89
5.3.6.2 Membrane Thermoelasticity 90
5.3.7 Tether Studies 91
5.4 Results and Discussion 91
5.4.1 Force Calibration 91
5.4.2 Membrane Thermoelasticity 95
5.4.3 Membrane Tether Formation and Dynamics 99
5.5 Summary 103

6 The Use of a Micromagnetic Tweezer to Study the Dynamics of Tether Formation 105

6.1 Abstract 105
6.2 Introduction 106
6.3 Materials and Methods 109
6.3.1 Magnetic Force Transducer Fabrication 110
6.3.2 Vesicle Formation 110
6.3.3 Magnetic Bead Composition 111
6.3.4 Vesicle Aspiration 111
6.3.5 Temperature of the System due to Ramping 112
6.3.6 Formation of a Tether 114
6.4 Results and Discussion 116

6.4.1 On the Dependence between Force Threshold and Rate of Applied Force . . . 116
6.4.2 Verification of the Force Threshold-Force Rate Dependence . . 119
6.4.3 A One Barrier Energy Model . . . 123
6.4.4 A Two Well Energy Model . . . 128
6.5 Improvements . . . 131
6.6 Outstanding Questions . . . 133
6.7 Summary . . . 135

7 Investigating the Effect of Modifiers on Tether Formation Dynamics 136

7.1 Introduction . . . 137
7.2 Materials and Methods . . . 138
7.2.1 Lipids . . . 139
7.2.2 Humidity Chamber . . . 139
7.2.3 Solution Chamber . . . 140
7.2.4 Tension Determination . . . 141
7.2.5 Tethering Protocol . . . 143
7.3 The Effects of Membrane Modifiers on Tether Formation . . . 144
7.3.1 Cholesterol . . . 144
7.3.2 Tension . . . 155
7.3.3 Biotin Concentration . . . 159

7.3.4 SOPS 164

7.4 Improvements 168

7.5 Summary 169

8 Concluding Remarks and Future Work **171**

Bibliography **174**

A Vesicle Making Protocol **193**

A.1 Stock solutions 193

A.2 Cleaning 196

A.3 Lipid Desiccation 197

A.4 Electroformation 197

A.5 Storage 199

B Numerical Modeling with COMSOL **201**

B.1 Governing Relations 202

B.2 Material Properties 202

B.3 Numerical Considerations 205

C A Newtonian Explanation of Tether Formation? **207**

D Magnetic Field Effect On Lipids **213**

D.1 Methods 213

D.2 Results and Discussion 214

E Fabricating with S1813 **218**

E.1 Overview 218

E.2 Spinning 219

E.3 Soft-baking 220

E.4 Developing 221

E.5 Lift-off 221

Index 222

List of Tables

6.1 Two barrier fit parameters 130

7.1 Cholesterol study fit parameters 149

7.2 Tension study fit parameters 156

7.3 Biotin study fit parameters 161

7.4 SOPS study fit parameters 166

A.1 SOPC–Biotin-X recipe 194

A.2 POPC–Biotin-X recipe 194

A.3 SOPC–Biotin-X–SOPS recipe 194

A.4 SOPC–Biotin-X–Cholesterol recipe 195

B.1 MFT material constants 206

List of Figures

2.1 Various phases of phospholipid-cholesterol membranes 9

2.2 Lipid types 11

2.3 Visualization of a surface 15

2.4 Lateral pressure profile of lipid bilayer. 20

2.5 Lipid shape and curvature 21

2.6 Phase separation due to curvature 22

2.7 A microaspirated vesicle 27

2.8 A tether off a vesicle 29

2.9 A depiction of the source of interlayer drag 32

2.10 An energy potential well with a single barrier 35

2.11 Intuitive model for F_{th} versus $^{df}/_{dt}$ 40

4.1 The chrome mask used for photolithography 57

4.2 Deposition on a sapphire substrate 61

4.3 Pattern transferred to photoresist 65

4.4 Substrate with patterned photoresist 69

4.5 Electroplated gold wire within a photoresist channel 71

4.6 An electroplating supply 72

4.7 Resulting micropatterned wire 74

4.8 Photograph of the MFT after microfabrication 76

5.1 MFT cartoon and magnetic field profile 87

5.2 Master force curves for the MFT 93

5.3 Thermomechanical responses in aspirated vesicles 96

5.4 Time-course of a tether pulled from a GUV with force 100

6.1 Thermal response of MFT during different ramps 113

6.2 Tether formation 115

6.3 Current and force ramp independence 117

6.4 Establishing dynamics of tether formation 118

6.5 Checking position and current systematics 120

6.6 Examining temperature and timing systematics 122

6.7 One barrier energy models for tethering system. 124

6.8 One barrier fit and control data 126

6.9 Two barrier energy models for tethering system. 127

6.10 Two barrier model compared to control data 130

7.1 Neutral pressure drift 142

7.2 Cholesterol effect on F_{th} versus $^{df}/_{dt}$ 145

7.3 Effect of [Chol] on the relation between F_{th} and $^{df}/_{dt}$ 147

7.4 All fits for and data of cholesterol compared to control fit 148

7.5 Fit values of [Chol] studies. 151

7.6 Individual effects of τ on the relationship between F_{th} and $^{df}/_{dt}$ 153

7.7 All fits for and data of tension compared to control fit 154

7.8 Fit values of tension studies. 157

7.9 Effect of [Biotin] on the relation between F_{th} and $^{df}/_{dt}$ 160

7.10 Fit values of [Biotin] studies. 162

7.11 Effect of [SOPS] on the relation between F_{th} and $^{df}/_{dt}$ 165

7.12 Fit values of [SOPS] studies. 167

B.1 Geometric regions of the MFT 203

C.1 Log-log plot of F_{th} against $^{df}/_{dt}$ 209

C.2 t_{th} as a function of $\overline{\Delta f}$ 211

D.1 Areal strain versus frequency 215

D.2 α during with various alternating current waveforms 216

List of Equations

2.1 $C = \mathbf{n} \cdot \left(\partial^2 \mathfrak{r} / \partial s^2\right)$ 14

2.2 $\frac{C_1+C_2}{2} = \frac{\left(1+h_x^2\right)h_{yy}+\left(1+h_y^2\right)h_{xx}-2h_x h_y h_{xy}}{2\left(1+h_x^2+h_y^2\right)^{3/2}},\ C_1 C_2 = \frac{h_{xx}h_{yy}-h_{xy}^2}{\left(1+h_x^2+h_y^2\right)^2}$ 16

2.3 $\frac{C_1+C_2}{2} \cong \frac{h_{yy}+h_{xx}}{2},\ C_1 C_2 = h_{xx}h_{yy} - h_{xy}^2$ 16

2.4 $\mathcal{F} = \frac{\kappa_b}{2}\left(C_1 + C_2 + C_0\right)^2 + \kappa_G C_1 C_2$ 17

2.5 $\mathcal{E} = \tau \int dA + \frac{k_c}{2}\int \left(C_1 + C_2\right)^2 dA$ 23

2.6 $A \cong \int dxdy + \frac{1}{2}\int \left(h_x^2 + h_y^2\right) dxdy.$ 23

2.7 $A_{red}\left(\tau\right) \equiv \frac{1}{2}\left\langle \int \left(h_x^2 + h_y^2\right) dxdy \right\rangle = \frac{A}{8\pi^2}\int \frac{k_B T}{\tau q^2 + k_c q^4} q^2 dq$ 24

2.8 $\frac{A_{red}(\tau)}{A} = \frac{k_B T}{8\pi k_c} \ln\left(\frac{\pi^2/\mathfrak{b}^2+\tau/k_c}{\pi^2/A+\tau/k_c}\right)$ 24

2.9 $\frac{\Delta A}{A} = \frac{\tau}{K_A} + \frac{k_B T}{8\pi k_c}\ln\left(1 + \frac{\tau A}{\pi^2 k_c}\right)$ 24

2.10 $\frac{\Delta A}{A} = \frac{k_B T}{8\pi k_c}\ln\left(\frac{\tau A}{\pi^2 k_c}\right)$ 25

2.11 $\frac{\Delta A}{A} = \frac{\tau}{K_A}$ 25

2.12 $K_{A,app} = \left(\frac{1}{A}\frac{dA}{d\tau}\right)^{-1} = \frac{K_A}{1+K_A k_B T/8\pi k_c \tau}$ 25

2.13 $\Delta p = 2\tau\left(\frac{1}{R_p} - \frac{1}{R_V}\right)$ 26

2.14 $\tau = \frac{\Delta p}{2}\frac{R_p}{1-R_p/R_V}$ 26

2.15 $\Delta A = 2\pi R_p L_p + 2\pi R_p^2 - \pi R_p^2 = 2\pi R_p L_p + \pi R_p^2$ 28

2.16 $\frac{\Delta A}{A} = \frac{1}{4}\left(\frac{R_p}{R_V}\right)^2\left(1 + 2\frac{L_p}{R_p}\right)$ 28

2.17 $\tau = \frac{K_A}{4}\left(\frac{R_p}{R_V}\right)^2\left(1+2\frac{L_p}{R_p}\right)$ 28

2.18 $G_{bend} = 12\pi k_c + \pi k_c \frac{L_t}{R_t}$ 30

2.19 $G_{stretch} = \frac{K_A}{2} A \left(\frac{\Delta A}{A}\right)^2$ 30

2.20 $G_{pV} = -\Delta p \left(\frac{4}{3}\pi R_V^3 + R_t^2 \pi L_t\right)$ 30

2.21 $G_{load} = -f L_t$ 31

2.22 $\frac{\partial G_{tot}}{\partial R_V} = 8\pi\tau R_V - 4\pi R_V^2 \Delta p = 0$ 31

2.23 $\frac{\partial G_{tot}}{\partial R_t} = -\pi k_c \frac{L_t}{R_t^2} + 2\pi\tau L_t - 2\pi R_t L_t \Delta p = 0$ 31

2.24 $R_t = \sqrt{\frac{k_c}{2\tau}}$ 31

2.25 $\frac{\partial G_{tot}}{\partial L_t} = \pi \frac{k_c}{R_t} + 2\pi\tau R_t - \pi R_t^2 \Delta p - f = 0$ 31

2.26 $f = 2\pi\sqrt{2k_c\tau}$ 31

2.27 $f = 2\pi\sqrt{2k_c\tau} + 2\pi b h^2 \dot{L}_t \ln\left(R_V/R_t\right)$ 33

2.28 $k_{\rightarrow} = \frac{1}{t_D} e^{-E_b/k_B T}$ 34

2.29 $f_\beta = \frac{k_B T}{x_\beta}$ 36

2.30 $k_{\rightarrow}(f) = \frac{1}{t_D} e^{-\left(E_b - f x_\beta\right)/k_B T} = \frac{1}{t_D} e^{-E_b/k_B T} e^{f x_\beta / k_B T} = \frac{1}{t_{off}} e^{f/f_\beta}$ 36

2.31 $r_f \equiv \frac{t_{off}}{f_\beta}\frac{df}{dt}$ 37

2.32 $S(f) \approx \exp\left[-\int_0^f \frac{k_{\rightarrow}(f')}{df/dt} df'\right]$ 37

2.33 $p(t)\,dt = S(t)\,k_{\rightarrow}(t)\,dt$ 37

2.34 $\tilde{p}(f)\,df = p(t)\,dt$ 38

2.35 $\tilde{p}(f)\,df = p(t)\frac{dt}{df}df = \frac{k_{\rightarrow}[f(t)]}{df/dt} S[f(t)]\,df = \frac{k_{\rightarrow}(f)}{df/dt} S(f)\,df$ 38

2.36 $F_{th} = f_\beta \ln\left\{ r_f \left[\frac{\partial \ln(k_{\rightarrow})}{\partial f} - \frac{\partial \ln\left(r_f\right)}{\partial f}\right]_{f=F_{th}}\right\}$ 38

2.37 $F_{th} = f_\beta \ln(r_f) = f_\beta \ln\left(\frac{t_{off}}{f_\beta}\frac{df}{dt}\right)$ 39

2.38 $\frac{1}{df/dt} = \frac{t_{off}}{f_\beta} e^{-F_{th}/f_\beta}$ 39

2.39 $\frac{1}{k_\rightarrow} = \sum_i t_{off}\,(i)\, e^{-f/f_\beta}$ 41

2.40 $\sum_i^n \frac{t_{off,i}}{f_{\beta,i}} e^{-F_{th}/f_{\beta,i}} = \frac{1}{df/dt}$ 41

3.1 $f = 2\pi\sqrt{2k_c\tau}$ 46

4.1 $\tau_{fab} \approx \frac{1}{\alpha_{refl}} \frac{E/A}{P/A}$ 67

4.2 $V_{out,A_1} = -V_{in}\left(\frac{R_1+R_2}{R_3+R_4}\right)$ 73

4.3 $I_{R_{load}} = \frac{V_{out,A_1}}{R_s}\left(1 + \frac{R_f}{R_I}\right)$ 73

5.1 $\mathbf{B}\,(\mathbf{r}) = \frac{\mu_0 I}{2\pi A} \iint_A \frac{1}{|\mathbf{r}-\mathbf{r_0}|}\hat{\phi}\, dA$ 88

5.2 $\mathbf{B} = \frac{\mu_0 I}{2\pi y}\hat{y}$ 89

5.3 $\alpha = \frac{2R_P\Delta L(1-R_P/R_V)}{4R_V^2 - R_P^2 + 2R_P L_0}$ 90

5.4 $\mathbf{F}_{Stokes} = -6\pi\eta R\mathbf{v}$ 91

5.5 $\mathbf{F}_{ferro} = \nabla\,(\mathbf{m}\cdot\mathbf{B})$ 92

5.6 $\mathbf{F}_{para} = -\frac{\mu_0\chi_{bead}R^3}{3\pi}\frac{I^2}{y^3}\hat{y}$ 92

5.7 $\mathbf{F}_{ferro} = -\frac{\mu_0 m}{2\pi}\frac{I}{y^2}\hat{y}$ 94

5.8 $F_{return} = 2\pi\sqrt{2k_c\tau}$ 102

5.9 $F_{return} = 2\pi\sqrt{2k_c\tau} + 2\pi\frac{dL_t}{dt}h^2\ln\left(R_V/R_t\right)$ 102

6.1 $\left|\frac{df}{dt}\right| = \frac{\mu_0 m}{2\pi y^2}\frac{dI}{dt} + \frac{\mu_0 mI}{\pi y^3}v$ 116

6.2 $F_{th} = f_\beta \ln\left(\frac{t_{off}}{f_\beta}\frac{df}{dt}\right)$ 125

6.3 $\frac{df}{dt} = \left(\frac{t_{off,1}}{f_{\beta,1}}e^{-F_{th}/f_{\beta,1}} + \frac{t_{off,2}}{f_{\beta,2}}e^{-F_{th}/f_{\beta,2}}\right)^{-1}$ 128

6.4 $\mathbf{F}_{para} = \nabla\left(\mathbf{m}\cdot\mathbf{B_{tot}}\right) \propto \nabla\left(\left|\mathbf{B_{wire}}+\mathbf{B_{bkgd}}\right|^2\right) =$

$2\left|\mathbf{B}_{wire}+\mathbf{B}_{bkgd}\right|\cdot\nabla\left|\mathbf{B}_{wire}+\mathbf{B}_{bkgd}\right| \propto \mathbf{B}_{wire}\cdot\nabla\left|\mathbf{B}_{wire}\right|+\mathbf{B}_{bkgd}\cdot\nabla\left|\mathbf{B}_{bkgd}\right|+$

$\mathbf{B}_{wire}\cdot\nabla\left|\mathbf{B}_{bkgd}\right|+\mathbf{B}_{bkgd}\cdot\nabla\left|\mathbf{B}_{wire}\right| \approx \mathbf{B}_{bkgd}\cdot\nabla\left|\mathbf{B}_{wire}\right|$ 132

7.1 $\tau = \frac{\Delta p}{2}\frac{R_p}{1-R_p/R_V}$ 143

B.1 $\rho C_p\frac{\partial T}{\partial t} = \dot{q}+\nabla\cdot\left(k\nabla T\right)$ 202

C.1 $\dot{x} = \frac{f}{\beta}$ 207

C.2 $x\left(t\right) = \int_0^t \dot{x}\left(t'\right)dt' = \int_0^t \frac{\left(df/dt\right)t'}{\beta}dt' = \frac{1}{2}\frac{\left(df/dt\right)}{\beta}t^2$ 208

C.3 $t_{th,ramp} = \sqrt{\frac{2\beta L}{df/dt}}$ 208

C.4 $F_{th,ramp} = \left(df/dt\right)t_{th} = \sqrt{2\beta L}\left(df/dt\right)^{1/2}$ 208

C.5 $x\left(t\right) = \int_0^t \dot{x}\left(t'\right)dt' = \int_0^t \frac{f}{\beta}dt' = \frac{f}{\beta}t$ 208

C.6 $t_{th,pulse} = \frac{\beta L}{f}$ 208

C.7 $\overline{\Delta f} \equiv \frac{F_{th,pulse}-F_{th,ramp}}{F_{th,ramp}}$ 210

C.8 $F_{th,ramp}t_{t,pulse} = \frac{\left(df/dt\right)t_{th,ramp}^2}{2}$ 210

D.1 $\alpha = \frac{2R_P\Delta L(1-R_P/R_V)}{4R_V^2-R_P^2+2R_PL_0}$ 214

D.2 $\frac{1}{T_{AC}}\int_0^{T_{AC}} IV\,\sin^2\left(\frac{2\pi t}{T_r}\right)dt \approx \frac{IV}{2}$ 217

Nomenclature

Roman Symbols

A	Cross-sectional Area
$A_{red}(\tau)$	Area Deviation due to Membrane Fluctuations
b	Interlayer Drag Coefficient
b	Intermolecular Spacing
$\mathbf{B}$	Magnetic Field
C_0	Spontaneous Curvatures of a Surface
$C_{1,2}$	Principle Curvatures of a Surface
C_p	Heat Capacity
$\mathrm{E}(x)$	Potential Energy Landscape of Tether Formation
f	Applied Force
f_β	Force Required to Lower an Energy Barrier by k_BT
$\overline{\Delta f}$	Ratio of $F_{th,pulse} - F_{th,ramp}$ to $F_{th,ramp}$
$\mathcal{F}$	Helfrich Energy Density
$\mathbf{F}_{mag}$	Applied Magnetic Force

$\mathbf{F}_{Stokes}$	Stokes Force
$^{df}/_{dt}$	Force Rate
F_{th}	Force Threshold
G_{bend}	Energy of Bending
G_{load}	Energy of Applied Force
G_{pV}	Energy of P-V Work
$G_{stretch}$	Energy of Stretching
G	Free Energy
h	Membrane Thickness
$h\left(x,y\right)$	3rd Coordinate of $\mathfrak{r}$ (in Background)
$H\left(t_{stop}-t\right)$	Heaviside Function that goes to zero at t_{stop}
I	Applied Current
k	Thermal Conductivity
K_A	Compressibility Modulus
$K_{A,app}$	Apparent Compressibility Modulus due to Tension
k_c	Local Bending Modulus

L_0	Initial Vesicle Projection Length
ΔL	Change in Projection Length of Vesicle
L	Distance a Membrane Extends Before Tether Formation
L_t	Length of the Tether
L_p	Projection Length of Vesicle into Pipette
$\mathbf{m}$	Magnetic Moment of the Bead
$\mathbf{n}$	Unit Normal Vector
Δp	Pressure Difference between Pipette and Bulk Solution
Δp_0	Change in the Neutral Pressure of a Microaspirator
q	Wavevector of Undulating Membrane
$\dot{q}$	Power Density
$\mathbf{r_0}$	Position of Cross-sectional Area
R	Radius of Magnetic Bead
r_f	Loading Rate of Tether System
R_P	Pipette Radius
$\mathfrak{r}$	A point on a sample surface

$\mathbf{r}$	Position of bead
R_t	Tether Radius
R_V	Vesicle Radius
S	Probability of Being in Bound State in Tether Energetic Model
T	Temperature
t	Time
T_{AC}	Time greater than T_r during an AC pulse
T_r	Response Time
t_{stop}	Time that Current Stops Flowing
t_{th}	Time Taken to Form a Tether
t_{off}	Reciprocal of Tether Formation Attempt Rate when $f = 0$.
$\mathbf{v}$	Velocity
V	Applied Voltage
x	Distance from Wire Edge (for Tethers)
x	1st Coordinate of $\mathfrak{r}$ (in Background)
y	Distance from the Center of the Wire

y	2nd Coordinate of $\mathfrak{r}$ (in Background)

Greek Symbols

α_{refl}	Reflectivity Coefficient
α_T	Area Expansivity Modulus
α	Vesicle Strain
β	Drag Constant
χ_{bead}	Magnetic Susceptibility
η	Viscosity
κ_G	Gaussian Bending Rigidity
μ_0	Permeability of Free Space
ρ	Density
τ_{fab}	Exposure Time
τ	Membrane Tension

Abbreviations

AFM	Atomic Force Microscopy
Biotin-X DHPE	*N*-((6-(biotinoyl)amino)hexanoyl)-1,2-dihexadecanoyl-*sn*-glycero-3-phosphoethanolamine, triethylammonium salt

BSA	Bovine Serum Albumin
GUV	Giant Unilamellar Vesicle
MFT	Magnetic Force Transducer
PBS	Phosphate Buffered Saline
PDMS	Polydimethylsiloxane
POPC	16:0-18:1 PC or 1-palmitoyl-2-oleoyl-*sn*-glycero-3-phosphocholine
SOPC	18:0-18:1 PC or 1-stearoyl-2-oleoyl-*sn*-glycero-3-phosphocholine
SOPS	18:0-18:1 PS or 1-stearoyl-2-oleoyl-*sn*-glycero-3-phospho-L-serine

Mathematical Symbols

$\langle \cdot \rangle$	Boltzmann-weighted Average

Chapter 1

An Introduction

There is nothing more difficult to take in hand, more perilous to conduct, or more uncertain in its success, than to take the lead in the introduction of a new order of things. - Niccolo Machiavelli [2]

RUBBER, soap bubbles, toothpaste, and cell membranes are all soft materials. They are all self-organizing; from small individual components, such as a monomer or a single surfactant, they link and form large complexes whose properties depend upon how the components were linked. They are also all materials with significant physical behavior that occurs at energies comparable to room temperature thermal energy [3]. In the case of cell membranes, the individual component is an amphiphilic molecule and the significant physical behavior is bending. Cells take advantage of bending to perform many functions, such as cell fusion and transport through tissue. Further functions are performed through use of tethers, or a thin, long tube of membrane with very high curvature, including activation of white bloods cells vital for immune response [4, 5], trafficking material between cells [6, 7], or initiating lysis in target cells by natural killer cells over long distances [8].

While the dynamic formation of tethers are prevalent in cellular systems [4, 9], there is a lack of experimental tools to form them in a controlled environment with well-defined, dynamic, and controllable forces, which would be of great value to study

their properties and to study membrane physics in general. For studying tethers, knowing applied forces *a priori* improves knowledge of not only the magnitude but also of the rate at which forces are applied. Tools such as atomic force microscopy and optical tweezers, however, require careful and thorough calibration methods to obtain this knowledge. Further, these techniques often require support from a substrate in order to perform experiments and interpret results. To move subject matter like vesicles—a model system of a cell membrane composed of a lipid bilayer—off of the surface, a device that applies forces to produce tethers should be integrated with microaspiration, which is a method that utilizes pipettes with microscale tips in order to hold cells or vesicles with uniform tension. Magnetic tweezers, which generate a magnetic field to control the force on a magnetic bead that is attached to a membrane, have also been used to apply controlled forces to membranes. Depending on design, they can exert either small forces of a few piconewtons [10] or large forces up to several nanonewtons [11]. Furthermore, magnetic tweezers are straightforward to construct and are inexpensive. As they are typically made of bulk materials, however, magnetic tweezers can by limited in how quickly forces may be changed [11]. Microfabricated magnetic tweezers generate current with microfabricated wires that are close to the sample. They can be used to manipulate forces on much faster time scales, but thus far also do not support integration with other membrane manipulation techniques, such as microaspiration. Microaspiration, on its own, is used for studying tethers but either must use a slowly varying force, such as gravity [12], to pull a tether or must

couple the applied tension to the force applied to pull a tether as the pipette is used for both capacities simultaneously [13].

In this thesis, we describe the construction of a microfabricated magnetic force transducer (MFT) and its application to forming tethers and studying membrane biophysics. Our design enables the incorporation of a microaspirator into the assembly in order to control membrane tension. It also fulfills other important criteria, such as ease of theoretical description, manufacture, affordability, range in forces and force ramps, and integrability into other microscopic setups.

This MFT generates highly localized magnetic fields to apply point forces to an aspirated vesicle via a magnetic bead. Using the point forces, we found a novel dependence of the force required to pull a tether on the rate of change in the force. While another system has very recently found a qualitatively similar dependence in studies on cells [13], our work is the first to examine a pure lipid system with distinct control of tension and applied point forces. To explain the phenomena observed, we developed an energetic model analogous to that model proposed to explain membrane rupture with increasing tension [14]. With this model, we examined the effect that various modifications would have on the membrane. In particular, we included cholesterol in the membrane to investigate how variation in packing parameter and diffusion in the membrane would affect the energetics of tether formation. Studies were additionally conducted on the effects of tension. We also adjusted the biotin concentration to determine what influence the number of receptor-ligand bonds had

on tether formation, and of charged lipids (phosphatidylserine) to look at the impact of lipid structure. In addition to probing the dynamics of tether formation, we further used the device to examine the frictional drag between the inner and outer leaflets of the bilayer membrane. Finally, a full numerical model of the thermal properties of the system was developed and utilized to accurately ascertain the effect of temperature upon the system, thus demonstrating additional applications of this new tool. The microfabricated MFT enabled new biophysical studies of the dynamics of tethers.

In order to provide a starting point for this thesis, Chapter 2 reviews continuum membrane mechanics to provide a base for understanding tether formation. Chapter 3 covers the field of various magnetic force applicators—bulk, microfabricated, permanent, and electromagnetic, including their benefits and drawbacks in order to set-up Chapter 4, which details how the microfabricated device were built. Chapter 5 presents the magnetic force transducer-aspiration system and some introductory biophysical studies to demonstrate its usefulness. Extending from Chapter 5, Chapter 6 investigates the relationship between force threshold and the time rate of change in force application. A two-barrier energetic model is further proposed to explain the observed dependence. Chapter 7 examines this correlation under a variety of experimental conditions. A series of appendices cover vesicle making protocols (Appendix A), the numerical methods used to model thermal properties of the MFT (Appendix B), an alternate classical model for tether formation (Appendix C), the influence the magnetic field has on membrane properties (Appendix D), and micro-

fabrication methods with alternate resists (Appendix E).

Chapter 2

A Membrane Mechanics Primer

Each individual fact, taken by itself, can indeed arouse our curiosity or our astonishment, or be useful to us in its practical applications. - Hermann von Helmholtz [15]

BACKGROUND and context are vital to understand any topic. Especially in the sciences, being familiar with the fundamentals of a topic provide the cornerstone for further growth in knowledge. In order to supply this foundation, we review, in this chapter, the components which make up membranes and several aspects of the underlying mechanics of membranes. A brief review of Kramer energetics follows to describe the theoretical foundation for the work that will be presented in Chapter 6.

2.1 Membrane Composition

To understand *how* something works, it is often wise to first be familiar of *what* that something is composed. While a membrane is composed of thousands or more distinct types of components, the majority of them fall into three families: saccharides, proteins, and lipids.

2.1.1 Non-lipid Membrane Components

Saccharides, or carbohydrates, are polymers composed of monosaccharides, and whose function within the membrane, when conjugated to lipids in the form of glycolipids, includes protecting the cell from adverse environments, modifying local electric fields, cell recognition, and cell surface receptors [16, p. 593]. Carbohydrates are an important class of molecule for proper cellular function but will not be further developed in this work.

Proteins are another biopolymer formed from the joining of amino acids, whose charge, polar nature, and shape contribute largely to the protein's eventual function. Within the membrane, proteins serve to start signaling cascades to regulate cellular function, transport ions such as protons and calcium, release energy from adenosine triphosphates (ATP), synthesize ATPs, transduce mechanical stimuli, and a plethora of other functions. Membrane proteins depend upon the mechanics of the membrane for function and directly influence these processes [17, 18] and rightly form a significant portion of membrane research.

2.1.2 Lipids

Lipids form the bulk of membranes, and are amphiphilic molecules; they consist of a hydrophobic domain connected to a hydrophilic domain. The amphiphilic lipids have toward water leads them to spontaneously form self-assembled nanostructures (to be covered in Section 2.2.2), including the bilayer membranes that form cell membranes

or vesicles. Lipids may be further divided into fat acyls, sphingolipids, glycerolipids, sterol lipids, and phospholipids. Fat acyls are the carbon chains by which more complicated lipids are formed. Sphingolipids consist of fat acyls joined with the amino acid serine and sugar residues. They provide mechanical stability to the membrane due to their ability to pack tightly and are important in cell signaling and recognition [19]. Sterols are composed of a base four carbon ring structure and serve primarily as hormones and signaling molecules. One type of sterol, cholesterol, is a vital component of mammalian membranes. Cholesterol can not only increase the fluidity of a membrane, but also provides the increased packing necessary for inducing phase separation in membranes [19]. As reviewed by van Meer *et al.* [19], cholesterol helps create enriched domains, or temporary regions of high cholesterol content that facilitate protein function. Cholesterol leads to the formation of either solid gel (Figure 2.1b), liquid ordered (Figure 2.1c), or liquid disordered phases (Figure 2.1a) in the membrane. The long saturated tails of sphingolipids lead to a solid gel phase that helps form lipid rafts in cells and is typified by diffusion coefficients on the order of $10^{-3}\,\mu\mathrm{m}^2/\mathrm{s}$ and high packing parameters. Liquid ordered phases with diffusion coefficients on the order of $1\,\mu\mathrm{m}^2/\mathrm{s}$ and greater packing may appear when cholesterol is a constituent of the membrane. Whether the liquid ordered phase, the liquid disordered state (diffusion coefficients on the order of $1\,\mu\mathrm{m}^2/\mathrm{s}$ and no long range order), or a coexistence between the two form depends upon the saturation of the surrounding lipids and system temperature [19]. The presence of these phases were first verified

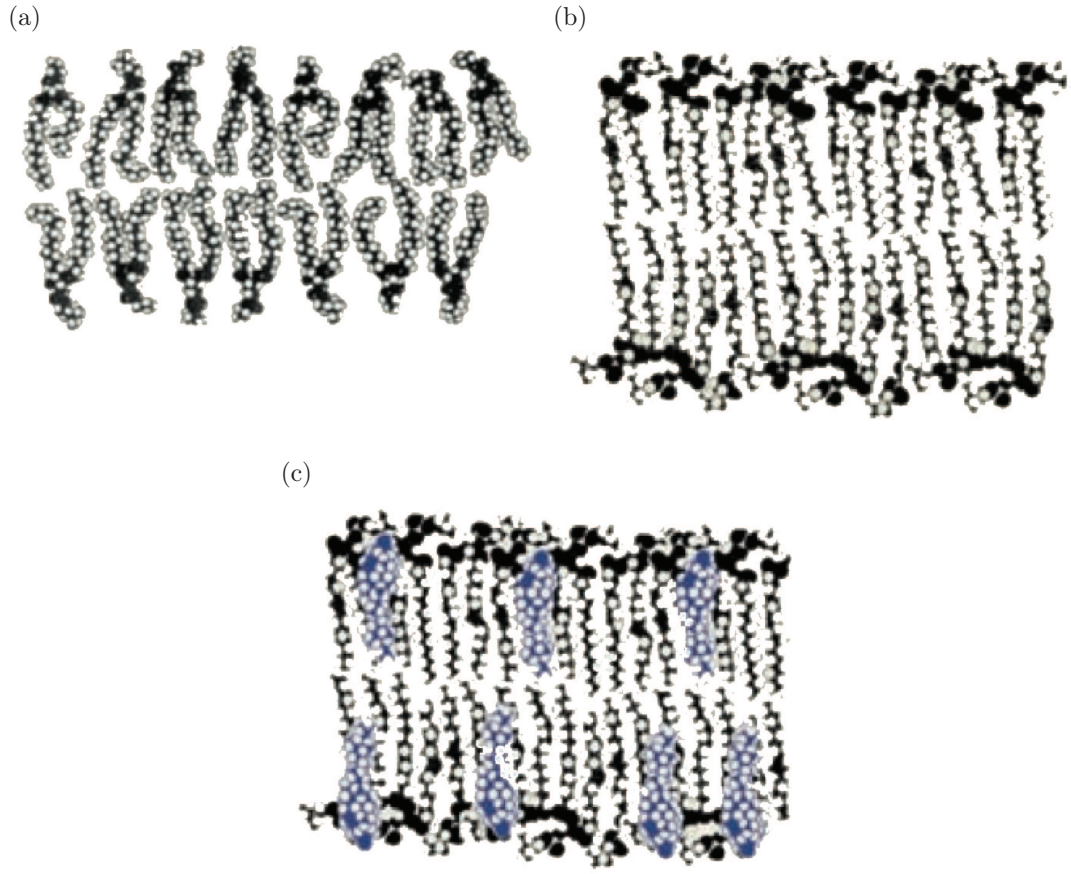

Figure 2.1 : Various phases of phospholipid-cholesterol membranes (adapted from [19]). (a) The liquid disordered phase exhibits low packing parameters and very high diffusion coefficients. (b) The solid gel phase occurs with lipids with long, saturated tails, such as sphingomyelin. This phase exhibits long range order but low diffusion coefficients. (c) In the presence of cholesterol, lipid bilayers may exhibit the liquid ordered phase, which is characterized by higher packing parameters and high diffusion coefficients.

in vesicles using fluorescence microscopy by Veatch and Keller [20, 21] and has been generally been accepted to be present in cell membranes [22].

Glycerolipids are fatty acid esters of glycerol (three carbons and associated hydroxyl groups) and largely provide storage fat in animals. A particular family of glycerolipids though form the foundation of the membrane itself: phospholipids. Phospholipids consist of two fatty acid chains attached to two carbons of a glycerol with a phosphate and headgroup off the third carbon. The chain lengths and unsaturation content lead to variations in packing density [23] and curvature of the membrane [24, pp. 378–82]. The headgroups also contribute to membrane mechanics. Phosphatidylcholine (PC) forms about 20% of eukaryotic cellular membranes and is found at particularly high concentrations in the outer leaflet [16, p. 589]. Phosphatidylethanolamine (PE) with its primary amino group is often partitioned to the inner membrane and forms 10-20% of the membrane. Also often found in the inner membrane, phosphatidylserine (PS) occurs in concentrations of less than 10% and is important in establishing a charge difference between leaflets as it is the only headgroup with a net charge at physiological conditions [16, pp. 589–90].

The structures of the lipids used for this work are diagrammed in Figure 2.2. SOPC (1-stearoyl-2-oleoyl-*sn*-glycero-3-phosphatidylcholine) has two 18 carbon tails, one of which is monounsaturated, and a PC headgroup. POPC (1-palmitoyl-2-oleoyl-*sn*-glycero-3-phosphocholine) is similar to SOPC but with a 16 carbon saturated tail. With a modified head group, SOPS (1-stearoyl-2-oleoyl-*sn*-glycero-3-phospho-

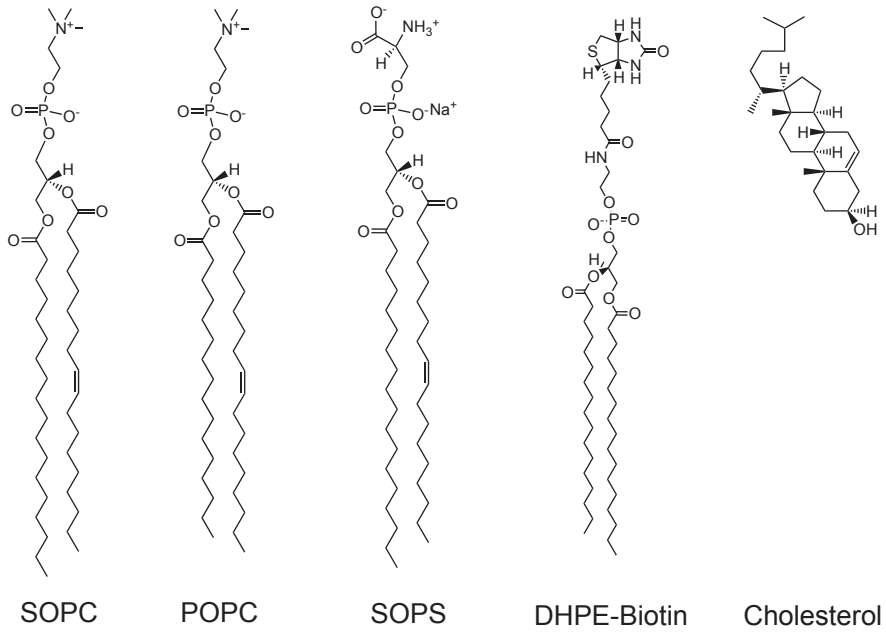

Figure 2.2 : Various lipids found within a cell that are relevant to the experiments in this thesis. SOPC, POPC, and SOPS are phospholipids. DHPE-Biotin is a phospholipid conjugated with a biotin molecule and cholesterol is a sterol (structures provided by or modified from Avanti Polar Lipids).

L-serine) has the same tail structure as SOPC but a PS headgroup. To provide sites for receptor-ligand binding, DHPE-Biotin ((*N*-((6-(biotinoyl)amino)hexanoyl)-1,2-dihexadecanoyl*sn*-glycero-3-phosphoethanolamine) composed a part of every vesicle. While affecting the membrane through shorter tail lengths and full saturation of chains, DHPE-Biotin is kept in low concentrations ($< 10\,\text{mol}\%$) to not significantly effect membrane mechanical properties. Cholesterol is a much smaller, very hydrophobic molecule due to its four carbon rings. As described above, cholesterol may modify the phase behavior of vesicles. These few lipids form the basis of the multitude of studies that will be discussed in Chapters 5 and 6.

2.2 Mechanical Properties of Membrane

To fully understand the studies conducted in this thesis using point forces applied to vesicles, one must first be familiar with the concepts and principles behind the studies. In this section, the major concepts of continuum mechanics of a membrane will be reviewed. The membrane is essentially a soft, thin material that is easily bent but difficult to compress, analogous to rubber [3, 25]. However, while the properties of rubber depend upon the crosslinking between component monomers, the properties of lipid membranes come from the balance of entropic expulsion of water from the hydrophobic region of the membrane with the steric repulsion of lipid acyl chains. As such, one may initially assume that the mechanics underlying membranes are governed by the microscale. At the microscale, stochasticity due to thermal fluctuations domi-

nate the system, lengths are on the order of 1 nm and timescales are on the order of a few microseconds. Lipid membranes, however, have characteristic lengths of several hundred nanometers and characteristic times of milliseconds. Hence, while a single lipid can be examined microscopically, a mean-field approach is needed for the entire membrane [26]. These scale are yet too small for macroscopic consideration, particularly as membranes undulate readily at room temperature at scales that macroscopic descriptions fail to capture [27]. To extenuate the uniqueness of membranes yet more, they are two-dimensional structures that act as fluids with patches on the order of tens to hundreds of nanometers [28]. Lipid membranes live in the mesoscopic regime, where both thermal fluctuations and bulk mechanics compete. For example, a freely floating vesicle will undulate due to thermal energy; however, with a sufficiently high tension, the undulations become negligible and the lipid expands as a linear material (see Section 2.2.3 for further development). The lipid membrane is at a mechanically intriguing regime where the microscopic and macroscopic meet.

When a force acts upon a membrane, the membrane may respond through area changes, bending, or shearing. For pure lipid membranes, there is negligible resistance to shear ($\sim 10^{-6}\,{}^{\mathrm{N}}/_{\mathrm{m}}$ in the case of the more complicated red blood cell [29]) and so will not be considered here. Area changes result from the applied force stressing the membrane which results in a change in strain through the stress-strain relationship [30, pp. 65–7]. The applied force manifests as tension in the membrane and, in microaspiration experiments (explained in Section 2.2.4), is typically on the or-

der of $10^{-5} - 10^{-3}$ N/m in vesicles (with thermal fluctuations being damped out by $\sim 5x10^{-4}$ N/m [31]) and 10^{-4} N/m in red blood cells [32]. Strain of the membrane is typically no more than 6% [31, 33], and the link between how much an area will expand with an applied stress is characterized by a compressibility modulus given as K_A. Bending results from a curvature change in the membrane due to the applied force, with the curvature changing from 10^5/m to 10^7/m in tether experiments (explained in Section 2.2.5) possible. The bending of the membrane relates to the bending modulus k_c and is typified by curvature: normal, Gaussian, and spontaneous. These moduli and associated ideas will be then be applied to an aspirated vesicle and finally to a tether coming off a vesicle to provide a base for the experiments presented in Chapters 5 and 6.

2.2.1 Normal and Gaussian Curvatures

Normal and Gaussian curvatures may be derived by examining a two dimensional Riemannian surface, such as in Figure 2.3 and determining its principal curvatures*. The tangent and unit normal vector may be used to determine the principal, mean, and Gaussian curvatures. In general, the curvature of a surface can be defined by:

$$C = \mathbf{n} \cdot \left(\partial^2 \mathfrak{r} / \partial s^2\right), \tag{2.1}$$

*This section is largely based upon [30] and to a lesser extent [34].

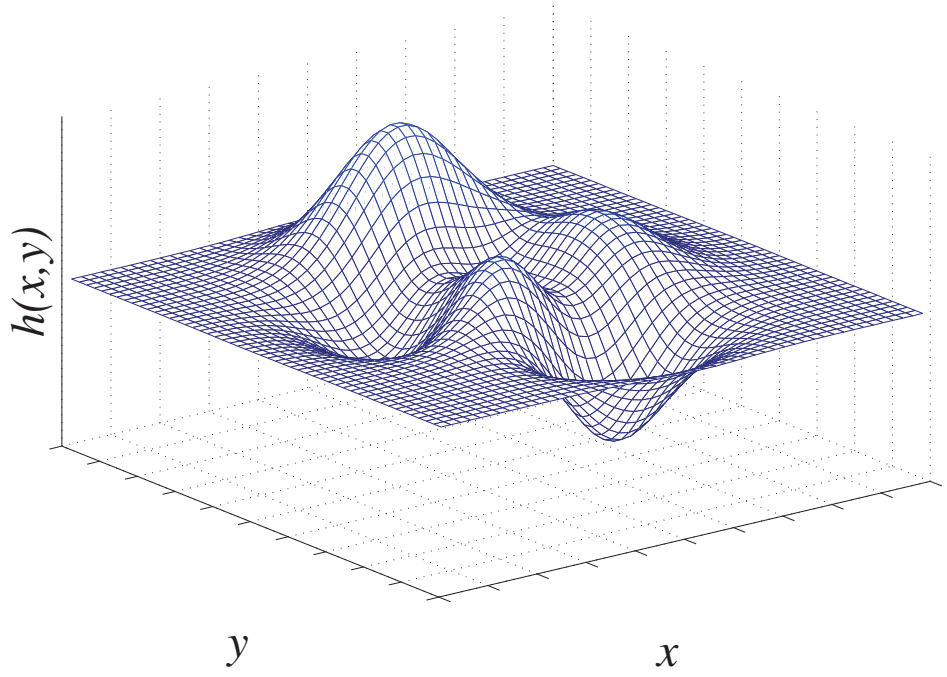

Figure 2.3 : A surface can be defined by a function $h\,(x, y)$ dependent on a set of external Cartesian coordinates x, y. Modeled after [34, p. 419] using the built-in MatLab peaks function.

where the unit normal vector, $\mathbf{n}$, $\mathfrak{r}$ is a point on the surface, and s is the arc length along a curve. As a curve may vary along a surface, the curvature of a surface is not unique. For example, the curvature ranges from 0 to $1/R$ for a cylindrical shell. The maximum and minimum values of curvature as a function of direction for a surface are called principal curvatures and denoted by C_1 and C_2. With C_1 and C_2, one can find the mean curvature, which is the average curvature, and the Gaussian curvature, which is an intrinsic measure with a sphere having a positive value. The mean curvature is $(C_1+C_2)/2$, while the Gaussian curvature is C_1C_2.

Using the detailed derivation conducted by Boal [30, pp. 179-81], the mean and Gaussian curvatures are

$$\begin{aligned} \frac{C_1+C_2}{2} &= \frac{\left(1+h_x^2\right)h_{yy}+\left(1+h_y^2\right)h_{xx}-2h_xh_yh_{xy}}{2\left(1+h_x^2+h_y^2\right)^{3/2}}, \\ C_1C_2 &= \frac{h_{xx}h_{yy}-h_{xy}^2}{\left(1+h_x^2+h_y^2\right)^2}, \end{aligned} \tag{2.2}$$

which, for slowly varying functions corresponding to gentle undulations,

$$\begin{aligned} \frac{C_1+C_2}{2} &\cong \frac{h_{yy}+h_{xx}}{2} \\ C_1C_2 &= h_{xx}h_{yy}-h_{xy}^2. \end{aligned} \tag{2.3}$$

approximates Equation 2.2. $h_\alpha = \partial h/\partial\alpha$ $(\alpha = x, y)$ in the above equation where $h(x, y)$ is the height of the surface at the associated two-dimensional coordinate projection (x, y).

The energy density of bending deformations $\mathcal{F}$ associated with these curvatures, or Helfrich energy density, can be written as [30, p. 182]

$$\mathcal{F} = \frac{k_c}{2}\left(C_1 + C_2 + C_0\right)^2 + \kappa_G C_1 C_2 \tag{2.4}$$

where k_c and κ_G are the bending rigidity—or bending modulus—and Gaussian bending rigidity—or saddle-splay modulus, and C_0 is the spontaneous curvature, which will be explained below. k_c is readily measured using aspiration techniques (for examples, see [31, 33]) and found to be on the order of $\sim 1x10^{-19}$ J (or $25\,k_BT$). The bending modulus may be: increased through the long range ordering of cholesterol (by a factor of ~ 3 to $\sim 3x10^{-19}$ J for SOPC at 50 mol% cholesterol [35, 36]), increased curvature (factor of $\sim$ 2 to $1.5x10^{-19}$ J for 2:1 a 1,2-dioleoyl-*sn*-glycero-3-phosphocholine:cholesterol mixture with a ~ 5 fold increase in curvature [37]), and increased chain length (factor of ~ 2 to $1.2x10^{-19}$ J as chain length increased from 13 carbons to 22 [38]); and decreased through the disruption caused by salicylate (by a factor of ~ 2 to $0.5x10^{-19}$ J for SOPC at 10 mM [31]) and the disorder caused more than two unsaturations in a lipid tail (factor of $\gtrsim 2$ decease to $0.4x10^{-19}$ J drop for increase in unsaturations from 1 to 6 [38]).

While k_c may be readily measured, κ_G is difficult to measure in membranes as it invariant to translation and rotation [34]. Yet, since the integral over the surface of the Gaussian curvature does not change with the shape of the surface as long as the topology of the surface is fixed (the Gauss-Bonnet Theorem [30, p. 183]), one may still

describe shape changes of membrane systems with fixed topology without knowing κ_G [34, p. 425]. Interestingly, it can additionally be shown from Equation 2.4 that the energy for a sphere, regardless of radius, is $8\pi k_c$. These developments will be used below to derive the equations governing tether formation.

2.2.2 Spontaneous Curvature

As seen in Equation 2.4, spontaneous curvature quadratically influences the energy density of the membrane. The minimization of the energy leads to the topology of the membrane; spontaneous curvature contributes to the shape. The intrinsic curvature of a lipid arises from a difference in effective area between that of a lipid's polar headgroup and of its acyl chains, caused by steric, hydrophobic, and electrostatic factors [24, pp. 378-82]. Steric factors include the size of the headgroup, the length of the acyl chains, the number of chains, and the extent each chain is unsaturated. Entropic interactions, namely ensuring water molecules are in the bulk, lead to the hydrophobic attraction of acyl chains from lipid to another, minimizing the separation between chains. Electrostatic factors primarily concern the charge on the headgroup. As like charges repel, headgroups of similarly charged lipids will increase separation among lipids. All these factors lead to a lateral pressure profile of the membrane (see Figure 2.4) consisting of an attractive interfacial region and repulsive headgroup and chain regions [39]. The balance of this profile leads to the membrane shape, and can be approximated by the spontaneous curvature.

The spontaneous curvature can be positive, negligible, or negative. Lipids with positive curvatures consist of lipid headgroups whose area are greater than that of acyl chains, as in Figure 2.5a. These lipids may lead to the formation of micelles which consist of self-assembled structures with polar groups exposed to an aqueous solution and apolar tails protected within. Lipids with similar areas lead to bilayer formations, see Figure 2.5b. Bilayer formations consist of two leaflets of opposing direction in aqueous solutions; the polar headgroups face the solution, while the tails are again shielded from water. Lipids of negative curvature, however, tend to invert in apolar solutions, forming inverse micelles, or H_{II}-phase structures. These lipids are mixed within a cell [34, p. 413], helping to form the variety of morphologies observed among cell types.

One of the morphologies that may be synthetically replicated is that of a giant unilamellar vesicle (GUV), which is a spheroid bilayer membrane with a radius of $10 - 20\,\mu$m that acts as a model system of a cell membrane. GUVs have been used extensively to look at phase separation due to cholesterol [20, 21] and due to curvature (see Figure 2.6, [40]). Finally, using GUVs, curvature has also been established to affect inter-leaflet motion and the dynamics of tether formation [41]. This phenomena forms the basis of future tether studies.

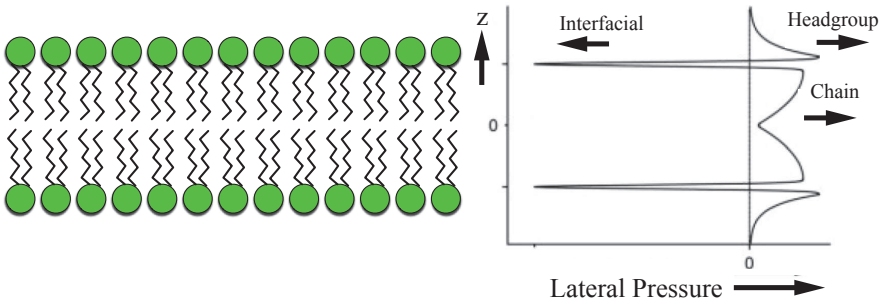

Figure 2.4 : Lateral pressure profile of lipid bilayer. The lateral pressure across the bilayer, given against a cross-section of the bilayer, consists of the balanced pressures of the lipid headgroups, chains, and interfacial regions. Adapted from [39].

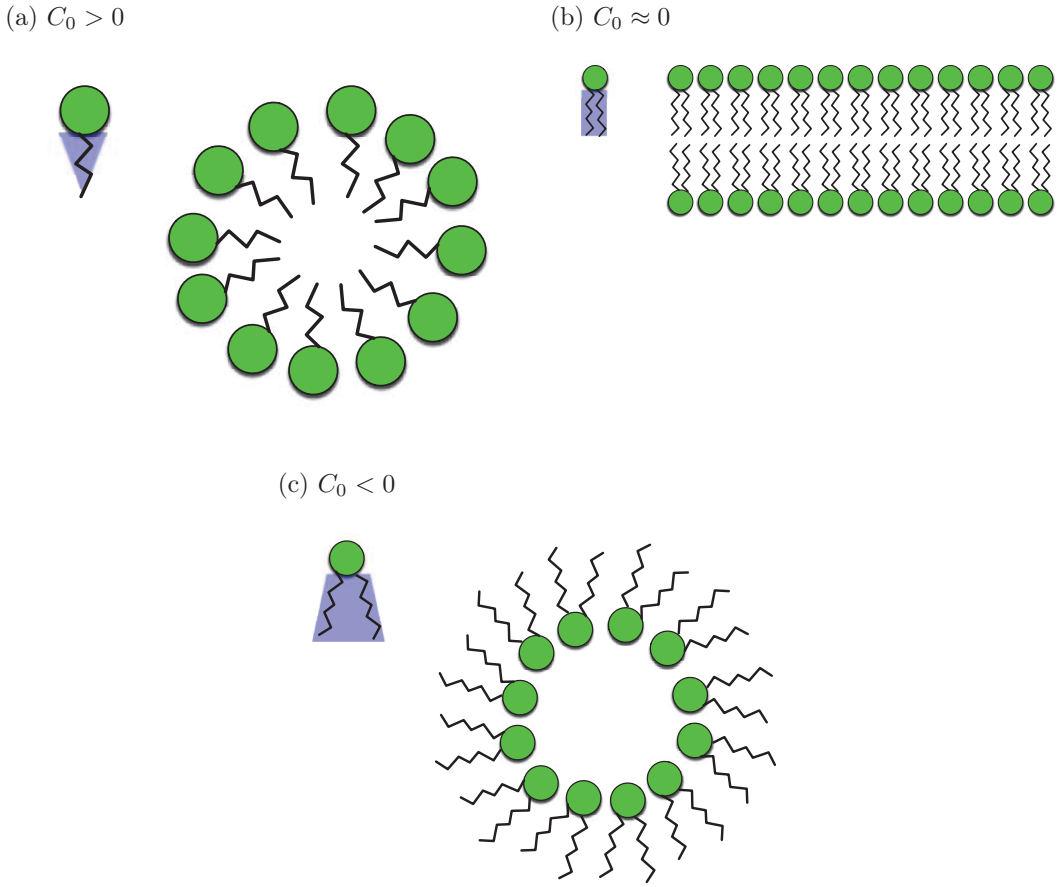

Figure 2.5 : Steric effects of lipids on spontaneous curvature. (a) Lipids with head groups of larger cross-sectional areas than that of the acyl chains (packing parameter $< 1/3$) have positive curvature, forming micelles. (b) With roughly equal cross-sectional areas of head groups and acyl chains (packing parameter $\sim 1/3 - 1$), lipids of neutral curvature generate bilayers. (c) Inverse micelles or H_{II}-phase lipids consist of acyl chains with larger cross-sectional areas than their head groups (packing parameter < 1). The structure is induced by negative curvature. Packing parameters and inspiration for figures from [24, p. 381].

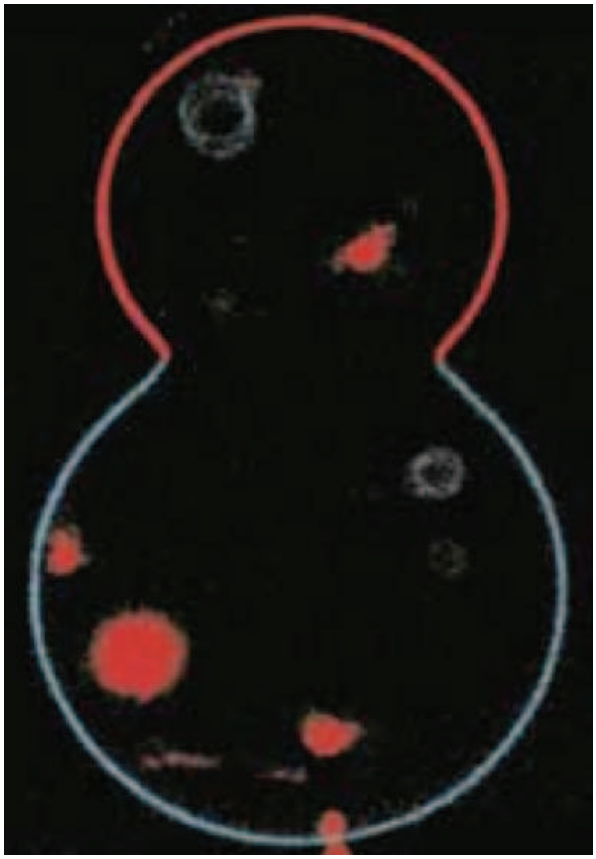

Figure 2.6 : Phase separation due to curvature. The two coexistent phases are sphingomyelin- and cholesterol-enriched DOPC (blue) and pure DOPC (red). Adapted from [40].

2.2.3 Compressibility

The formalism developed above for curvature can be extended to determine the stretch a membrane experiences as a tension τ is applied[†]. Using the Helfrich energy, Equation 2.4, with the Gaussian curvature taken as negligible and including the energy associated with the added tensile stress, the energy of a membrane G is given by

$$G = \tau \int dA + \frac{k_c}{2} \int (C_1 + C_2)^2 \, dA, \tag{2.5}$$

with $dA = \sqrt{1 + h_x^2 + h_y^2} dxdy$ [30, p. 197]. As the membrane is only $\sim 4\,\mathrm{nm}$ thick and the energy associated with the bending modulus ($\sim 1x10^{-19}\,\mathrm{J} \approx 25\,\mathrm{k_BT}$) is much less than that of compressibility (compressibility is typically on the order of $10^2\,{}^{\mathrm{mN}}/_{\mathrm{m}} \approx 50 - 70\,{}^{k_BT}/_{\mathrm{nm}^2}$ [34, p. 423], corresponding to $\sim 1x10^{-16}\,\mathrm{J} \approx 25x10^3\,\mathrm{k_BT}$ for the entire membrane), there may be significant undulations in the membrane [31]. The area may then be separated into a non-undulating term and a fluctuating term if one assumes gentle undulations of the membrane:

$$A \cong \int dxdy + \frac{1}{2} \int \left(h_x^2 + h_y^2\right) dxdy. \tag{2.6}$$

Averaging the second term over all configurations with Boltzmann weights leads to a

[†]This section follows [30, Sec. 6.5]

deviation of area, $A_{red}(\tau)$, due to curvature of

$$A_{red}(\tau) \equiv \frac{1}{2}\left\langle \int \left(h_x^2 + h_y^2\right) dxdy \right\rangle = \frac{A}{8\pi^2}\int \frac{k_B T}{\tau q^2 + k_c q^4} q^2 dq, \tag{2.7}$$

where q is the corresponding two-dimensional wave-vector, and k_B and T are the Boltzmann constant and temperature, respectively. Physically, q corresponds to a fluctuation mode of the membrane, which can vary from from $\pi/A^{1/2}$, the size of the membrane, to π/b, with intermolecular spacing b . Equation 2.7 can then be integrated to obtain [30, p. 198]

$$\frac{A_{red}(\tau)}{A} = \frac{k_B T}{8\pi k_c} \ln\left(\frac{\pi^2/\mathrm{b}^2 + \tau/k_c}{\pi^2/A + \tau/k_c}\right). \tag{2.8}$$

Recognizing $A \gg \mathrm{b}^2$, defining $\Delta A \equiv A_{red}(0) - A_{red}(\tau)$, and taking into account the first term of Equation 2.5, the area strain $\Delta A/A$ is found to be

$$\frac{\Delta A}{A} = \frac{\tau}{K_A} + \frac{k_B T}{8\pi k_c} \ln\left(1 + \frac{\tau A}{\pi^2 k_c}\right), \tag{2.9}$$

where K_A is the compressibility modulus (on the order of $10^2\ \mathrm{mN/m}$ [31]). The first term of Equation 2.9 is due directly to the application of tension to the membrane; the second term results from thermal fluctuations of the membrane.

In the limit of low tension, Equation 2.9 reduces to

$$\frac{\Delta A}{A} = \frac{k_B T}{8\pi k_c} \ln\left(\frac{\tau A}{\pi^2 k_c}\right). \tag{2.10}$$

At high tension, the significance of undulations from thermal fluctuations is reduced and the membrane becomes analogous to a flat two-dimensional elastic material. The areal expansion of the membrane then depends on the compression and tension by

$$\frac{\Delta A}{A} = \frac{\tau}{K_A}. \tag{2.11}$$

The compressibility thus appears to depend upon tension, and this apparent compressibility $K_{A,app}$ is given by [30, p. 199]

$$K_{A,app} = \left(\frac{1}{A}\frac{dA}{d\tau}\right)^{-1} = \frac{K_A}{1 + {}^{K_A k_B T}/_{8\pi k_c \tau}}. \tag{2.12}$$

The compressibility may also be modulated by the incorporation of addition molecules into the membrane. With the presence of cholesterol, the compressibility increased (by a factor of ~ 3.5 to $640\,{}^{\mathrm{mN}}/_{\mathrm{m}}$ for SOPC at 50 mol% cholesterol [36]). The compressibility decreased when salicylate was present (by a factor of ~ 2 to $100\,{}^{\mathrm{mN}}/_{\mathrm{m}}$ for SOPC at 10 mM [31]). Chain length, however, did not significantly effect compressibility [38].

In summary, a membrane behaves elastically, unless the tension is low enough that thermal fluctuations of the membrane effect compressibility. With the background

of bending and stretch established in these past few sections, the physics governing aspirated vesicles and tethers may be developed.

2.2.4 Mechanics Applied to Microaspiration

Microaspiration is a standard method to measure membrane mechanical properties[‡]. Take an aspirated vesicle, much like the one diagrammed in Figure 2.7, and consider the pressure difference experienced by the vesicle outside the pipette and by the vesicle as a projection within the pipette. The pressure difference between the outside environment and the inside of the vesicle, of radius R_V, can be found using the Laplace-Young Law to be $2\tau/R_V$, while the pressure difference between the vesicle and the environment inside the pipette, of radius R_p, is similarly found as $2\tau/R_p$. The pressure difference between the pipette and the environment, Δp, can then be related:

$$\Delta p = 2\tau \left(\frac{1}{R_p} - \frac{1}{R_V} \right). \tag{2.13}$$

Solving for the tension τ yields

$$\tau = \frac{\Delta p}{2} \frac{R_p}{1 - R_p/R_V}, \tag{2.14}$$

which shows the direct dependence of the tension in the membrane on the applied pressure, and its more involved relation to the geometry of the vesicle [34, p. 426].

[‡]The mechanics of microaspiration has been well-known in the membrane mechanics community since at least the 1970s [29, 42]. The derivations in this section though follow the logical development as presented by [34, Sec. 11.3.1].

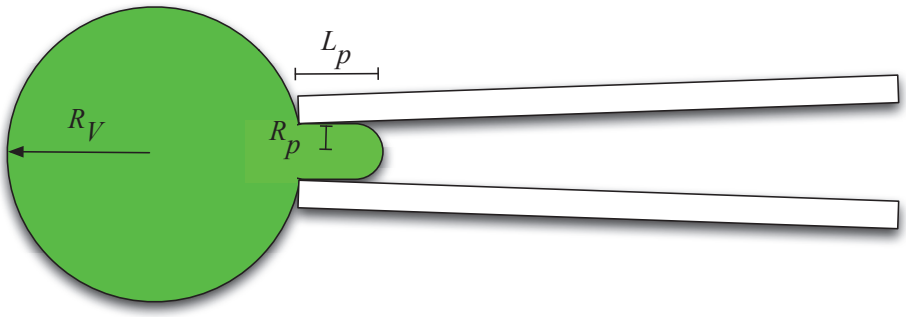

Figure 2.7 : A microaspirated vesicle of radius R_V with projection length L_p in a pipette of radius R_p.

From Equation 2.11, we know that at high tensions, $^{\Delta A}/_{A} = {}^{\tau}/_{K_A}$. So an additional connection between tension and geometry may be established. If before being aspirated, the vesicle was a sphere of area $4\pi R_V^2$, and the increase in area due to the projection of a portion of the membrane into a capped cylinder was

$$\Delta A = \underbrace{2\pi R_p L_p + 2\pi R_p^2}_{cylinder} - \underbrace{\pi R_p^2}_{patch} = 2\pi R_p L_p + \pi R_p^2, \tag{2.15}$$

where L_p is the projection length. $^{\Delta A}/_{A}$ can then be given by

$$\frac{\Delta A}{A} = \frac{1}{4}\left(\frac{R_p}{R_V}\right)^2\left(1 + 2\frac{L_p}{R_p}\right). \tag{2.16}$$

Or when combined with Equation 2.11, the tension is

$$\tau = \frac{K_A}{4}\left(\frac{R_p}{R_V}\right)^2\left(1 + 2\frac{L_p}{R_p}\right). \tag{2.17}$$

Knowing the geometry and pressure difference of the system, the tension and the areal expansion of the system may be determined. The dependence between the tension and areal strain may then be used to determine the compressibility modulus, as demonstrated by [29, 31].

2.2.5 Tether Mechanics

If a point force of sufficient strength is applied to the membrane, the membrane will undergo structural reorganization to increase the curvature of the lipids at the point by several orders of magnitude to form a tether. In an area of a few hundred

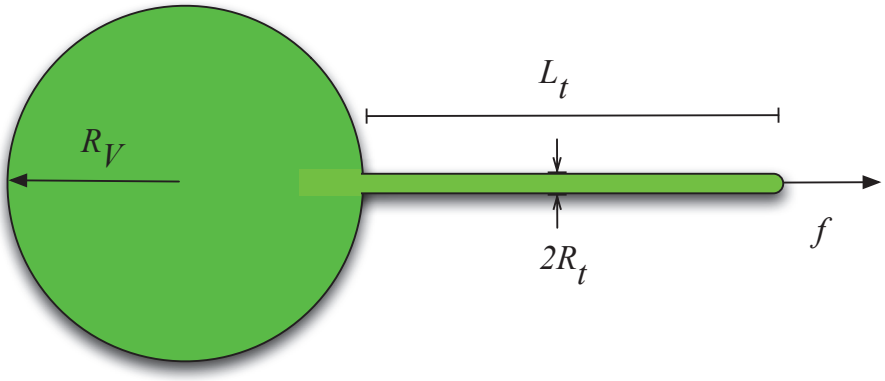

Figure 2.8 : A tether of radius R_t and length L_t being pulled off a vesicle with radius R_V by an applied force f.

square nanometers, the curvature increases from $^{10^5}/_{\mathrm{m}}$ to $^{10^7}/_{\mathrm{m}}$. The applied force will continue to draw the tether out with increasing length and decreasing tether radius. This response of a membrane to a point force may be developed purely from energetic considerations. Four energetic terms model a tethered system (Figure 2.8)[§]. First, the energy due to curvature of the membrane as a sphere, a cylinder, and a cap is given by

$$G_{bend} = 12\pi k_c + \pi k_c \frac{L_t}{R_t}, \tag{2.18}$$

where L_t and R_t are the length and radius of the tether, respectively [34, p. 428]. The constant contribution to bending energy, regardless of radius, was used to obtain the first term, while the second term resulted purely from the cylinder. Second, the energy of membrane stretch is

$$G_{stretch} = \frac{K_A}{2} A \left(\frac{\Delta A}{A} \right)^2, \tag{2.19}$$

while, third, that due to the work done against pressure is

$$G_{pV} = -\Delta p \left(\frac{4}{3}\pi R_V^3 + R_t^2 \pi L_t \right). \tag{2.20}$$

Fourth, the work exerted by the force is given by

$$G_{load} = -f L_t. \tag{2.21}$$

[§]The derivations in this section follow the logical development as presented by [34, Sec. 11.3.2].

The total energy G_{tot} is simply the sum of these four terms.

The total energy can then be minimized to determine the equilibrium state of the system. Minimizing by the vesicle radius,

$$\frac{\partial G_{tot}}{\partial R_V} = 8\pi\tau R_V - 4\pi R_V^2 \Delta p = 0, \tag{2.22}$$

yields the Laplace-Young relationship $\Delta p = 2\tau/R_V$ [34, p. 430]. Likewise, by minimizing the total energy with respect to the tether radius, the following expression is obtained:

$$\frac{\partial G_{tot}}{\partial R_t} = -\pi k_c \frac{L_t}{R_t^2} + 2\pi\tau L_t - 2\pi R_t L_t \Delta p = 0. \tag{2.23}$$

Simplifying gives a method to determine the tether radius via the tension, or more explicitly

$$R_t = \sqrt{\frac{k_c}{2\tau}}. \tag{2.24}$$

In a similar fashion to minimizing based on the radii of the system, the equilibrium of the system with respect to tether length derives from

$$\frac{\partial G_{tot}}{\partial L_t} = \pi \frac{k_c}{R_t} + 2\pi\tau R_t - \pi R_t \Delta p - f = 0 \tag{2.25}$$

and returns

$$f = 2\pi\sqrt{2k_c\tau}, \tag{2.26}$$

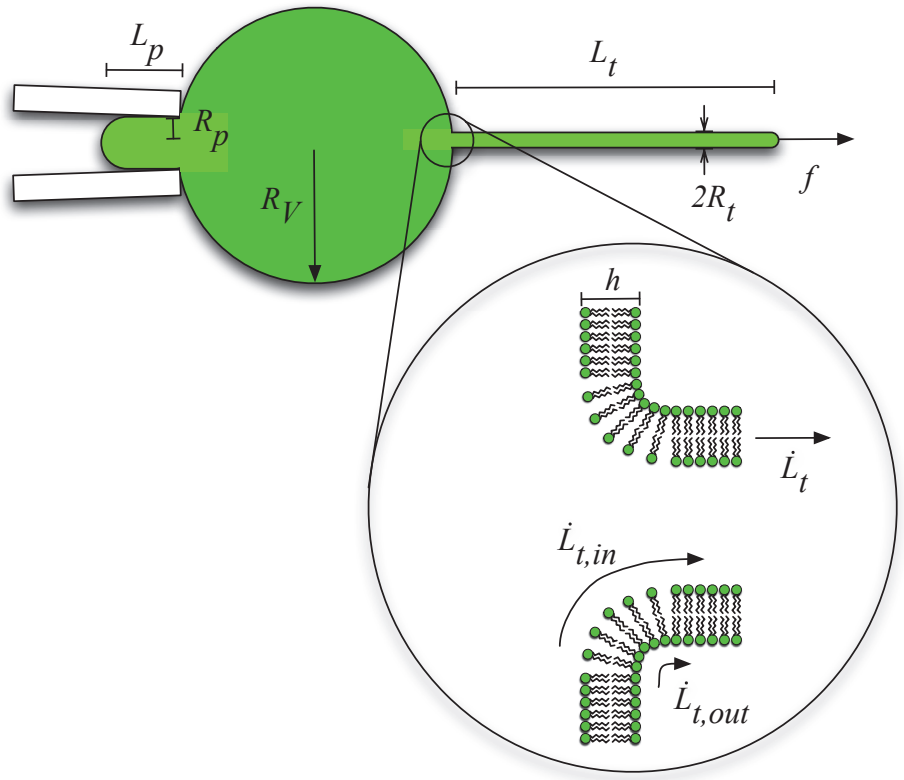

Figure 2.9 : A schematic depicting differential velocity of leaflets during tether formation. As the two leaflets must travel a different distances in the same time to maintain mass conservation, the rate of tether elongation differs between the inner ($\dot{L}_{t,in}$) and outer ($\dot{L}_{t,out}$) leaflets. Adapted from [41].

which reveals what force and tension balance the tether [34, p. 430]. Finally, Equation 2.26 may be extended to the case of a tether undergoing motion by following a thorough development as described by Evans and Yeung [41]. Image pulling a tether at a constant force rate, as in Figure 2.9. The lipids enter into the tether from the main portion of the vesicle and undergo a drastic change in curvature. The curvature experienced by the inner and outer leaflets are nonetheless different. Although the curvatures differ, mass is still conserved, leading to a differential in the rates of tether formation occurs between the inner and outer leaflets. Furthermore, the two leaflets interact with each other and with themselves to resist the flow, leading to an effective drag as the tether is pulled. The result of Evans and Yeung's work [41] is an additional term¶ related to the drag characterized by a strength b between a bilayer of width h:

$$f = 2\pi\sqrt{2k_c\tau} + 2\pi b h^2 \dot{L}_t \ln\left({}^{R_V}/_{R_t}\right). \tag{2.27}$$

As a demonstration of the general applicability of the magnetic force transducer-aspiration system, which will be discussed later, this formalism will be utilized in Section 5.4.3 to determine b for a returning tether of a lipid membrane.

2.3 Translating Energy Surfaces into Observables

Just as above, most descriptions of tether dynamics focus on the tether once it has already been formed. Other than recent studies on cells lacking an actin cytoskeleton

¶There is yet another term that Evans and Yeung derived, but at the length scales of the tethers discussed, it is negligible.

[13], work as not been done to determine how pure lipid membranes—without the influence of cytoskeletal connections—contribute to tether formation. However, with the drastic change in curvature, it is clear that a large amount of energy is required to bend the membrane, regardless of cytoskeletal influences.

In Chapter 6, we will postulate that the tether formation process may be modeled by an energy landscape characterized by two barriers. Many phenomena related to membranes, from decoupling adhesion site to vesicle rupture, can be modeled using an energy barrier model. This model was first described by Kramers in 1940 [43] and more recently discussed by Evans in relation to binding of membrane-based molecules [44][‖]. To relate energies to tether formation, we first examine the basic energy barrier model given in Figure 2.10a.

The energy landscape is described by an energy well that raises in energy E_b at the top of an energy barrier at a distance x_β. A system initially at the well minimum will surmount the energy barrier described by E_b at a rate $k_\rightarrow$, with an dependence given by

$$k_\rightarrow = \frac{1}{t_D} e^{-E_b/k_B T}, \tag{2.28}$$

where t_D is the diffusive relaxation time (which is dependent upon the diffusion in the system and the local curvature of the energy landscape). Physically, $1/t_D$ is the attempt frequency for an over-damped transition, such as in the membrane, and leads

[‖]This section is based upon the development presented by Evans [44].

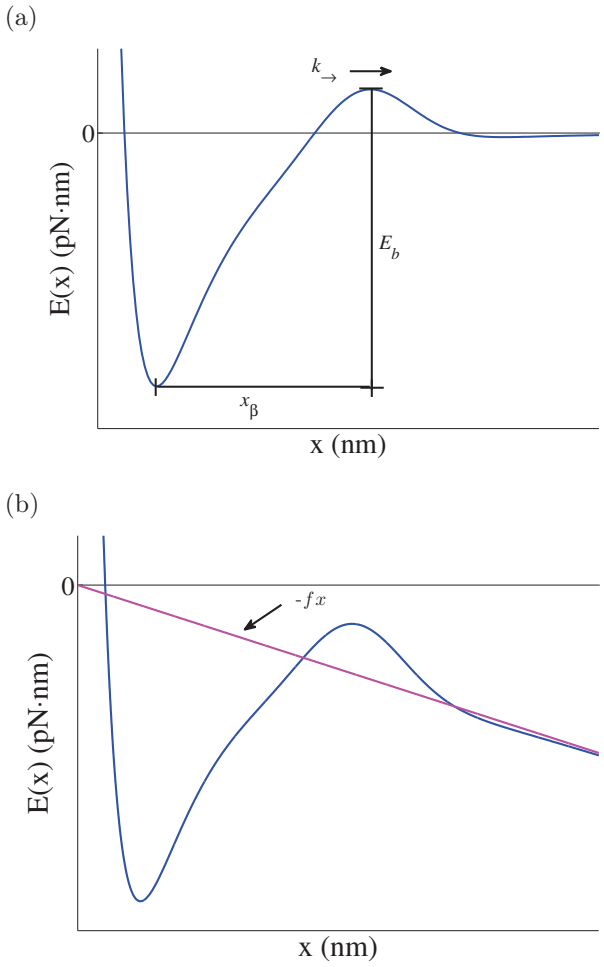

Figure 2.10 : An energy potential well with a single barrier. (a) The maximum of the barrier is a distance x_β away from the energy minimum. The rate that an event occurs that surmounts a barrier is given by $k_{\rightarrow}$ and corresponds to a barrier height E_b. (b) An applied force biases the energy by $-f\,x$, tilting the potential landscape and lowering E_b.

to thermally activated escape. $k_{\rightarrow}$ is the escape rate as it is the likeliness of reaching the top of the barrier, which drops off exponentially with the energy barrier height. k_BT—roughly $4.1\,\mathrm{pN}\cdot\mathrm{nm}$—sets the scale by which the rate of an event occurs [44]. An increase of just 1 k_BT will decrease the rate by 63%; each similar increase in k_BT will likewise decrease the rate by 63%. Returning to Figure 2.10a, an applied force f will modify the energy landscape by $E_b(f) = E_b(0) - fx_\beta$, where x_β is the position of the transition state. The force necessary to lower the height of the energy barrier at x_β by the thermal energy k_BT gives a convenient scale for the force of the system. This force f_β is given by

$$f_\beta = \frac{k_BT}{x_\beta}. \tag{2.29}$$

Using a model developed by Bell [45] and propagated by Evans, $k_{\rightarrow}$ may be related to this characteristic force through an exponential

$$k_{\rightarrow}(f) = \frac{1}{t_D}e^{-\left(E_b - fx_\beta\right)/k_BT} = \frac{1}{t_D}e^{-E_b/k_BT}e^{fx_\beta/k_BT} = \frac{1}{t_{off}}e^{f/f_\beta}, \tag{2.30}$$

where t_{off} is the reciprocal of the escape rate when the applied force f is zero [44]. t_{off}, or $1/k_{\rightarrow}(0)$, sets an opportune scale of time of the system.

If the applied force is determined by a force ramp, the force at a time t is $f = (df/dt)\,t$. The force ramp can be expressed in terms of the scaled units of the system (f_β and t_{off}) through what is called the loading rate r_f. This loading rate is

$$r_f \equiv \frac{t_{off}}{f_\beta}\frac{df}{dt}. \tag{2.31}$$

Assuming the molecules have moved passed the barrier and so diffusion becomes negligible, a return rate $k_{\leftarrow}$ may be ignored. Then according to Evans [44], $k_{\rightarrow}\left[f\left(t\right)\right]dt$ gives the probability of a system in the original state bound in the lowest potential well, shown in Figure 2.10a, making a transition out of the well in time t to $t+dt$. So the probability $S\left(t\right)$ of the system being in the bound state at time t can be approximated by the inverse of the exponential of the time-integral $k_{\rightarrow}\left[f\left(t\right)\right]dt$ from the beginning of the ramp to the time t. The time integral can be turned into an integral over force through $f\left(t\right)=\left({}^{df}/_{dt}\right)t$. This yields

$$S\left(f\right)\approx\exp\left[-\int_0^f\frac{k_{\rightarrow}\left(f'\right)}{{}^{df}/_{dt}}df'\right], \tag{2.32}$$

where f' is a dummy variable. The probability that the system leaves the original bound state in an time interval from t to $t+dt$ (or force interval from f to $f+df$) is equal to the probability of the system being bound ($S\left(t\right)$) times the probability of the system transitioning to the unbound state state $k_{\rightarrow}\left(t\right)dt$. Over a time interval from t to $t+dt$, the probability of entering an unbound state, $p\left(t\right)dt$, is given by

$$p\left(t\right)dt=S\left(t\right)k_{\rightarrow}\left(t\right)dt. \tag{2.33}$$

This probability over time can be related to probability of the system transitioning from the state S to an unbound state in a force interval f to $f + df$ by

$$\tilde{p}\left(f\right) df = p\left(t\right) dt, \tag{2.34}$$

where f and t are related by $f = \left({}^{df}/_{dt}\right) t$. As the force ramp ${}^{df}/_{dt}$ is a positive constant, $\tilde{p}\left(f\right) df$ reduces to

$$\tilde{p}\left(f\right) df = p\left(t\right) \frac{dt}{df} df = \frac{k_{\rightarrow}\left[f\left(t\right)\right]}{{}^{df}/_{dt}} S\left[f\left(t\right)\right] df = \frac{k_{\rightarrow}\left(f\right)}{{}^{df}/_{dt}} S\left(f\right) df. \tag{2.35}$$

$\tilde{p}\left(f\right) = k_{\rightarrow}\left(f\right) S\left(f\right) \left({}^{df}/_{dt}\right)^{-1}$ is the probability distribution of tether transition events as a function of f. Maximizing this expression yields an expression that can be used to find the most likely force F_{th} of surmounting the energy barrier [44]:

$$F_{th} = f_{\beta} \ln \left\{ r_f \left[\frac{\partial \ln\left(k_{\rightarrow}\right)}{\partial f} - \frac{\partial \ln\left(r_f\right)}{\partial f} \right]_{f=F_{th}} \right\}, \tag{2.36}$$

with the standard deviation of F_{th} equal to f_{β} [44]. Equation 2.36 shows that the most likely force that the system will transition from a bound to unbound state under an externally applied force ramp is related to the escape rate $k_{\rightarrow}$ and the external force ramp, manifested in this case through r_f.

For a single barrier and a constant force ramp, Equation 2.36 can be determined analytically. In this case, $k_{\rightarrow}\left(f\right) \propto e^{f}$ (from Equation 2.30), leading to ${}^{\partial \ln(k_{\rightarrow})}/_{\partial f} = 1$.

Furthermore, as $^{df}/_{dt}$ is constant, $^{\partial \ln(r_f)}/_{\partial f} = 0$. Applying Equation 2.31 yields

$$F_{th} = f_\beta \ln(r_f) = f_\beta \ln\left(\frac{t_{off}}{f_\beta}\frac{df}{dt}\right) \tag{2.37}$$

or

$$\frac{1}{^{df}/_{dt}} = \frac{t_{off}}{f_\beta} e^{-F_{th}/f_\beta}, \tag{2.38}$$

showing an explicit relationship between F_{th} and $^{df}/_{dt}$.

An intuitive model for tether formation using Figure 2.10a may be constructed in order to help understand the Evans construction. We compare the inverse of the transition rate, $^{1}/_{k_{\rightarrow}(f)}$, to the timescale on which the rate changes appreciably, Δt. Δt is defined by $(^{df}/_{dt})\, x_\beta \Delta t = k_B T$. It is the time for the barrier to decrease by $k_B T$. When the two times are equal, $(^{df}/_{dt})\, \Delta t$ is the expected force during the ramp at which a transition occurs (Figure 2.11). Below this expected force, the transition rate is low compared to the inverse of the characteristic observation time Δt. While at forces above the expected force, the rate raises significantly and the transition is very favorable.

So far, only a single barrier has been considered. However, the same derivation can be applied to multiple barriers by extending the rate as defined by Equation 2.30 to take into account the time to surmount each barrier, namely

$$\frac{1}{k_{\rightarrow}} = \sum_i t_{off}(i)\, e^{-f/f_\beta}, \tag{2.39}$$

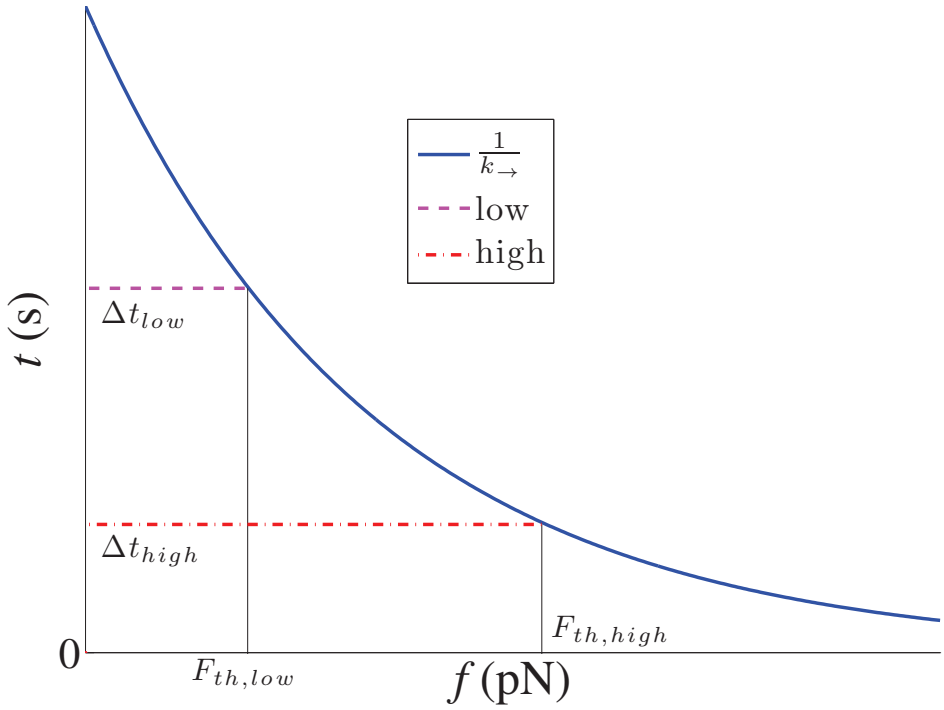

Figure 2.11 : An intuitive model to describe how the apparent threshold force, F_{th}, was determined by the force ramp, $^{df}/_{dt}$. At a low force ramp $(^{df}/_{dt})_{low}$, a time scale characteristic of the observation time (magenta dashed line) can be determined by the force ramp, $\Delta t_{low} = (^{k_B T}/_{x_\beta})\,(^{df}/_{dt})^{-1}_{low}$. When Δt_{low} intersected $^{1}/_{k_{\rightarrow}}$ (solid blue line), the time scale for the state to transition, a tether pulled at a low measured force threshold $F_{th,low}$. At higher force ramps, however, Δt_{high} (red dash-dotted line) crossed $^{1}/_{k_{\rightarrow}}$ at a higher observed force threshold $F_{th,high}$.

where i denotes the ith barrier. Applying Equations 2.36 and 2.31 to Equation 2.39 yields

$$\sum_{i}^{n} \frac{t_{off,i}}{f_{\beta,i}} e^{-F_{th}/f_{\beta,i}} = \frac{1}{df/dt}. \tag{2.40}$$

This expression consists of two observables, df/dt and F_{th}, which will be used in Chapter 6 to determine the values t_{off} and f_{β} that describe the energy landscape of tether formation.

While we will apply a two barrier model to approximate the relationship between df/dt and F_{th} during tether formation, the model is not limited to force dynamics. Evans *et al.* used a similar development to represent how the rupture tension of an aspirated vesicle depended upon the rate at which the tension increased. In their model, the barriers corresponded to defect-limited and cavitation-limited regimes and differed in height by $3\,k_BT$ [14]. The two barrier model is thus generalizable to a variety of different membrane mechanical phenomena.

2.4 Summary

This membrane primer established the foundational knowledge for the rest of the thesis. It began by introducing a variety of biological macromolecules essential for proper membrane function. In particular, various types of lipids and the phase behavior during mixing was reviewed. A development of some aspects of the mechanical properties of membranes followed: curvature and compressibility. The concepts ap-

plied to a vesicle led to the the physics governing both microaspirated vesicles and tethers. The mechanics was followed with an interpretation of energy barriers, along with a practical example of the analysis. This chapter has recapitulated the physical concepts relevant for interpretation in the rest of this work.

Chapter 3

Review of Various Magnetic Force Applicators

I am busy just now again on electro-magnetism, and think I have got hold of a good thing, but can't say. It may be a weed instead of a fish that, after all my labor, I may at last pull up. - Michael Faraday [46]

Over the years, many devices have been designed and built to exert forces on micro-scale biological material. Some of these tools include the optical trap, the atomic force microscope, flow chambers, and magnetic tweezers. In the following section, we examine the development of magnetic tweezers further from macroscopic permanent magnets to microscopic electromagnets. The benefits and drawbacks of each will be discussed and illustrated through relevant experiments.

3.1 Macroscopic Permanent Magnets

The first post-war application of magnetic forces to microscopic biological systems was developed by Crick and Hughes in 1950 [47]. They created a device consisting of large U-shaped permanent magnets made of Alcomax, a magnetic alloy. The magnets consisted of roughly $4\,\mathrm{cm}^2$ square faces with about 2 cm separation and over 10 cm in inner perimeter, which generated an H-field of between $1.6\,\mathrm{kA/m}$ to $64\,\mathrm{kA/m}$ [47]. The H-field concentrated down a tapered iron pole and exerted a force on microscopic ground particles composed mostly of magnetite or iron oxide that had been taken

up by frontal bone of chick embryos. While they were unable to obtain quantifiable results of force application in the system due to the forces being too low, Crick and Hughes did show qualitatively that forces could be exerted within living cells and that these cells could take up magnetic material without damage [47].

Eventually, scientists developed techniques to apply magnetic forces more systematically and applied these to biological systems. Strick *et al.* fabricated a system consisting of two large cobalt-samarium magnets with a 2 mm gap that could rotate about the sample within a microscope to apply torsion to super-coiled DNA [48]. As the DNA uncoiled, the extension of the DNA and the force required to obtain this extension were measured. Application of forces from 0.01 pN to 10 pN lengthened DNA up to 100% with very high sensitivity to the force [48]. Such experiments have been useful for determining the mechanics of DNA winding, but have proved difficult to calibrate as they depend upon visualizing fluctuations of microscopic samples undergoing Brownian motion, which demands high magnification (and short working distance) optics.

Although straightforward, permanent magnet systems are only slowly adjustable. Additionally, it is difficult to machine permanent magnets in order to simultaneously obtain high magnetic field gradients and high magnetic field magnitudes. This competition leads to a smaller range of applied forces than can be obtained with the designs presented below.

3.2 Macroscopic Magnetic Tweezers

Macroscopic magnetic tweezers extended the methodology of permanent magnets by using a solenoid, or wrappings of current-carrying wires, to generate a magnetic field. Making use of a material with high magnetic permeability, such as iron or Permalloy, the magnetic tweezers directed the magnetic field to a tapered tip. This tapered tip leads to larger forces as compared to permanent magnets; using currents also modulated the force generated. Below, I present some of the significant work in macroscopic magnetic tweezers in this section and mention some of their shortcomings.

As with permanent magnets, Crick and Hughes were one of the pioneers of the application of electromagnets, or magnetic tweezers, to biological systems [47]. They wrapped a core composed of μ-metal, a material with high magnetic permeability, with a solenoid. The core was of similar dimensions as the U-shaped magnet, while the solenoid contained almost 1000 wraps of wire. The design enabled H-fields of up to $6.2\,{}^{\mathrm{kA}}/_{\mathrm{m}}$ to be obtained. While lower than that of permanent magnets, the local gradients were higher, producing greater force. By rotating the H-field, much as Strick *et al.* would do later, torsional experiments on embryonic chick bone cells determined the rigidity modulus of cytoplasm to be on the order of 10 Pa [47].

After Crick and Hughes, large electromagnetic devices were used to examine viscosity within amoeba [49], and the rheological properties of axon cytoplasm in squids [50]. In one of the more recent significant applications of an electromagnet to study cell mechanics, Wang *et al.* applied an electromagnet to conduct torsional experiments

on cell surface receptors to examine mechanotransduction through the cell cytoskeleton [51]. Rotated magnetized beads on the cell surface exerted pressures of 7 Pa (with a resolution of about 1 Pa), activating cellular mechanical responses. Brief pulses of up to 40 times higher field were possible if pulses lasted 10 μs [51], but advanced waveforms were not applied. Detailed examination of the force field would have also required numerical methods.

Using more more sophisticated control and data acquisition techniques, Heinrich and Waugh developed an electromagnet consisting of an iron core with a solenoid [52]. Furthermore, they combined this iron-core based electromagnet with microaspiration, a method to hold cells with constant tension, in order to study several mechanical properties of vesicles: equilibrium force dependence on tension and the local bending modulus. The force at which a tether maintained equilibrium, f, was found to follow the relation (for tethers of a few tens of microns or less):

$$f = 2\pi\sqrt{2k_c\tau}, \tag{3.1}$$

where k_c is the local bending modulus, and τ is the membrane tension. Further, k_c was found to be 1.2×10^{-19} J [52]. While it was a novel use of a magnetic device, the magnetic profile of Heinrich and Waugh's magnetic tweezer is difficult to model due to the complicated geometry and with its high reactance, its frequency range is limited.

Using a similar design of an iron core-based solenoid with a tempered tip, Bausch

et al. were able to exert nanonewton (nN) forces on magnetic beads bonded to the membrane of fibroblasts. By fitting a Voigt profile—which is indicative of viscoelastic behavior—to the trajectory of the creep of the membrane, they were able to calculate the viscoelastic properties of the membranes of fibroblasts, including viscosity [53]. While it could apply forces up to 600 pN, this electromagnet did not have the H-field resolution needed to exert piconewton level forces.

In an extension of the work of Bausch *et al.,* Huang *et al.* developed a large quadrupole electromagnet that could apply forces of up to 800 pN over a $0.5x0.5\,\mathrm{mm}^2$ area with less than 10% variation [54]. With the quadrupole design, the electromagnet could exert forces in two dimensions over the large area. In combination with a two-photon microscope to image in three-dimensions, the electromagnet was used to track long term cell response from a steady, large, directional force. While very useful for investigating bulk motion over many cells or tissue, the device exerted no less than 50 pN and was used only in long pulse modes. The electromagnet of Huang *et al.* applied to large systems but was not suitable to measuring small forces at high force rates.

Finally, Hosu *et al.* built an iron core solenoid with several layers of wrapped coils to generate forces [55] that was similar to the design of Heinrich and Waugh but with a more compact design and greater fields. The forces generated by magnetic beads attached to Chinese hamster ovary and human brain tumor cells formed tethers which were subsequently released individually [56]. The release was studied not only with

magnetic tweezers but also with atomic force microscopy and electron microscopy. The magnetic tweezers and atomic force microscope were used to quantify, using a multi-element Voigt model, the viscoelastic properties of the two cell types as each tether detached from its respective magnetic bead. The electron microscope imaged the tethers, verifying that multiple, individual tethers had formed [56]. Although Hosu *et al.* followed the trajectories as the tethers extended, they did not examine the dynamics of formation itself. Further, as the cells were imaged on a 2-D surface, the membrane tension was not controlled, limiting the extent to which membrane mechanical properties could be determined.

Macroscopic magnetic tweezers improved upon permanent magnets by being able to develop larger forces and modulate the force generated. And in combination with advances in acquisition and control, the use of magnetic tweezers enabled the measurement of several membrane mechanical properties, including bending modulus and viscosity. Due to a large reactance, however, frequencies of at most 10 Hz were applied in any of the reviewed work. The forces are also often onerous to model and are delocalized.

3.3 Microfabricated Magnetic Tweezers

Due to advances in microfabrication techniques, macroscopic magnetic tweezers have been miniaturized to sub-millimeter scales, addressing some of their disadvantages. For instance, smaller magnetic tweezers exhibit a much higher bandwidth, due to

lower reactances and more localized field gradients. This section describes some of these devices, details their application, and suggests some areas for improvement.

The laboratory of Johannes Kanger fabricated a microscale magnetic tweezer made of cobalt to focus fields generated using standard electromagnets [57]. This four-pole device exerted between 500 pN and 2500 pN on a 5 μm ferromagnetic bead when calibrated [57], while a similar three-pole design exerted 30 pN to 1000 pN on a 3 μm ferromagnetic bead [58]. These high forces were sufficient to move beads within a cell, which completed the work attempted by Crick and Hughes. Using a viscoelastic, or Voigt, model, de Vries *et al.* deduced that the viscosity of objects within a cell depended upon the particle size, thus verifying the mesh model of the cellular cytoskeleton [58]. While it was used to ascertain interesting biophysical properties about the cytoplasm, this device required numerical methods to solve the force profile, which complicated the description of the forces. Furthermore, the magnetic tweezer was sensitive only to ~ 10 pN.

While it does not simplify the description of the forces, a hexagonal array of thin Permalloy foil that had been laser-machined down to about 100 μm provided forces of up to 13 nN that was sufficiently strong to observe nucleosome disruption events of chromatin [11]. To accomplish this Fisher *et al.* applied forces in three dimensions to a chromatin complex using the field generated by a solenoid focused through the foil. In addition to the high forces, the tweezer could apply forces that varied at higher frequency as the system experienced lower eddy currents [11]. While

it was an impressive device, its force resolution appeared to be on the order of several piconewtons while the force also had to be numerically determined. Further, such an elaborate system was difficult to construct.

In an intriguing variation of the pattered tweezers, Henighan *et al.* patterned an array of Permalloy disks of about 10 μm by 40 nm [59]. With an applied magnetic field from several sets of solenoids, the disks induced forces of up to 25 pN on 3 μm paramagnetic beads. The beads then translated cells from disk to disk [59]. The system developed by Henighan *et al.* demonstrated the ability to direct the motion of a multitude of cells individually but unfortunately, they did not study the effect of this force on biophysical properties even though the device should have been capable of such studies.

Microfabricated magnetic tweezer systems improve upon the larger tweezer designs by displaying much higher frequency responses, by exerting strong localized currents, and being able to integrate into a wider variety of biological instruments (due to their smaller size). However, the magnetic forces must often be numerically determined using finite element models, which requires time and is less accurate. Moreover, the devices may be difficult to fabricate and force sensitivity seems limited to a few piconewtons.

3.4 Microfabricated Electromagnet Wires

Improving upon the previous magnetic tweezer designs, microfabricated electromagnets based on wires have been modeled analytically and have been much more straightforward to develop. They also exert forces with sub-piconewton resolution. In the following paragraphs, I review some of the devices, discuss their limitations, and end by explaining how my own device builds upon these electromagnets.

As Henighan *et al.* developed a magnetic tweezer to translate cells, Lee, Purdon, and Westervelt fabricated an array of microscale electromagnets to do the same [10]. Each electromagnet comprised of an 8 μm by 100 μm gold layer that was a few hundred nanometers thick and conducted up to 150 mA. This current created forces of up to 40 pN on 3 μm paramagnetic beads attached to *Saccharomyces cerevisiae*—baker's yeast—cells [10]. While capable of manipulating many cells, addressing individual cells was difficult as fields crossed and neighboring wires affected the local magnetic field. In order to move single cells, Lee *et al.* made a similar design of separately addressable microfabricated coiled wire pads, which was further combined with a microfluidic device to allow cells to flow [60]. This device further maintained physiological temperatures with built-in temperature sensors and thermoelectric coolers using feedback. Although they fulfilled their purposes, neither device formed the basis of biophysical studies of the application of force upon cells. The devices additionally required numerical methods to solve their magnetic force profiles, and while the response of the thermoelectric may be very quick, it is not clear that the substrate

would conduct heat quickly enough to be effective on the scale of a few hundred microseconds.

Though they have not been applied to biological systems either, microfabricated electromagnets built from solder have been well-described analytically [61, 62]. These electromagnets formed a patterned pair of wires and generated magnetic fields from wire-induced forces, to sub-piconewton resolution, that acted as a sorter for a microfluidic device, without excessive heating (due to the large wire size) [62]. The device further helped Shevkoplyas *et al.* determine the initial magnetization of superparamagnetic beads [61], which had generally been considered to be negligible. This straightforward system was well described analytically but only exerted small forces of two to three piconewtons and has not been applied to biological systems.

Though microfabricated electromagnets exhibit ease of modeling and production, compared to more traditional magnetic tweezer designs, such systems have not, to the best of our knowledge, been combined with microaspiration to study the membrane mechanical properties of lipid membranes. In this thesis, the development of such a device is presented, and its incorporation with pipette aspiration, to study the dynamics of tether formation and other biophysical properties of vesicles.

Chapter 4

Microfabrication of a Magnetic Force Transducer

Most people spend more time and energy going around problems than in trying to solve them. - Henry Ford [63]

SEVERAL criteria determine the design of the microfabricated magnetic force transducer (MFT). First, it must be of low cost. Second, the force profiles must be of a simple form. Third, the forces must be dynamically alterable. Fourth, the MFT must be integrable with a variety of microscopes. These criteria guide the device design.

Microfabrication of the MFT followed nine steps. These steps were substrate cleaning, metal evaporation, resist spreading, soft-baking of the resist, photolithographic exposure, post-exposure baking of the resist, resist developing, electroplating, and finally lift-offing and etching. While this list may appear daunting, each step is straightforward and will be thoroughly discussed below. Before discussing methods, however, we describe the materials for the fabrication of the MFT below*.

*Much of this chapter is based upon Stark [64].

4.1 Materials

4.1.1 Resists

Developing an MFT requires the use of the photoresist SU-8 2015. SU-8 2015 (Microchem, Newton, MA) is a negative photoresist, that is the resulting pattern is the inverse of the mask used during photolithographic exposure. To obtain the required thickness of the gold wire during the later electroplating step, the SU-8 2015 must be spread to a thickness of 40 μm. To obtain this thickness, one to three milliliters of SU-8 2015 are poured to completely cover the substrate, and so supplies last several months. However, as SU-8 2015 is very viscous, it requires a spreading cycle when spinning. On a separate note, we have not observed degradation of plastic flasks due to SU-8 2015, which occurs with other resists, such as the positive photoresist S1813.

The reader should also be aware that several other resists are available to obtain other device characteristics. They will not be discussed in this chapter though. Some of these other resists are variants in the SU-8 series (such as SU-8 2, 25, and 50) that result in other resist thicknesses. Additionally, the AZ series from Microchemicals is often used for very fine features. Finally, S1813 is a very common positive photoresist and is discussed more fully in Appendix E.

Occasionally, it is necessary to remove resists. All resists can be removed with long enough exposure to acetone and agitation from an ultrasound. Toluene and acid etches (such as piranha) can also remove resists; however, they are much more aggressive towards other materials, such as plastics or metals, thus making them less

suitable for use in this experiment [64].

4.1.2 Substrate

In order to integrate into a microscope, a substrate was required that is optically transparent and polishable. To ensure electric current passes only through the electroplated wire, the substrate must be electrically insulated. Finally, as the current passing through the gold wire generates much heat, the substrate should be thermally conducting and not susceptible to fracture upon local heating. Sapphire satisfies these requirements [65]. The substrates used in this work were 1.5 in by 2 in by 1 mm (Swiss Jewel, Philadelphia, PA), allowing enough room to create the MFT and dissipate enough heat to keep temperatures in the device physiological.

There are also several other materials available that could have been used as a substrate but failed to satisfy one of the criteria specified above. Pyrex is optically transparent, electrically insulated, inexpensive, and machinable. However, it is not a good heat conductor. Aluminum nitride has a thermal conductivity that is about 4.5 times higher than that of sapphire and may be cleaved with a diamond scorer. However, it is optically opaque and is slightly more expensive than sapphire. Silicon is also commonly used as a substrate for microfabricated electronic devices, but is opaque [64]. Given these drawbacks, none of these other materials were more suitable than sapphire as a substrate.

4.1.3 Metals

To provide a seed layer for electroplating, two metals, titanium and gold, will be required for evaporation. The clean room at Rice University uses titanium as an adhesive in the evaporator. This titanium is provided for free by the clean room. Without its use as an intermediary between the sapphire substrate and the gold seed layer, the gold layer is easily scratched off. Chromium is also a common intermediary in clean rooms; however, due to concern of contamination of magnetically sensitive samples that other groups prepare, chromium is not used at Rice [64].

Gold was used to form electrodes because of its high electrical conductivity. It is also biologically compatible while inert to most solutions. To ensure the highest electrical conductivity possible, 99.999% pure gold suitable for the evaporator (vapor deposition grade) is used and may be obtained from Cerac (Milwaukee, WI). Glassy carbon crucible liners, necessary for holding the gold within the evaporator, may be purchased from Kamis (Mahopac Falls, NY).

4.1.4 Photolithographic Mask

We buy chrome masks, necessary for defining the pattern in photoresists, from Fineline Imaging (Colorado Springs, CO) with care taken to get a negative mask for use with SU-8 2015. Transparency masks may also be obtained from Fineline or another print shop for a lower cost than a chrome mask. However, the resolution is not as high, leading to a poorer quality microfabricated structure. Chrome masks may also

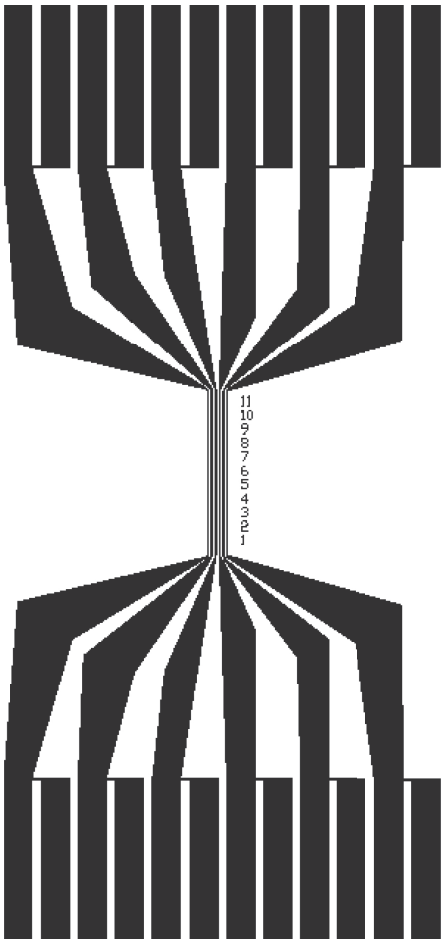

Figure 4.1 : The chrome mask used for photolithography. The dark portions of the mask will lead to areas of the resist that will be developed away, allowing access to the seed layer for electroplating. The light portions correspond to areas will the resist will not be developed away or electroplated. The number along the edge of the wire provide positing information while observing the final wires under a microscope.

be manufactured in the Rice clean room but is cost prohibitive due to the cost for the large patterns desired [64]. A schematic of the mask for this work is shown in Figure 4.1. The dark portions in the figure correspond to the areas of the chip that will be electroplated; light areas will not eventually be electroplated. With care, a well designed mask is the first step to a properly functioning device.

4.1.5 Fluid Chamber

Polydimethylsiloxane (PDMS) from Dow Corning (Midland, MI) forms the chamber that holds the vesicle solution. The PDMS consists of a 10:1 ratio of base to activator, which ensured mechanical flexibility and strength. A thickness of 1 mm keeps enough surface tension in the device to keep the fluid contained while allowing enough access to manipulate vesicles. A razor or an X-acto knife slices through the PDMS easily for custom shaping of the chamber.

4.1.6 Electrical Connections

Standard 16-gauge wire connects the pads leading from the MFT to the external current supply. The wire, which has its ends stripped, is held in place using a custom Delrin structural support. Other connection methods, such as using spring probe pins, could not carry sufficient current (up to 3 A) before overheating. Similarly to probe pins, the wires for wire-bonding were too thin and were additionally difficult to bond to the gold surface. Other alternatives were found to be too expensive (indium-based solder), too corrosive to gold (tin/lead-based solder), or too prone to spread

without much mechanical strength (silver-based conductive epoxy).

4.2 Methods

Creation of the MFT starts with cleaning the substrate, forming a seed layer, and spreading a uniformly thin layer of SU-8 photoresist. An SU-8 wire guide is then patterned atop. SU-8 resist is used to form the channel due to its ability to pattern structures tens of microns tall and due to its mechanical strength once fully cured. Patterning, itself, consists of several steps including spinning, baking, aligning, and developing [64]. Each step is discussed below and is based upon the datasheets provided by Microchem for SU-8 2015 [66]. Finally, gold is electroplated onto the seed layer, forming the wires, and excess material is stripped away.

4.2.1 Cleaning the Substrate

In order for a layer of either titanium or photoresist to adhere to the sapphire substrate, the substrate must be cleaned of any particulate or organic matter. A 10:1 (v/v) H_2SO_4:H_2O_2 (otherwise known as piranha etch) cleaning for five minutes at 100 °C eats away most organic residue and several inorganic compounds [67]. One should be wary when using a piranha etch as it is very reactive and exothermic. One should use nitrile masks, gowns, glassware, and gloves when working with piranha. Further, it should be disposed of in an acid waste container. After this strong cleaning, heating the substrate in acetone for 5 minutes at 100 °C removes any remaining

organic residue on the substrate. Spraying the substrate for thirty seconds with IPA removes acetone residue; spraying for thirty seconds, thereafter, with methanol removes the IPA residue. Finally, blowing the methanol off the substrate with nitrogen gas, placing the gas stream parallel to the substrate, leaves the substrate sufficiently dry and clean for further use. Baking the substrate at 100 °C for 30 min after cleaning may also be necessary to remove water which has adhered to the substrate surface [64].

4.2.2 Evaporating

After cleaning the substrate, a seed layer (see Figure 4.2) must be evaporated onto it in order to form the basis of the later electroplating step. To evaporate metal onto the wafer to form electrodes, a Sharon electron-beam evaporator was used. The Sharon electron-beam evaporator consists of three main units: the vacuum chamber, the high voltage supply, and the control unit. The vacuum chamber is where the substrate and gold source are placed and where the evaporation takes place. The high voltage supply[†] provides several kilovolts in order to accelerate electrons from the electron gun. The electrons strike the source material, giving their energy to a metal atom, which then evaporates [64]. The evaporated atom then condenses on the sapphire substrate, forming the thin film. Finally, the control unit contains the software for setting the evaporation program, the source being used, and the shutters.

Evaporation is a vital step for creation of the device, but it is also an expensive

[†]Because of the high voltage, care should be taken not to touch the leads.

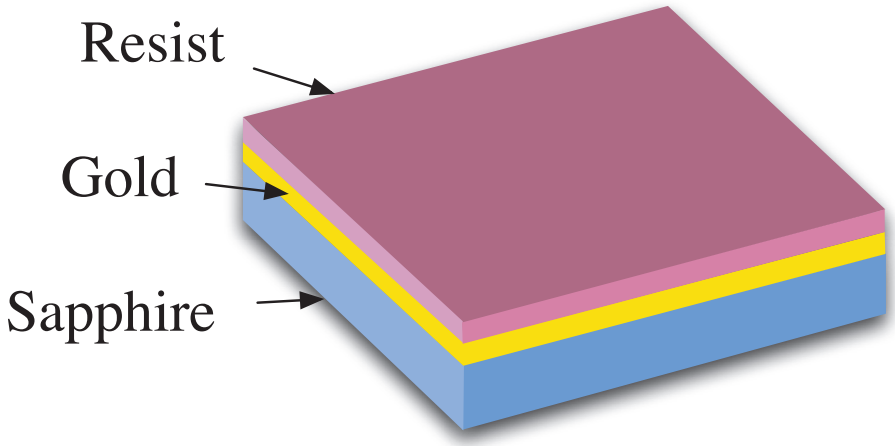

Figure 4.2 : Deposition on a sapphire substrate. The 100 nm-thick layer of gold adheres to the sapphire substrate via a 10 nm-thick layer of titanium (which is not shown as it is very thin); both layers are formed through evaporation. The SU-8 2015 photoresist is spread on top of the gold to a uniform thickness of 40 μm to form a uniform layer suitable for patterning.

step. While the metal evaporates, it not only coats the sapphire substrate, but also the inside of the vacuum chamber. Therefore, much of the source material is wasted. For example, assume one evaporates 50 nm of gold (molecular weight 19.3 g/cm^3) onto a substrate. Then, since the area of the evaporation chamber that is evaporated upon is about 1 square meter, each run uses $50\,nm * 1\,m^2 * 19.3\,g/cm^3 = 0.965\,g$ of material. As a 25 gram source is typically used, 10-20 runs can be done conservatively.

During a general run on the evaporator, 10 nm of titanium is put down at 1 Å/s followed by 100 nm of gold at 2.0 Å/s. 10 nm of titanium provides a very strong adhesion layer for the gold. A thinner layer often leads to gold flaking or scratching off at unwanted times. Putting on 10 nm also ensures that the deposition rate steadies at 1 Å/s, establishing a more uniform–and lower resistance–layer. The thick gold, as noted above, provides a low resistance layer [64].

There are a variety of issues one should be aware of when using the evaporator. First, the evaporator costs $10 per use during main hours plus the cost of materials. Also concerning costs, as many pieces as possible should be put in the vacuum chamber during one run to avoid wasting material. Always ensure that the substrate shutter does not hit the substrate or substrate support plate by screwing the substrate support plate tightly to the evaporator. If it is hit, the substrate may fall during the middle of the run. In addition to causing possible damage to the evaporator, a fallen substrate needs to be removed and possibly put back into place, necessitating waiting for several more hours while the vacuum chamber pumps down. Finally, the clips

holding the substrate onto the substrate support plate create shadows on the substrate, or areas where the evaporated metals do not fall. Any designs should allow for shadows.

Evaporation of titanium and gold form the seed layer on the sapphire substrate. With a patterned resist to guide electroplating, a gold wire will be formed.

4.2.3 Spinning

In order for a mask to form a pattern in photoresist with constant exposure, the photoresist must be uniform in thickness. Uncured photoresist is a solution of monomers and solvent resulting in a certain viscosity. If spun at a specified velocity for a certain amount of time, the resist spreads uniformly in a reproducible manner. A spinner accomplishes this task by revolving the substrate with photoresist atop at predetermined high speeds for set times.

To form a 40-micron-thick film of SU-8 2015, as diagrammed in Figure 4.2, pour three milliliters of resist onto a substrate centered in the spinner. As SU-8 2015 is viscous, one should ensure that the entire substrate is covered before spinning. Despite this precaution, SU-8 2015 still requires a spreading cycle of 500 rpm for 5 seconds with a 100 rpm/s ramp. The spinning cycle is 1600 rpm for thirty seconds with a 300 rpm/s ramp, and if the substrate is not completely covered, one should clean the substrate with acetone, IPA, and methanol and spin again [64]. Further, if SU-8 2015 does not adhere, and cleaning the substrate as already described is not

sufficient, applying a coat of Omnicoat—a very viscous resist from Microchem—may act as an adhesion layer for SU-8. Omnicoat does provide a good adhesion layer, but can be difficult to remove during the later lift-off step. And as should be noted for every fabrication step, times and temperatures of any step vary depending on the desired thickness.

Spinning ensures a proper thickness of resist, leading to proper straight gold wires after electroplating.

4.2.4 Soft-baking

After spinning the resist, it still is not photosensitive. To make the resist photosensitive, the solvent within the resist must be removed by heating the substrate to evaporate the solvent. This procedure is called soft-baking.

To soft-bake SU-8 2015, heat the substrate to 65 °C for two minutes. Then increase the heat to 95 °C for five min and allow the substrate to cool to room temperature. Gradually raising and lowering the temperature reduces forming stress on resist due to heat shock.

4.2.5 Exposing

Once the photoresist has become photosensitive, one can expose it to ultra-violet light to destroy bonds in the resist, which leads to crosslinking of the individual resist monomers to eventually form a solidified polymer. The Rice cleanroom uses 365 nm light from the Süss aligner to photo-activate the resist. As seen in Figure 4.3, these

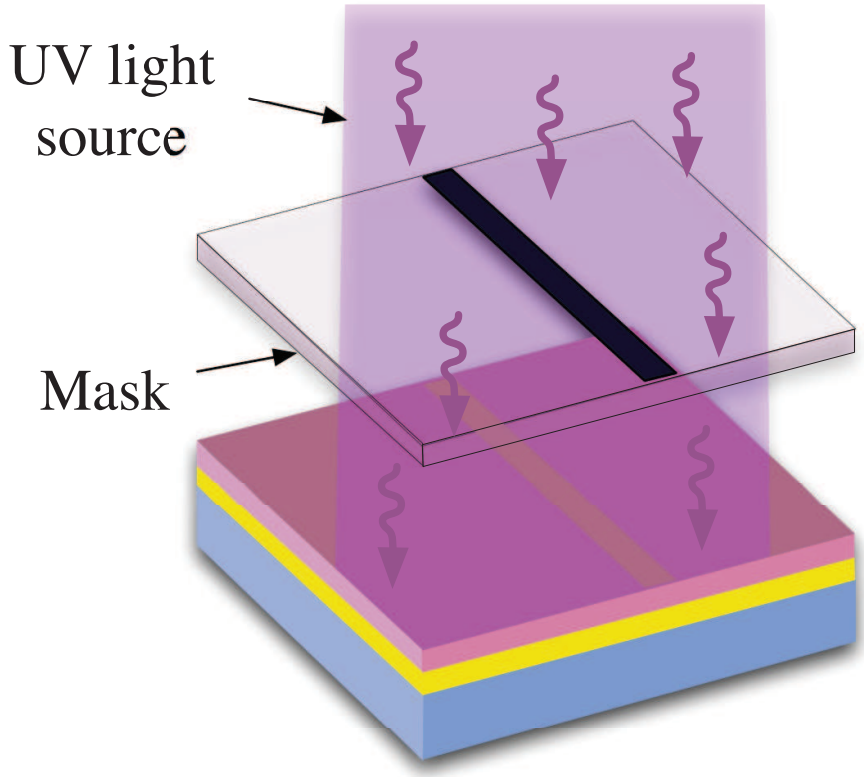

Figure 4.3 : Pattern transferred to photoresist. The UV light from an aligner initiates a photochemical reaction in exposed resist. The shadows due to the pattern in the mask are thus transferred, leading to the eventual microfabricated structure in the resist.

exposed areas become the transferred pattern from the mask to the photoresist. The unexposed areas will form a barrier to electroplating; the electroplated wires will only form in the channels formed in the resist. The Süss aligner comes with a manual, so only tips and concerns shall be covered here.

4.2.5.1 Alignment

To properly expose the resist, with proper patterning, the substrate must be correctly positioned. Positioning is accomplished with the use of alignment marks, of the Weight Error Correction (WEC), and of substrate evenness.

In order to ensure that a pattern is aligned correctly over the substrate, make sure the pattern has several widely-spaced alignment marks [64]. Then use both of the attached objectives on the microscope on the Süss aligner to see both alignment marks simultaneously. By adjusting the x-y position and rotation angle of the piece to align the marks, the substrate across the entire pattern will be aligned.

The WEC setting adjusts for the varying weights of substrates used in the aligner. If adjusting the WEC setting is skipped, the substrate will be too far from the mask and finer features will not come out. Further, larger features may be of different dimensions than designed. If the WEC setting is not skipped, but fine features still do not come out, then do not turn the WEC knob the full two rotations counterclockwise as directed when bringing it flush to the substrate. The aligner may give an error, but finer features may come out. If the substrate is too close to the mask, it may

stick. While stuck, the substrate will not move in a smooth manner but will rather move jaggedly, making aligning difficult.

If the substrate is not parallel to the mask, then the resist will not be uniformly exposed. The resulting pattern will not properly develop. Unevenness of the substrate will result from tape, resist, or other material on the mask or from uneven coverage of the O-ring that seals the substrate to the aligner.

The substrate may be aligned in all three spatial directions and parallel to the mask through alignment marks, weight error correction, and substrate evenness. Doing these alignments ensures that a properly position pattern will be formed.

4.2.5.2 Timing

A well-formed micropatterned resist is sensitive to more than correct alignment; it is also sensitive to the total time exposed to ultraviolet light. Different resists and different resist thicknesses require diverse amounts of UV exposure in order to break all necessary bonds within the resist. Given the reflectivity coefficient α_{refl} of the surface of a substrate, the power flux P/A emitted by the UV source, and the exposure dose E/A needed, the exposure time τ_{fab} can be estimated by [64]

$$\tau_{fab} \approx \frac{1}{\alpha_{refl}} \frac{E/A}{P/A}. \tag{4.1}$$

For example, the reflectivity coefficient for gold is 2. The exposure dose for SU-8 2015 at $40\,\mu$m is about $250\,\mathrm{mJ/cm^2}$, and the power flux is usually around $20\,\mathrm{mW/cm^2}$.

These values yield a τ of about 6.25 sec. The exposure time may need to be adjusted if features are over- or under-cut but generally does not need to be [64].

Over- and under-cutting results from an exposure time that is too short or too long. In this situation, the sides of the pattern wall will not be normal to the substrate surface; they will be slanted. If the pattern is wider at the bottom than at the top, it is undercut. If it is thinner, it is over-cut. Being over- or under-cut can lead to structures with widths that are different than expected [64]. Additionally, depending upon the resist, improper exposure can cause cracking or keep resist from fully developing. Proper exposure times, however, lead to fully developed channels with orthogonal walls.

4.2.6 Post-Exposure Bake

Some resists, such as SU-8 2015, require a bake after exposure in order to drive an acid-catalyzed reaction that alters the solubility of the polymer in a developer [64]. The post-exposure bake (PEB) also causes some slight diffusion of the resist, which lowers interference effects. For a 25-micron-thick film of SU-8 2015, a bake at 65 °C for two minutes followed by a one minute bake at 95 °C activates the acid-catalyzed reaction enough for proper development. Under-baking may lead to the resist not solubilizing enough for proper developing, while over-baking may lead to it becoming too soluble.

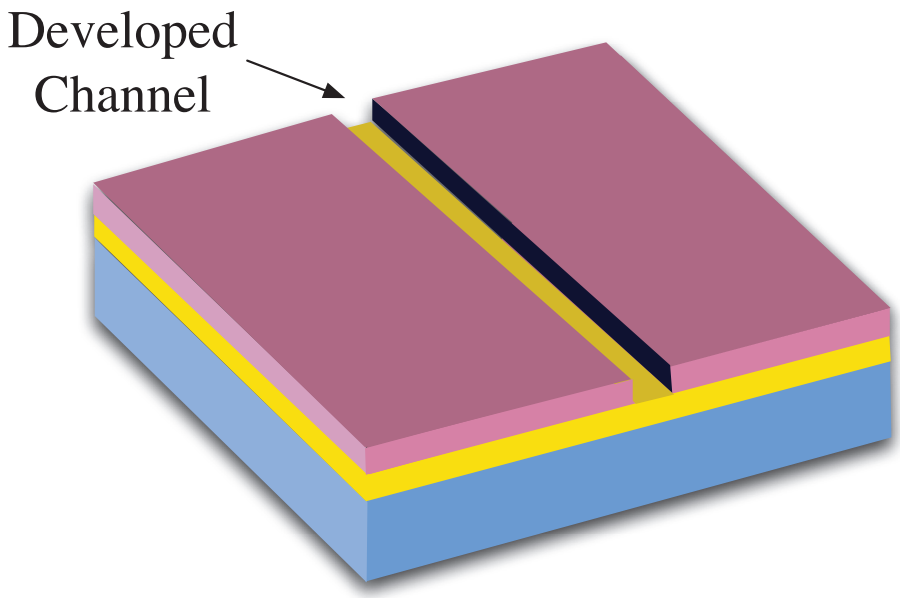

Figure 4.4 : A schematic of the substrate with patterned photoresist. The developer dissolved the non-crosslinked resist, leaving a channel that may be used to guide the growth of an electroplated wire.

4.2.7 Developing

After crosslinking, developing solubilizes non-crosslinked resist. Thus, for SU-8 2015, unexposed resist dissolves, leaving a negative pattern [64]. To develop the SU-8 2015, the entire substrate should be put in SU-8 Developer (Microchem) in an ultrasound sonicator (U/S) for three minutes. Immediately thereafter it should be put into another volume of fresh SU-8 Developer, again for three minutes in the U/S. Afterwards the developer should be cleaned off with a rinse of IPA and then either methanol or deionized water [64]. The resulting substrate with developed channel in the photoresist is pictured in Figure 4.4.

4.2.8 Electroplating

The gold wire (see Figure 4.5) was formed in the channels in the SU-8 2015, the exposed portions of the seeding layer, by electroplating onto the gold layer. Plating occurred at 60 °C while being stirred at 220 rpm. The 25 μm thick layer of gold took 25 hr to plate with a current density of 275 $\mu\text{A}/\text{cm}^2$ passing through the chip while submerged in a Techni-Gold 25 ES Au solution (Technic Inc., Cranston, RI).

In order to ensure even plating via a constant current density, care must be taken to use a stable current supply. My system uses a custom built supply that follows the circuit diagram shown in Figure 4.6. The output at A_1, given an input V_{in}, is given by

$$V_{out,A_1} = -V_{in}\left(\frac{R_1 + R_2}{R_3 + R_4}\right), \tag{4.2}$$

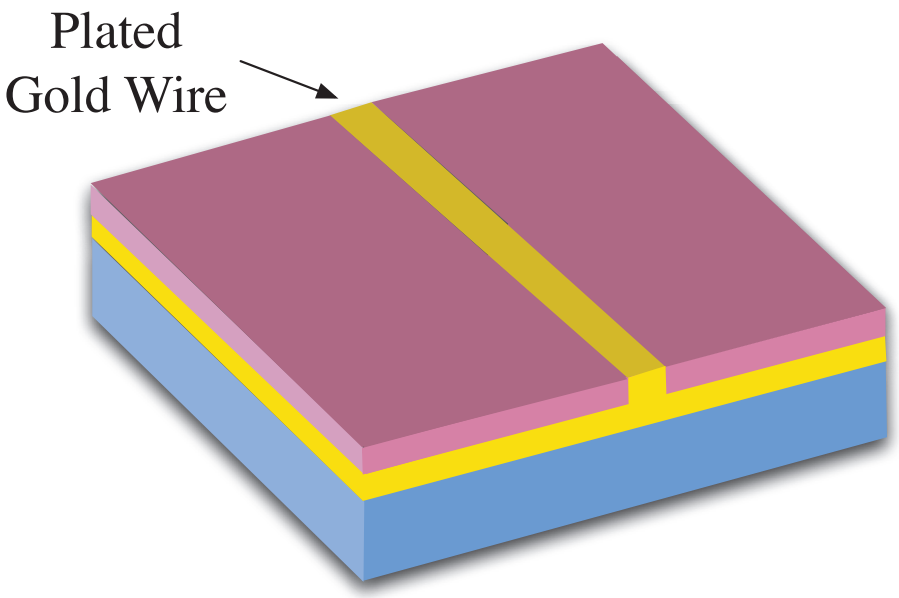

Figure 4.5 : Figure depicting the electroplated gold wire within a photoresist channel. The gold grows on top of the exposed portions of the seed layers, growing at a rate of $1\,{}^{\mu\mathrm{m}}/_{\mathrm{hr}}$.

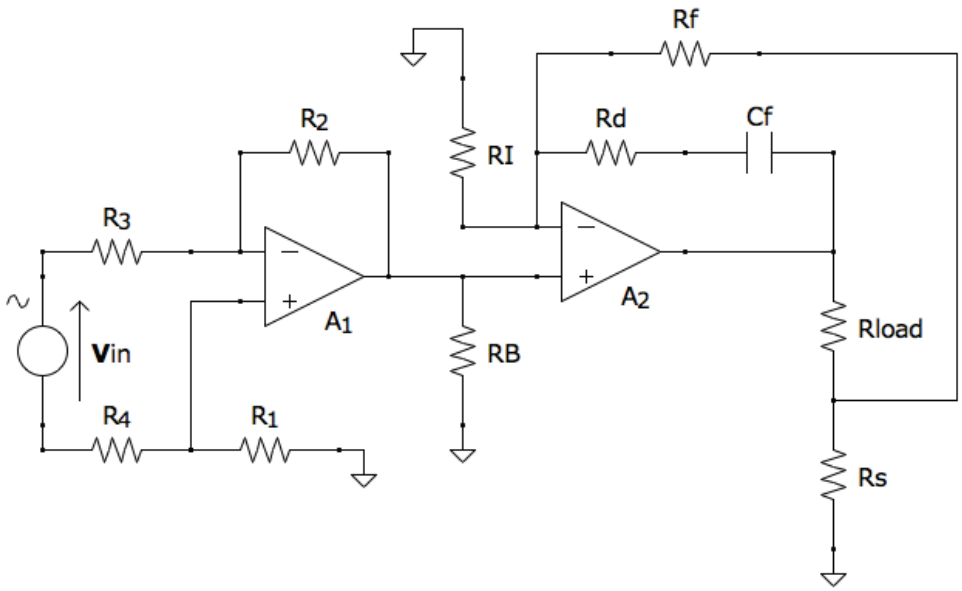

Figure 4.6 : A circuit diagram for an electroplating supply. The input voltage, V_{in}, is decoupled from its external ground by the differential amplifier A_1. The resulting signal is then converted, by amplifier A_2, into a constant current passing through R_{load}. The current is given by $I_{R_{load}} = \frac{V_{out,A_1}}{R_s}\left(1 + \frac{R_f}{R_I}\right)$.

with the output voltage decoupled from any external grounds. With all four resistances in the inverter being the same in this system, $V_{out,A_1} = -V_{in}$. The signal then passes to A_2, which outputs a voltage such that the current flowing through R_{load} is constant and obeys

$$I_{R_{load}} = \frac{V_{out,A_1}}{R_s}\left(1 + \frac{R_f}{R_I}\right), \tag{4.3}$$

when $R_s \ll R_f$ or R_I [68]. Note that Equation 4.3 does not depend upon R_{load}, and so the current supplied through R_{load} is constant. The device thus ensures a constant current density for even plating.

4.2.9 Lift-off and Etch

After electroplating, the resist should be removed, leaving just the wafer and metal. To remove the resist, it must be solubilized, a procedure also known as lifting off. SU-8 2015 may be lifted off if there is a coating of Omnicoat between it and the substrate [64]. A substrate with SU-8 2015 and Omnicoat may be removed by placing it in Remover PG (Microchem) at 80 °C for five minutes. The Remover PG eats away the Omnicoat, leaving beads of SU-8 2015. Cleaning with IPA, DI water, and $N_2\,(g)$ finishes the stripping procedure.

To etch away the gold seed layer, one should expose the seed layer to a GE-8110 $KI_:I_2$ gold etchant (Transene, Inc., Danvers, MA) for 50 sec. Because the seed layer is several orders of magnitude thinner than the electroplated wire, the etchant removes the seed layer while not reducing the gold on the electroplated wires significantly.

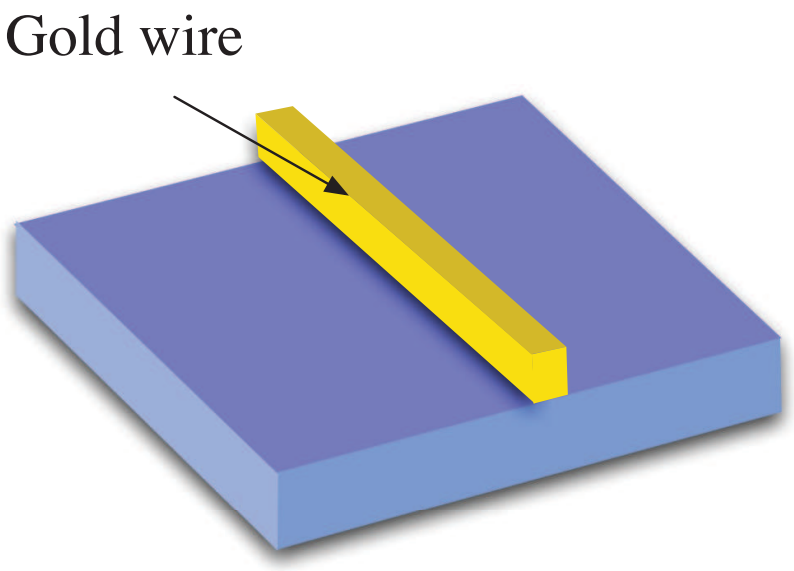

Figure 4.7 : A depiction of the resulting micropatterned wire sitting atop a clean sapphire substrate. In practice, six wires are actually patterned for redundancy.

The thin remaining titanium seed layer may be removed by placing the substrate into a piranha solution for $3 - 5$ sec, or until the gray tinge of the titanium dissolves away. Immediately place the device into a large quantity of DI water to ensure that a minimum amount of titanium between the gold wire and the sapphire substrate is removed. Be sure to do this etching in a functioning fume hood as the fumes that form when the substrate is placed into the water are very acidic. An alternative etch to KI:I_2 is *aqua regia*. *Aqua regia* is a 1:3 ratio of nitric and hydrochloric acids, is extremely aggressive, and able to etch away the entire device in a few minutes. If one must use *aqua regia,* instead of KI:I_2, care should be taken to minimize exposure of the device to as short a time as possible. A diagram of the substrate with only the gold wire remaining can be see in Figure 4.7.

4.3 The MFT Device

Figure 4.8 shows a central portion of a sapphire chip. In the previous section, the fabrication procedure was demonstrated with one wire. In practice, however, the device is made with six gold wires—for redundancy—and electrical leads for application of currents to generate a magnetic field. Up to 6 A has been applied to the device for up to 5 s without destroying the gold wires, but 3 A or less were applied in experiments to avoid excessive heating. The device costs a few hundred dollars to fabricate—with the main cost being that of the gold.

To complete the device, a copper stage holder is also machined to hold the sapphire

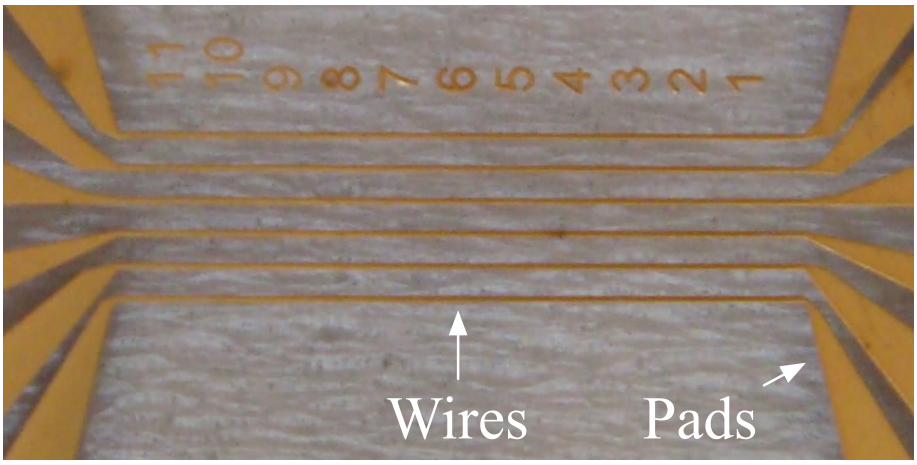

Figure 4.8 : Photograph of the MFT after microfabrication. The six gold wires are 9 mm long with a 425-µm center-center spacing. The pads enable the connection of the microscale wires to macroscale sources.

piece. The stage holder fits snugly into the Zeiss microscope and does not block access to the micropipette. As final component of the device, a PDMS chamber on top of the MFT minimizes fluid evaporation. The PDMS chamber holds in the sample solution through surface tension and has access on one side for the micropipette.

By following the steps detailed above, a magnetic force transducer can be built using standard microfabrication methods. The magnetic force transducer is easily integrated into a microscope as its sapphire substrate is optically transparent and optically polishable. Furthermore, the substrate readily dissipates heat but does not conduct electricity. The electricity, of up to 3 A, may rather be applied through the device, generating localized magnetic fields that can exert force on magnetic beads. If the bead is adhered to a vesicle, a tether may from from the applied point force, which forms the basis of the studies conducted in Chapters 5 and 6.

Chapter 5

A Microfabricated Magnetic Force Transducer-Microaspiration System for Studying Membrane Mechanics

Bring forward what is true. Write it so that it's clear. Defend it to your last breath! - Ludwig Boltzmann [69, p. 198]

The integration of a microfabricated magnetic force transducer and microaspiration, as detailed in this chapter, provides a new tool in a biophysicist's arsenal to investigate membrane properties under a mechanical stimulus. In particular, the combined system exerts a point force, with a controllable waveform, on a membrane while simultaneously holding the tension at a known constant. Such a device may be used to study biologically relevant mechanical properties such as adhesion and mechanotransduction. The following chapter details the development of this technique and its application to the study of tether formation and dynamics.

5.1 Abstract

The application of forces to cell membranes is a powerful method for studying membrane mechanics. To apply controlled dynamic forces on the piconewton scale, we designed and characterized a microfabricated magnetic force transducer (MFT) consisting of current-carrying gold wires patterned on a sapphire substrate. The ex-

perimentally measured forces applied to paramagnetic and ferromagnetic beads as a function of applied current agree well with theoretical models. We used this device to pull tethers from micro-aspirated giant unilamellar vesicles and measure the threshold force for tether formation. In addition, the interlayer drag coefficient of the membrane was determined from the tether-return velocity under magnetic force-free conditions. At high levels of current, vesicles expanded as a result of local temperature changes. A finite element thermal model of the MFT provided absolute temperature calibration, allowing determination of the thermal expansivity coefficient of 1-stearoyl-2-oleoyl-*sn*-glycero-3-phosphocholine vesicles ($1.7 \pm 0.4x10^{-3}\,\mathrm{K}^{-1}$) and characterization of the Joule heating associated with current passing through the device. This effect can be used as a sensitive probe of temperature changes on the microscale. These studies establish the MFT as an effective tool for applying precise forces to membranes at controlled rates and quantitatively studying membrane mechanical and thermomechanical properties.

5.2 Introduction

Mechanical forces regulate a host of biological processes, and the controlled application of forces to membranes and cells is necessary to study mechanosensitive phenomena such as cell adhesion, mechanotransduction, and stem cell differentiation [70]. Several techniques have been developed for applying localized forces to cells, such as atomic force microscopy (AFM), optical tweezers, and magnetic tweezers [71]. While

these techniques have greatly advanced the field of cell and membrane mechanics, they are not without limitations. For example, the applied forces are usually not known *a priori*, and as quantitative biology advances, there is an increasing need for accurate knowledge of both the magnitude and the rate at which forces are applied. Moreover, many force application techniques are limited to cells attached to a microscope coverslip. Optical tweezers generally require a high numerical aperture lens to form the optical trap [72], with lower depth of field that limits working distance [73]. AFM experiments are difficult to perform and interpret on cells that are not supported by a substrate.

For these reasons, it can often be practically difficult to apply piconewton forces while simultaneously manipulating cells with micropipettes, such as during microaspiration and patch clamp experiments. Such integrated experiments are necessary for studies that require simultaneous control of a global parameter such as membrane tension or transmembrane voltage and application of a point force. For example, cell adhesion is mediated by receptor-ligand interactions whose strength is dependent on membrane tension [74] and the rate of force application [75]. Thus, a full biophysical understanding of adhesive interactions requires methods for simultaneous control of membrane tension and application of precise forces.

Early studies in cell adhesion noted that when adherent red blood cells were subject to fluid forces, long, thin tubes of membrane (termed tethers) formed [76]. Later, controlled tether formation became a powerful tool for systematic studies of

cell and membrane mechanical properties [32, 77]. In particular, tether experiments utilizing giant unilamellar vesicles (GUVs) provided a direct method to measure the membrane bending stiffness [12, 78], which regulates processes that involve dramatic changes in membrane curvature such as membrane fusion and microvilli formation. Tether experiments were also developed to measure dynamic membrane properties such as the interlayer drag coefficient opposing relative motion of the membrane leaflets [12, 41]. In these experiments, tethers were formed using gravitational force on glass beads or an additional pipette to retract a tether at a constant rate from an aspirated vesicle. In an alternative approach, magnetic forces have been used to pull tethers. Heinrich and Waugh used a large electromagnet based upon an iron core wrapped with a solenoid in order to pull tethers off aspirated vesicles and measure the membrane bending stiffness [52]. Hosu and Forgacs pulled tethers off adhered cells to study the effect of specific and nonspecific interactions in the tether formation process [56]. While tethers can be successfully pulled with a large iron-core electromagnet, such a device is bulky, produces a force profile that is difficult to model, and has a large inductance that can limit the force modulation bandwidth to the order of 10^2 Hz [11].

To address these limitations, we constructed a magnetic force transducer using microfabrication methods. Microfabricated devices have very low inductances that allow modulation of forces at frequencies several orders of magnitude faster than their larger counterparts [11]. In our design, the device is straightforward to construct with

standard photolithographic techniques, compact, inexpensive and easily integrated into standard microscopes. The force profile is also simple to model. Although microfabricated magnetic force transducers have been described before [10, 11, 59, 61, 79, 80], they have not been integrated with micropipette techniques and used to measure membrane mechanical properties.

Below, we describe the MFT device and present a detailed characterization of its magnetic force and thermal properties. We demonstrate the ability to form tethers from GUVs, and we measure threshold forces and tether dynamics. The thermal properties of the device are used to accurately measure the thermal expansivity coefficient of the membrane. This MFT-aspiration system is easy to operate and broadly applicable to a variety of molecular and cell mechanical experiments, and it is especially attractive as a straightforward method for the controlled application of dynamic forces.

5.3 Materials and Methods

5.3.1 Magnetic Force Transducer Fabrication

Following standard photolithographic techniques [80], we fabricated gold wires atop c-axis cut sapphire (1.5 in × 2 in × 1 mm, Swiss Jewel, Philadelphia, PA, [64]). A full development of fabrication can be found in Chapter 4. Briefly, the sapphire was cleaned in a 10:1 (v/v) H_2SO_4:H_2O_2 piranha etch for 5 min at 100 °C followed by standard organics. Remaining moisture was removed via a 100 °C bake for 30

min. Two seed layers were evaporated onto the substrate using a Sharon E-beam evaporator: 10 nm of 99.99% Ti at a rate of 1 $^{\text{Å}}/_{\text{s}}$, and 100 nm of 99.999% Au (Cerac, Milwaukee, WI) at 2 $^{\text{Å}}/_{\text{s}}$. To form boundaries of the gold wire during electroplating, a 40 μm thick layer of SU-8 2015 photoresist (Microchem, Newton, MA) was spun onto the sapphire substrate under a spreading cycle of 500 rpm for 5 s and a spinning cycle of 1600 rpm for 30 s. A thin layer of Omnicoat (Microchem) was used to improve adhesion between the gold seed layer and SU-8 2015. This was followed by a soft-bake of 65 °C for two min and 95 °C for 5 min. After baking, the resist was exposed to 365 nm UV light at an exposure dose of 250 $^{\text{mJ}}/_{\text{cm}^2}$ using an MJB4 Mask Aligner (Süss MicroTec, Philadelphia, PA) and a patterned chrome mask (designed in house, made by Fineline Imaging, Colorado Springs, CO). A post-exposure bake at 65 °C for 2 min and at 95 °C for 1 min followed. The guide channels were finally formed upon development of the photoresist with two 3 min exposures to SU-8 developer in an ultrasound sonicator.

A 25 μm thick layer of gold was plated onto the exposed portions of the seeding layer over 25 hr. The layer was formed with a current density of 0.275 $^{\text{mA}}/_{\text{cm}^2}$ passing through the chip while submerged in a Techni-Gold 25 ES Au solution (Technic Inc., Cranston, RI) at 60 °C while being stirred at 220 rpm. The SU-8 2015 and Omnicoat were then removed with Remover PG (Microchem) at 80 °C for 5 min. Exposure to a GE-8110 KI:I_2 gold etchant (Transene, Inc., Danvers, MA) for 50 sec etched the seed layer while not significantly reducing the gold on the electroplated wires.

Using a profiler (Dektak 6M, Veeco, Plainview, NY), we determined the wires were 90 μm wide and 25 μm tall. As shown before, Figure 4.8 shows a central portion of a sapphire chip with six gold wires—for redundancy—and leads for application of currents to generate a magnetic field. Up to 6 A could be applied to the device for up to 5 s without destroying the gold wires, but 3 A or less were generally applied in experiments to avoid excessive heating.

The device cost a few hundred dollars to fabricate—with the main cost being that of the gold. In addition to a low cost compared to many other force application systems, MFT devices of various patterns are possible, limited to the geometry and resolution of the chrome mask. Furthermore, a new device may be fabricated within two days. As such, it is quick and inexpensive to modify the system. To fit the sapphire piece, a copper stage holder was also machined to hold the sapphire piece. The stage holder fitted snugly into the Zeiss microscope and did not block access to the micropipette. A polydimethylsiloxane (PDMS, Dow Corning) chamber was placed over the device to minimize fluid evaporation. It held in the sample solution through surface tension and had access on one side for the micropipette.

5.3.2 Vesicle Formation

The majority of vesicles were formed using the electroformation technique described by Zhou and Raphael [31, 33]. A detailed protocol may be found in Appendix A. A 15 μL chloroform solution containing 1 $^{\text{mg}}/_{\text{mL}}$ 1-stearoyl-2-oleoyl-*sn*-glycero-3-phos-

phatidylcholine (SOPC) or, in the case of tether experiments, 1-palmitoyl-2-oleoyl-*sn*-glycero-3-phosphocholine (POPC, both from Avanti Polar Lipids, Alabaster, AL), which had been stored at −20 °C under nitrogen, was spread on each of two platinum electrodes and placed under vacuum for at least 2 hr. The electrodes were then submerged in 200 mM sucrose solution (Sigma-Aldrich, St. Louis, MO) and exposed to an alternating voltage. The voltage consisted of the waveforms: 10 Hz at 250 mV to 1000 mV in 250 mV increments, at 10 min each; then 6.6 Hz at 750 V and 3.3 Hz at 500 mV, at 10 min each; finally 1.1 Hz at 250 mV for 90 min. The vesicles were then collected and stored under nitrogen in a 4 °C refrigerator. For tether experiments, either 0.5 mol % or 5 mol % Biotin-X-DHPE (*N*-((6-(biotinoyl)amino)-hexanoyl)-1,2-dihexadecanoyl*sn*-glycero-3-phosphoethanolamine, triethylammonium salt, Invitrogen, Carlsbad, CA) was added to the SOPC solution.

5.3.3 Magnetic Bead Composition

Paramagnetic beads (Spherotech, Lake Forest, IL) at 2.5% $^{w}/_{v}$ were stored in 0.016 M phosphate buffered saline (PBS), pH 7.4 with 0.02% sodium azide. These 2.2 μm diameter beads further consisted of a 12% $^{v}/_{v}$ $\gamma - Fe_2O_3$ nanoparticle-polystyrene blend. Streptavidin-coated ferromagnetic beads (Spherotech) at 1% $^{w}/_{v}$ were also contained in 0.016 M PBS, pH 7.4 with 0.02% sodium azide, and the 4.4 μm diameter microspheres consisted of an 8% $^{v}/_{v}$ CrO_2 nanoparticle-polystyrene blend. The beads were then diluted ten times, thoroughly mixed, and refrigerated. For force calibration ex-

periments, a 2 μL stock bead solution was further diluted in 998 μL Milli-Q deionized water. For tether experiments, the 2 μL stock bead solution was mixed in a solution composed of 998 μL 210 mM glucose (Sigma-Aldrich) and 12.5 μL 10x PBS. Immediately before experiments, the ferromagnetic beads were exposed to a 300 mT field for at least 5 sec to align the magnetic micro-domains within the beads. Only 200 mT is needed to ensure maximum remanent magnetization [81].

5.3.4 Vesicle Aspiration

Aspiration pipettes were fabricated using a P-97 micropipette puller (Sutter Instrument, Novato, CA) on borosilicate capillary tubes (Kimble Chase, Vineland, NJ) and cut cleanly on a custom-built micro-forge. A 1% (BSA, Sigma) solution in 210 mM glucose was used to coat the pipettes, which were subsequently washed in a pure glucose solution. During experiments, pressure was maintained by attaching the micropipette to a water reservoir with 10 μm mm resolution (Robo Cylinder, IAI, Torrance, CA) and the height of the water reservoir corresponding to a neutral pressure at the pipette tip was periodically calibrated using vesicle debris or magnetic beads, both of which experienced neutral pressures at the same water reservoir height. Pressures from 4.9 Pa to 49 Pa were then used to aspirate the vesicle within the pipette.

5.3.5 Force Calibration of MFT

Force calibration of the MFT was conducted on an Axiovert 200M inverted microscope on a 20x Ph1 LD A-Plan (Zeiss, Thornwood, New York) with a 1.6x optovar. After

(a)

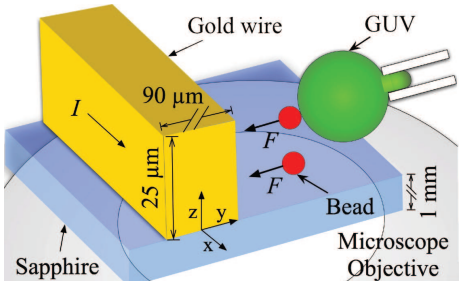

(b)

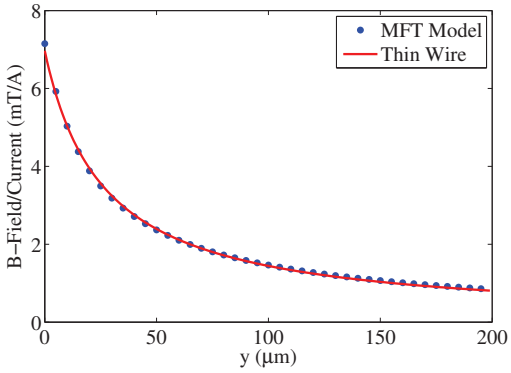

Figure 5.1 : Schematics of the MFT with an aspirated GUV and associated model of the magnetic field. (a) An electroplated rectangular gold wire sits atop an optical quality sapphire substrate above the microscope objective. Current (I) in the wire generates a magnetic field that exerts force upon the ferromagnetic bead adhered to the GUV, which can pull a tether. Free-floating beads were used to calibrate forces. (b) Calculated magnetic field versus distance from the wire edge at half the height of the wire. Even though the wire is rectangular, the field (blue dots) matches well the r^{-1} curve (red line) expected for an infinitely thin wire.

beads were added, and if necessary, magnetized, a 1 s current pulse of 0.5 A to 3 A was sent through a single wire on the MFT via a custom-built computer interface. These high currents generated a magnetic field that decreased with distance from the wire. Any magnetic microbeads in the system experienced a force of attraction and were accelerated towards the wire. Figure 5.1a depicts a cartoon of the device.

Images were taken with a Retiga 2000R (Qimaging, Surrey, BC) at 4x4 binning and with external triggering via Labview 2009 (National Instruments, Austin, TX) to obtain frame rates of up to $\sim$ 50 fps. Images were subsequently analyzed with custom tracking programs in MatLab 2009b (The Mathworks, Natick, MA) to obtain particles trajectories and velocities.

The expected force profile is easily calculated from the known cross-sectional geometry of the wire, treating it as an infinitely long rectangular wire with uniform current density. We integrated the field, $\mathbf{B}$, generated by the current, I, as:

$$\mathbf{B}(\mathbf{r}) = \frac{\mu_0 I}{2\pi A} \iint_A \frac{1}{|\mathbf{r} - \mathbf{r_0}|} \hat{\phi}\, dA, \tag{5.1}$$

where μ_0 is the permeability of free space, A is the cross-sectional area of the wire normal to the current flow, $\mathbf{r}$ is the position of the bead, and $\mathbf{r}_0$ is the location of infinitesimal element of the cross-sectional area. The integral extends over the wire cross section lying in a plane perpendicular to the wire and containing the location of the bead. Figure 5.1b shows the result of this calculation along the $+\hat{y}$ direction at the wire's mid-height. The field is fit well by the equivalent expression for an

infinitely thin wire:

$$\mathbf{B} = \frac{\mu_0 I}{2\pi y}\hat{y}, \tag{5.2}$$

where y is the distance from the center of the wire. We used this expression for the field in all force calibration measurements.

5.3.6 Thermal Characterization of the MFT

5.3.6.1 Finite Element Modeling

The temperature profile within the device was modeled using the Transient Heat Transfer Conduction package on COMSOL 3.4. Details of the modeling may be found in Appendix B. All components of the MFT system were included in the model: the sapphire, gold wires, surrounding air, and PDMS and glass coverslip chamber filled with water. The model used time step sizes of no more than 0.01 s and contained over 140,000 mesh points. The model's outer boundaries were modeled with large enough spatial dimensions as to not affect the model's convergence; increasing the dimensions of the model's outer boundaries had negligible effect on the temperature profile. These outer boundaries were set so that they were closer to the wire than the boundaries in the real system. Additionally, each outer boundary's temperature was held at 293.15 K, and at all interior boundaries, the temperature was continuous. The heat source for the model was determined experimentally by measuring the voltage drop across the wire between the pads for each applied current and assuming that the dissipated power (IV) was deposited uniformly in the wire. The heat source in

the model was only present during the first 6 s of the simulation, while the simulation itself lasted up to 16 s, which matched experimental conditions. Swiss Jewel provided the thermal conductivity (32.5 $^{W}/_{m\cdot K}$), density (3970 $^{kg}/_{m^3}$), and heat capacity of sapphire (669.44 $^{J}/_{kg\cdot K}$), and the parameters of PDMS were taken from the Polymer Data Handbook [82]. All other material parameters were from the COMSOL materials database.

5.3.6.2 Membrane Thermoelasticity

The area of the GUV membrane and the length of projection into the pipette are sensitive to the temperature of the local environment. Determination of projection lengths into the pipette of an aspirated vesicle was performed with a 40x DIC W Plan-Apochromat (Zeiss) with a 1.6x optovar at 1x1 binning and frame rates of ~ 28 fps. The projection length changed with current due to temperature rise of the membrane. The strain resulting from this temperature rise, α, was determined using

$$\alpha = \frac{2R_P\Delta L\,(1 - {}^{R_P}/_{R_V})}{4R_V^2 - R_P^2 + 2R_P L_0}, \tag{5.3}$$

where R_P is the pipette radius, R_V is the vesicle radius, ΔL is the change in projection length, and L_0 is the initial projection length [33, 83]. Using the COMSOL model of the temperature rise of the MFT during current pulses lasting 6 s of 1, 2, or 3 A, a thermal area expansivity of the membrane was extracted from the observed strain.

5.3.7 Tether Studies

Tether studies consisted of first aspirating vesicles as described above (see Figure 5.1a). The vesicle was then slowly moved to a free-floating bead and tapped against it until the streptavidin-coated bead adhered to the biotinylated Biotin-X lipids within the GUV. The GUV-bead complex was then gently moved to within 100 μm of the MFT. A ramp waveform (1, 2, or 3 A for 3 or 6 s) was applied, and the resulting images were analyzed to obtain tether extension curves.

5.4 Results and Discussion

5.4.1 Force Calibration

In order to verify our field profile and calibrate the force on the beads, we tracked the response of both paramagnetic and ferromagnetic microspheres, not attached to vesicles, as current was passed through the magnetic force transducer. The beads were in the low Reynolds number regime, so the velocities of the tracked particles were converted into forces using Stokes Law:

$$\mathbf{F}_{Stokes} = -6\pi\eta R\mathbf{v}, \tag{5.4}$$

where $\mathbf{F}_{Stokes}$ is the Stokes force, η the viscosity of water (0.89 mPa $\cdot$ s), R the radius of the bead, and $\mathbf{v}$ the velocity. The Stokes force balanced the applied magnetic force $\mathbf{F}_{Stokes} = -\mathbf{F}_{mag}$. For a magnetic bead, the force due to an applied magnetic field is

given as

$$\mathbf{F}_{mag} = \nabla \left(\mathbf{m} \cdot \mathbf{B} \right), \tag{5.5}$$

where $\mathbf{m}$ is the magnetic moment of the bead. For a paramagnetic bead with a magnetic susceptibility χ_{bead} and radius R [61], Equation 5.5 reduces to

$$\mathbf{F}_{para} = -\frac{\mu_0 \chi_{bead} R^3}{3\pi} \frac{I^2}{y^3} \hat{y}. \tag{5.6}$$

As can be seen in Figure 5.2a, the force on free-floating paramagnetic beads follow a y^{-3} master curve over a current range from 0.75 A to 3 A when normalized by the current squared. The maximum force seen for paramagnetic beads in this study was 5.4 pN. Taking the parameters of the fit curve and a bead radius of 1.1 μm, we found a χ_{bead} of 0.14. This value compares well to the susceptibility of 0.17 reported by Shevkoplyas *et al.* for superparamagnetic microbeads composed of iron oxide in a polymer matrix when applying Equation 5.6 [61]. The discrepancy between the values may be due to slightly different filling fractions between bead types, leading to different force strengths for similarly sized beads. Similarly, given the strong dependence on the radius, slight difference in bead size will yield different estimates in the susceptibility.

Applying Equation 5.5 to a free-floating ferromagnetic bead, the force experienced is

$$\mathbf{F}_{ferro} = -\frac{\mu_0 m}{2\pi} \frac{I}{y^2} \hat{y}. \tag{5.7}$$

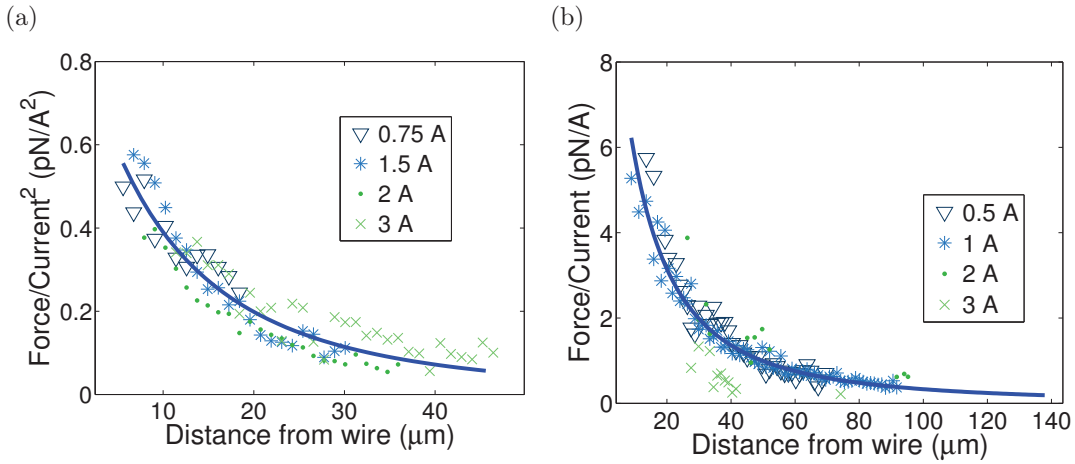

Figure 5.2 : Normalized magnetic forces generated by the MFT and measured using magnetic beads. (a) The normalized force experienced by free-floating paramagnetic beads for several different currents scales as the square of the current and varies with distance from the wire (y) as $\nabla\left(B^2\right) \propto y^{-3}$ (solid blue line), as expected for paramagnetic material. Each current is the binned average of several runs with a bin of $1\,\mu$m. (b) The force for free-floating ferromagnetic beads scales with the current and varies as $\nabla B \propto y^{-2}$ (solid blue line). Each current is the binned average of several runs with a bin of $1\,\mu$m.

Figure 5.2b shows the force profiles of ferromagnetic beads normalized to I when exposed to fields generated by currents ranging from 0.5 A to 3 A. The maximum force seen for ferromagnetic beads was $\sim$ 20 pN, which is comparable to the forces applied using an iron-core-based electromagnet [52]. The low forces recorded for 3 A might have been due to non-negligible convective effects at higher current. Calibration at 3 A is also difficult due to high bead velocity. Other than at 3 A, these profiles fit a y^{-2} curve well, and yield a magnetic moment of $4x10^{-14}\,\mathrm{A}\cdot\mathrm{m}^2$. While the magnetic moment depends upon volume fraction and magnetization of the magnetic material, our measured value agrees reasonably well with a previously reported value of $3x10^{-13}\,\mathrm{A}\cdot\mathrm{m}^2$ extrapolated from SQUID magnetometer results for similar beads [81]. Ferromagnetic beads were used for the biophysical studies in this work because larger applied forces were possible and the force profile did not decrease with distance as quickly as compared to paramagnetic beads. While paramagnetic beads had some practical advantages, including not requiring magnetization before use and of having magnetic moments that modulated linearly with external field in the field strengths of interest, the lower applied forces limited the use of paramagnetic beads for membrane tether studies. However, the calibration data on paramagnetic beads substantiates the quantitative calculation of forces in the device because different spatial dependence of the force provided an independent check of the expected magnetic field profile.

While forces of $\sim$ 20 pN observed with ferromagnetic beads are not as high as those achievable with optical tweezers or macroscopic magnetic transducers, they

are large enough to conduct mechanical studies on vesicles or cell membrane blebs. Higher forces further from the wire would enable the study of longer tether lengths ($> 100\,\mu$m) and measurement of the nonlocal bending energy of the membrane [12, 41] and investigation of the electromechanical properties of membranes under high curvature [84]. In principle, the forces may be increased by using beads of higher magnetic content or by increasing the current that the device can carry. Although thermal concerns limit the electrical current in the MFT described herein, the MFT design can be modified to roughly double the current limit based on our understanding of the thermal response of the device, which is described below. While it may be possible to increase the forces with optimization of bead properties, we have focused on our ability to apply controllable and calibrated forces rather than on investigating the magnetic properties of the beads.

5.4.2 Membrane Thermoelasticity

As in several other force application techniques, such as optical tweezers [85–88] and some magnetic designs [10], the MFT described here can cause localized heating of the solution bathing the membrane system. In this case, it is due to current flow producing Joule heat, which raised the temperature of the water near the wire and the vesicle. This temperature rise caused the membrane area to expand, which manifested itself as a visible increase in the projection length. In order to study this phenomenon carefully, we applied a 6 s constant current pulse through the MFT at

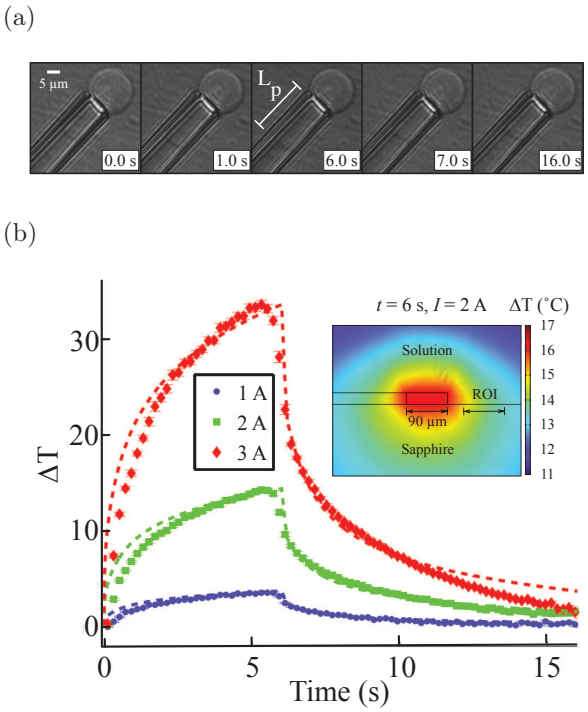

Figure 5.3 : Thermomechanical responses of aspirated vesicles in reaction to a 6 s pulse at 1, 2, or 3 A. (a) A time sequence showing the increase in L_p as current is applied. Once the current stops flowing, the projection length quickly returns to its original value. (b) The temperature estimate of the magnetic force transducer using a COMSOL model (dashed lines) shows an I^2 dependence with maximum temperature changes of 33 °C at 3 A. Estimating the thermal area expansivity at $1.7x10^{-3}\,\mathrm{K}^{-1}$, the areal strain change of the vesicle with applied current may be converted into temperature changes (error bar plots of mean temperature with standard error with symbols serving as error bars if error bars are not displayed) for 1 A ($N = 35$), 2 A ($N = 35$), and 3 A ($N = 30$). The variation of temperature with position predicted by the COMSOL model may be seen in the inset with the solution of the model at $t = 6$ s with $I = 2$ A. The region of interest (ROI) depicts the range of positions of the GUVs during this study.

various current levels (1 A, 2 A, and 3 A). At the onset of current application, the projection length increased rapidly for the first few hundred milliseconds, and then grew more gradually, as can be seen in Figure 5.3a. When the current halted, the projection length returned to its initial extension with a similar temporal pattern.

In order to understand the response of the vesicle, the temperature of the system was modeled using COMSOL 3.4, as detailed in Section 5.3.6.1. The result of this model may be seen as the dashed lines in Figure 5.3b. The temperature rise followed the I^2 dependence expected for Joule heating, with a maximum temperature rise of 30 °C after 6 s with $I = 3$ A. At 2 A after 3 s, the maximum current at which the majority of experiments were conducted and the length of time for which most experiments took place, the temperature rise was ~ 10 °C, which resulted in nearly physiological temperatures and was only a factor of two greater than the heating reported in optical tweezers [85, 87]. Using larger wires, the Joule heating could be further reduced. The temperature rise was described by a double exponential with a fast time constant of 0.3 s and slow time constant of 3 s. Likewise, cooling followed a double exponential with time constants of 0.4 s and 4 s. The fast time constant related to the immediate warming of the solution and sapphire; the slow time constant corresponded to the gradual increase in the background temperature as the entire sapphire chip heated. The inset shows the position dependence of temperature and one can see that the temperature was relatively uniform in the region of interest (ROI) for our experiments (between 25 μm and 100 μm), with a variation of less than

2 °C for 2 A. This uniformity is chiefly due to the high thermal conductivity of the sapphire substrate.

The ratio of area change to temperature change is the thermal area expansivity modulus (α_T) of the membrane. Using α_T as a free parameter, we were able to match all the measurements of the areal strain in the vesicle to COMSOL temperature predictions (error bar plots in Figure 5.3b). This fit yields a thermal area expansivity modulus of SOPC GUVs of $1.7 \pm 0.4x10^{-3}\,\mathrm{K}^{-1}$. To our knowledge, this is the first determination of the area expansivity of SOPC, but the obtained value is reasonable as it falls between the values of $2.4 \pm 0.4x10^{-3}\,\mathrm{K}^{-1}$ measured in egg lecithin [83] and $1.2 \pm 0.4x10^{-3}\,\mathrm{K}^{-1}$ reported for red blood cells [29]. Given that the elastic modulus of egg lecithin (0.14 N/m, [83]) is less than that of SOPC (0.211 N/m, [31]), which in turn is less than that of red blood cells (0.45 N/m, [29]), the thermal area expansivity of SOPC is expected to lie between that of egg lecithin and red blood cells. Thus, using knowledge of the temperature change from the COMSOL model, the MFT can be used to determine α_T for aspirated membrane systems, or conversely, an aspirated vesicle can be used to determine the local temperature increase at microscale length scales if the expansivity of the vesicle is known.

The uncertainty in our measurement of α_T was dominated by systematic uncertainty in the results of the COMSOL model. The major contributions to uncertainty in the predicted temperature change were uncertainty in sapphire conductivity, and variation in the applied power, which changed slightly because the resistivity of the

wire increased as the temperature rose. By running simulations at the extremes of these parameters, we estimated a relative error of 20% as the uncertainty in the expansivity model.

5.4.3 Membrane Tether Formation and Dynamics

In order to demonstrate the ability of the MFT to study membrane mechanics, we conducted tether formation experiments by attaching ferromagnetic beads to micro-aspirated GUVs and tracking their position while applying a linear current ramp to the MFT. Once the magnetic force reached sufficient strength, a tether formed, as seen in Figure 5.4a for a representative tether, and continued to lengthen until the current stopped. At that time, the tether retracted, drawing the bead back to its original position. The length of the tether, L_t (Figure 5.4b) was time dependent.

This trajectory may be seen in Figure 5.4c. The force on the bead increased linearly with current while the bead was stationary, but when the force reached 2.4 pN, a tether formed. The bead then moved toward the wire, which also caused an increase in the force ramp experienced by the bead. At 3.2 s, the current stopped. Such trajectories are a powerful tool for studying membrane properties, including determining the force at which tether formation occurs. We found that the force threshold, F_{th}, depended upon the concentration of biotin-X in the vesicle. At 0.5 mol % biotin-X, 2.1 ± 0.3 pN was required to pull a tether; while at 5 mol % biotin-X, 18.8 ± 5.4 pN was necessary. The adhesion strength depends upon membrane tension, the contact

(a)

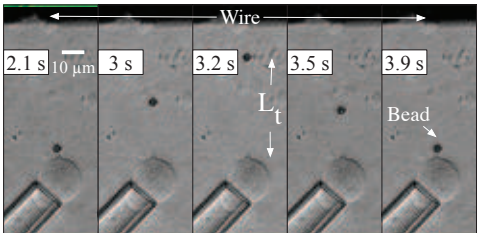

(b)

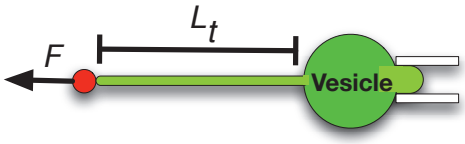

(c)

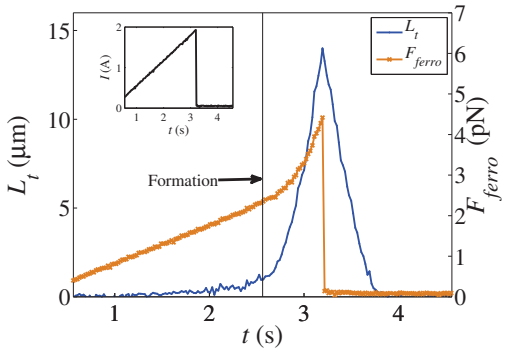

Figure 5.4 : Demonstration of a tether pulled from an aspirated GUV with the MFT. (a) The time sequence displays a ferromagnetic bead being pulled from a vesicle upon application of current through the wire. Once current flow was halted, the tether dragged the bead back to its initial position against the vesicle. (b) A cartoon of the aspirated vesicle depicting the tether length, L_t, from the edge of the ferromagnetic bead to the vesicle surface. (c) L_t (blue line) and pulling force F_{ferro} (brown line) during the linear ramp (see inset). A tether ($L_t \sim 0$) formed when the force experienced by the ferromagnetic bead (brown line) was sufficiently high. Once a tether formed, the force no longer followed a linear ramp since the distance to the wire was simultaneously decreasing. The force and force ramp increased until the current, and hence force, was turned off. The tether then retracted to its initial position only under the influence of membrane forces and viscous drag from the medium.

area and the concentration of receptors and ligands [74]. As the membrane tension was held approximately constant in our experiments, the greater required threshold force for higher biotin concentration likely reflects a greater contact area mediated by more adhesion sites between the streptavidin-coated ferromagnetic microbead and the biotinylated lipids, similar to previous observations in which the contact area was directly modulated [89].

Furthermore, with the ability to control piconewton forces dynamically, the effect of the force ramp $^{df}/_{dt}$ on tether formation can be investigated, which has not been carefully probed experimentally to the best of our knowledge. Control of $^{df}/_{dt}$ is essential for understanding interactions mediated by specific receptor-ligand interactions, where the disassociation rate depends heavily on the rate of force application and molecular details of the bond [75, 90, 91]. In this work, we observed tether formation at rates of $7.6 \pm 1.9\,^{\mathrm{pN}}/_{\mathrm{s}}$ for 5 mol % biotinylated lipids and of $1.59 \pm 0.25\,^{\mathrm{pN}}/_{\mathrm{s}}$ for 0.5 mol % biotinylated lipids. However, our MFT is capable of controlling force rates up to the order of $1x10^{4\,\mathrm{pN}}/_{\mathrm{s}}$ (see Section 6.4.1) and so could be used for dynamic force spectroscopy of receptor-ligand interactions [91] by tailoring membrane and bead composition appropriately [75].

Returning to Figure 5.4c, the viscous force during tether return was driven by membrane tension and retarded by viscous drag. During the return, the bead experienced no magnetic fields. The return itself was fairly constant as evidenced by the linear trajectory during this phase. In equilibrium tether systems, this force, F_{return},

is simply related to the bending stiffness and membrane tension by

$$F_{return} = 2\pi\sqrt{2k_c\tau}, \tag{5.8}$$

where τ is the tension and k_c is the bending modulus [12, 92]. However, in dynamic systems, Evans and Yeung found that viscous dissipation between the membrane leaflets is significant [41]. Following previous developments [12, 41], the interlayer drag coefficient, b, can be calculated using the return force by

$$F_{return} = 2\pi\sqrt{2k_c\tau} + 2\pi\frac{dL_t}{dt}h^2\ln\left({}^{R_V}/_{R_t}\right), \tag{5.9}$$

where h is the membrane thickness, R_V is the vesicle radius, and R_t is the tether radius. The second term on the right, the viscous term, may contribute up to the same order of magnitude as the first term, the tension term, to the total force [12, 41], and so cannot be neglected. Using $k_c = 1.2x10^{-19}$ J [12] and $R_t = 20$ nm we obtained a value of $b = 1.1\pm0.55x10^{9}$ ${}^{\text{N·s}}/_{\text{m}^3}$. (Note that although R_t was not measured independently, the calculated value of b only depends weakly on R_t). This is comparable to a value of $b = 4.6x10^{8}$ ${}^{\text{N·s}}/_{\text{m}^3}$ measured by Raphael and Waugh [12] and the 10^8 magnitude estimate of Evans and Yeung for PC systems [92]. The interlayer membrane viscosity may be sensitive to the rate at which the tether flows, which can also be probed using the MFT.

5.5 Summary

We have developed a microfabricated magnetic force transducer (MFT) that can be combined with microaspiration in order to study membrane mechanical properties via the application of point forces to the membrane. In this design, the transducer's magnetic field is straightforwardly modeled, and its field strength is adjusted by controlling the current passing through the wire. The ability to precisely control the current enables application of force rates from 1 to $10^{4\,\mathrm{pN}/\mathrm{s}}$ and application of various waveforms, including force ramps, pulses and sinusoids. The range of force profiles achievable in the MFT is difficult to reproduce in other force application systems.

To demonstrate the utility of the MFT, several biophysical properties of giant unilamellar vesicles were measured: the thermal expansivity coefficient α_T, the threshold force for tether formation F_{th}, and the interlayer drag coefficient b. For SOPC vesicles, we found $\alpha_T = 1.7 \pm 0.4x10^{-3}\,\mathrm{K}^{-1}$ in the temperature range of 22 to 50 °C, $F_{th} = 2.1 \pm 0.3$ to $18.8 \pm 5.4\,\mathrm{pN}$, depending on the concentration of biotin in the vesicle, and $b = 1.1 \pm 0.6x10^{9\,\mathrm{N}\cdot\mathrm{s}/\mathrm{m}^3}$. All these properties are consistent with previous measurements, establishing the MFT-microaspirator as a powerful tool for studying membrane mechanical properties. For example, the MFT can be used to quantitatively determine how changes in the chemical composition of the membrane by biologically important molecules—such as cholesterol, salicylate, or alcohols—alter the dynamic properties of membranes. In addition, different receptor-ligand pairs can be studied, and the MFT can be used to determine the relationship between den-

sity of adhesion sites and force thresholds and to investigate the relationship between dynamic force application and adhesion strength.

Chapter 6

The Use of a Micromagnetic Tweezer to Study the Dynamics of Tether Formation

Truth in science can be defined as the working hypothesis best suited to open the way to the next better one. - Konrad Lorenz [93]

WHILE there are several possible applications of the magnetic force transducer-aspiration system, such as measuring the thermal expansion coefficient or interlayer drag coefficient of various membrane compositions, we have applied our newly developed system to study the dynamics of tether formation in a vesicle and how this formation depends on applied force ramp. A strong dependence was found between these two observables. To ensure there were no other dependencies, the variation of the observed force threshold and the force ramp were compared to position, temperature, current threshold and time until tether formation. To interpret the results, we propose an energy model consisting of two barriers and use it to begin mapping the energy landscape of tether formation.

6.1 Abstract

Tethers are important in many cellular functions from morphological changes to material transfer. Much work has gone into studying the mechanics of tethers and tether formation, with particular focus on the role of the receptor-ligand bond. In many bi-

ological systems, such as white blood cell adhesion, tethers form not under a constant applied force but rather under a dynamically changing force. To date, no studies have investigated the relationship between the force necessary to form a tether and the rate at which the force changes. In order to determine this interdependence, we have applied our previously developed microfabricated magnetic force transducer-aspirator system to investigate the strong relationship the threshold force of tether formation had on force ramps that spanned three orders of magnitude. Other possible dependencies based on position, threshold current, temperature, and threshold time were investigated but found not to affect the measured relationship between threshold force and force ramp. We found the relation between these quantities to be well described by a two-barrier energetic model reminiscent of a model used for membrane lysis under dynamically changing tensions. Such studies form a basis from which the energy landscape of tether formation can be examined, including in model membranes containing cholesterol or in more complicated cellular systems.

6.2 Introduction

When a point force is applied to a membrane, a long and thin protrusion from the membrane with significantly higher curvature may form. This protrusion, also known as a tether, has been extensively studied for its biological importance in immune response [4, 5, 8] and cellular trafficking [6, 7]. Tether studies have involved understanding the effect of temperature induced membrane undulation on tether mechanics

along with the competition of steric and van de Waals energies [27]. Research has also been conducted on how curvature affects protein diffusion in membranes [94], and on the effect of amphiphiles on such membrane properties as bending modulus and thermal expansion coefficients [31, 95]. The mechanics governing tethers has also been reviewed quite extensively, with Seifert's review being particularly detailed [96, 97].

Most of the previous work though focused on static tethers and ignored how the tether was actually formed. Examination of the dynamics of tethers gained traction with the development of a model including the interlayer drag between leaflets [41] and demonstration of its non-negligible contribution to relevant energetics [12, 41]. Maeda *et al.* studied tether formation by investigating the forces seen as an AFM tip with multiple monolayers was pressed against and slowly pulled away from a surface covered with monolayers. They found discrete forces for DPPC layers (and broader ones for DMPC layers) corresponding to tether formation with AFM speeds of between $0.5\,{}^{\mu\mathrm{m}}/_{\mathrm{s}}$ and $50\,{}^{\mu\mathrm{m}}/_{\mathrm{s}}$ [98]. A more recent experiment used microaspiration to examine the force threshold required to pull tethers from human umbilical vein endothelial cells at various velocities and found a phenomenologically determined power law to relate the dependencies [13]. Theoretically, initial models of tether formation derived from soap film theory, with tether formation being modeled as two concentric rings being separated. Two regimes were shown in this model: a tension regime at high tether radii, and a bending regime at low tether radii [99]. A similar develop-

ment using the general shape equation with a surface parameterized by the angle of the tether showed that multiple tethers would coalesce during formation into one without an external agent (such as cytoskeletal linkage) separating them [100]. The force ranges at which tethers would form from vesicles adhered to a surface were developed using thermodynamic considerations and found to depend upon the energy and volume associated with adhesion [101]. Very recently, Pospieszalska *et al.* formulated a rigorous viscoelastic model explaining when a protrusion (viscoelastic under low forces) from a cell changes into a tether (large forces with growth proportional to force) [102].

As the physics underlying tether growth has been extensively studied, the understanding of specific adhesions—one method to exert force to develop a tether—has also been developed. Merkel *et al.* first examined adhesive dynamics using a technique they developed called dynamic force spectroscopy and used it to investigate the force required to break a streptavidin or avidin bond with biotin [75]. Recently, theoretical frameworks for adhesion have been discussed using thermodynamic considerations (to model de-adhesion of vesicles to study binding in cells) [74] or energetic considerations (to model how bond strength depends upon force ramp) [91].

With all these studies into tether dynamics, formation, and adhesion, none have yet, to the best of our knowledge, examined experimentally how the time rate of change in the applied force affects the force at which tethers form. To investigate this dependence, we utilized the combined magnetic force transducer (MFT)-

microaspirator that we have previously developed in Chapter 5. This device generated localized, well-controlled magnetic fields that generated forces on magnetic beads. The beads were adhered to a microaspirated vesicle through biotin-streptavidin bonds. With a sufficiently large force, a tether would form and the subsequent trajectory of the bead—as a proxy for the tether location—measured. The resulting trajectory and recorded current information allowed the applied force and force ramp to be determined.

This chapter begins by briefly reviewing the MFT-microaspirator system presented in Chapter 5. The relation between the threshold force of tether formation and the temporal change in the applied force will be presented, followed by several studies to examine any other correlations. Two models will be presented to describe the observed behavior: a one-barrier energy model and a two-barrier energy model. Using the more appropriate model, a first attempt at determining the energy landscape of tether formation will be presented.

6.3 Materials and Methods

To study how the threshold force of tether formation depends on the rate at which that force was applied, we made use of the joint magnetic force transducer-aspirator that was developed in Chapter 5. The MFT consisted of a sapphire substrate with gold wires patterned atop. The aspirator consisted of micro-forged pipettes. The vesicles used in the study were electroformed using lipids. Below, we give more detail

into the materials used for the experiments and the methods by which the experiments were conducted.

6.3.1 Magnetic Force Transducer Fabrication

We fabricated gold wires atop sapphire (1.5 in × 2 in × 1 mm, Swiss Jewel, Philadelphia, PA, [64]) following standard microfabrication methods (see Section 5.3.1). A 10 nm 99.99% Ti layer was evaporated unto a clean sapphire substrate using a Sharon E-beam evaporator. Evaporating 100 nm of 99.999% Au onto the Ti formed a seed layer for later electroplating. Electroplating required a barrier to direct where the structure would form. A 40 μm thick, patterned photoresist layer made of SU-8 2015 photoresist (Microchem, Newton, MA) provided the shape for wire growth after exposure through a chrome mask (designed in house, made by Fineline Imaging, Colorado Springs, CO) with a MJB4 Mask Aligner (Süss MicroTec, Philadelphia, PA). Subsequent development removed any uncrosslinked photoresist. Using a Techni-Gold 25 ES Au solution (Technic Inc., Cranston, RI), a 25 μm thick layer of gold was plated onto the exposed portions of the seed layer over the course of 25 hr. Removing the SU-8 2015 and the metal seed layer left wires that were 90 μm wide and 25 μm tall on top of the sapphire substrate.

6.3.2 Vesicle Formation

Vesicles were formed using the electroformation technique described by Zhou and Raphael [31, 33]. Briefly, a 15 μL chloroform solution containing 1 $^{\mathrm{mg}}/_{\mathrm{mL}}$ 1-stearo-

yl-2-oleoyl-*sn*-glycero-3-phosphatidylcholine (SOPC, from Avanti Polar Lipids, Alabaster, AL) was mixed with Biotin-X DHPE (*N*-((6-(biotinoyl)amino)hexanoyl)-1,2-dihexadecanoyl*sn*-glycero-3-phosphoethanolamine, triethylammonium salt, Invitrogen, Carlsbad, CA). The Biotin-X DHPE provided receptor-ligand binding sites to streptavidin-coated magnetic beads. The resulting solution was spread on each of two platinum electrodes and placed under vacuum for at least 2 hr. The electrodes were then submerged in 100 mM sucrose solution (Sigma-Aldrich, St. Louis, MO) and exposed to an alternating voltage. After $2 - 3.5$ hr, the solution, now containing vesicles, was collected and stored in a 4 °C refrigerator. *

6.3.3 Magnetic Bead Composition

Streptavidin-coated ferromagnetic beads of 4.4 μm diameter (Spherotech) provided the point forces used to pull tethers. The beads at 1% $^{w}/_{v}$ were contained in 0.016 M PBS, pH 7.4 with 0.02% sodium azide. The 8% $^{v}/_{v}$ CrO_2 beads were diluted by a factor of 5000 in 120 mM glucose (Sigma-Aldrich) and 1 mM 10x PBS solution. Ferromagnetic beads were magnetized by exposure to a 300 mT field for at least 5 sec, which was sufficient to obtain uniform magnetic saturation of all beads.

6.3.4 Vesicle Aspiration

Vesicle aspiration was applying negative pressures through a micropipette. Employing a P-97 micropipette puller (Sutter Instrument, Novato, CA) and a custom-built

*A more detailed description of vesicle formation is given in Appendix A.

microforge, we tapered borosilicate capillary tubes (Kimble Chase, Vineland, NJ) to form micropipettes with $\sim 10\,\mu$m inner diameter. The pipettes were coated with a 1% (BSA, Sigma) solution in 120 mM glucose. Attaching the micropipette to a water reservoir with 0.1 mm resolution (Robo Cylinder, IAI, Torrance, CA) provided adjustable pressure, which was used to aspirate the vesicle within the pipette.

6.3.5 Temperature of the System due to Ramping

The temperature change of the combined MFT-aspirator system was determined in detail in Section 5.3.6. Briefly, a current waveform of square pulses of 1 A, 2 A, or 3 A was passed through the device while a vesicle was aspirated. The heating resulted in biphasic growth in temperature as seen in Figure 5.3b. The agreement between the developed numerical COMSOL model and the thermal expansivity of aspirated SOPC vesicles established the use of COMSOL to accurately imitate the thermal response of the MFT-aspirator to an electrical current stimulus.

The electrical current applied for many of the experiments in the following studies used current ramps, as opposed to current pulses. To determine the response of the system to two commonly used ramps, a numerical approximation of the system undergoing an increase in current from 0 A to 3 A over 0.5 s, 5 s or 10 s was implemented. Figure 6.1 plots the temperature changes the model predicts during and after a ramp. Unlike the response seen with a square pulse, the system does not follow a biphasic increase but rather closely follows the same form of the ramp until current halts. Fol-

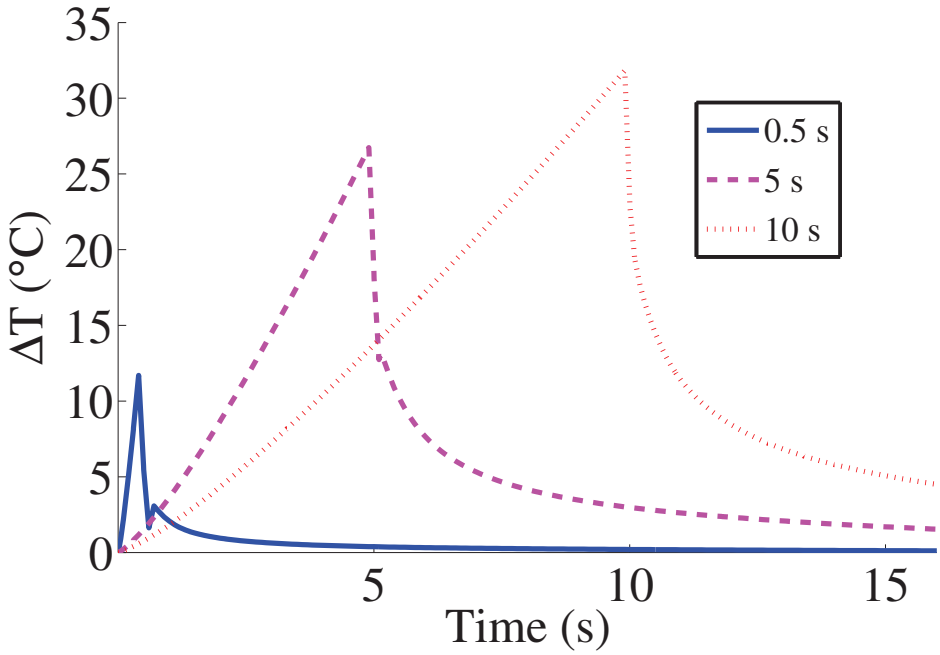

Figure 6.1 : Temperature change expected in the MFT-aspirator system during ramps in current. The ramps lasted 0.5 s (solid blue line), 5 s (dashed magenta line), 10 s (short dashed red line) and with a maximum current of 3 A in all three cases. Although all three ramps reached 3 A, the system only heated $\Delta T \sim 12\,^{\circ}\mathrm{C}$ with the 0.5 s ramp as compared to an increase of $\Delta T \sim 32\,^{\circ}\mathrm{C}$ for the 10 s ramp. The anomalous dip in the curve after the sharp decrease in temperature evident in the curves was due to overshooting of the numerical model at high slopes.

lowing this form, the short pulse of 0.5 s (ramp of 6 $^{A}/_{s}$) heats the system $\Delta T \sim 12\,^{\circ}\mathrm{C}$, while the longer pulse of 10 s (ramp of 0.3 $^{A}/_{s}$) heats the system up $\Delta T \sim 32\,^{\circ}\mathrm{C}$. The MFT rapidly cools once the current is removed. While these temperature changes are significant, no noticeable systematic effects were observed in the studies in this chapter due to temperature (see Figure 6.6a below), and the more accurate model of a ramp will be used for determining temperatures in the following sections.

6.3.6 Formation of a Tether

Tethers were formed by applying a point force to an aspirated vesicle (Figure 6.2a). Typically, the vesicle would be placed $\sim 70\,\mu$m from the wire. A current ramp (with currents no higher than 3 A and lasting no more than 10 s) raised the force applied to the vesicle. Occasionally, the force would be large enough to form a tether (Figure 6.2b), and the resulting images collected. If the force was not great enough, the vesicle-bead pair would be moved closer to the wire and another attempt at tether formation conducted. By determining the trajectory of the bead during tether formation (Figure 6.2c), the threshold force and force ramp were calculated.

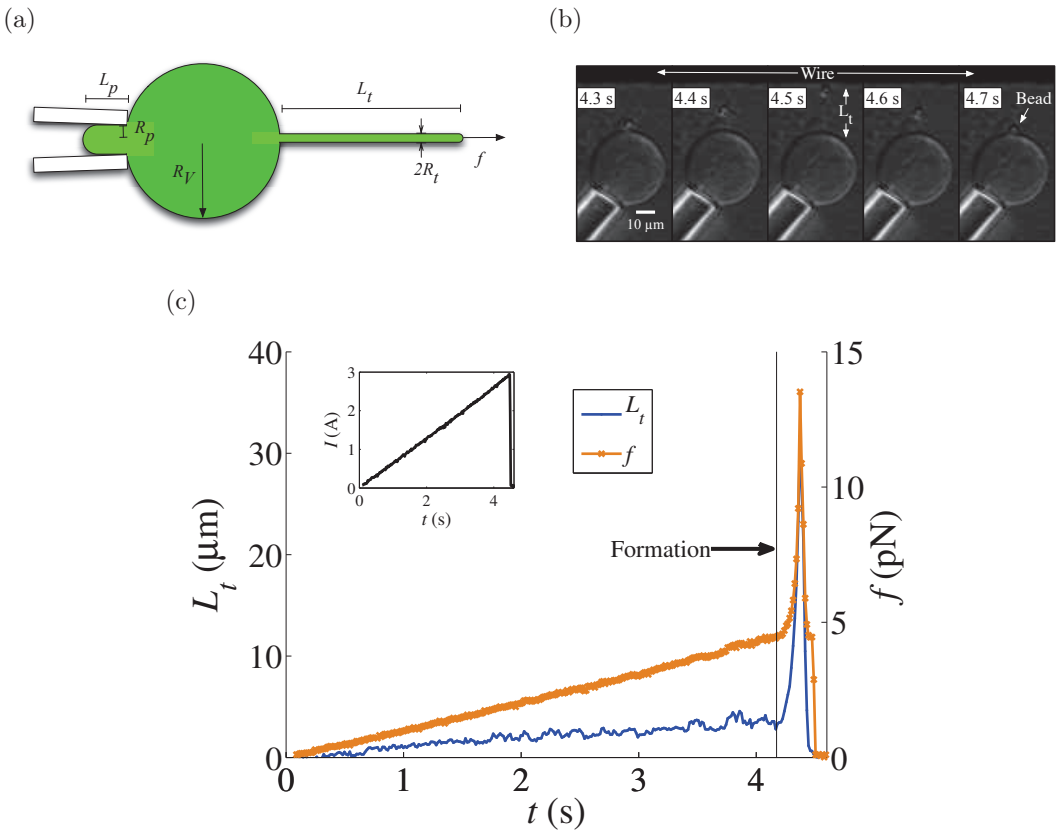

Figure 6.2 : The formation of a tether from an aspirated vesicle. (a) A schematic of a vesicle of radius R_V being aspirated by a pipette of radius R_p to a projection length L_p. An applied force f extended a tether of radius R_t to a length L_t. (b) A time sequence of a tether pulling off an aspirated vesicle. The magnetic bead, which applied the point force for tether formation, indicated the end of the tether. The bead, and tether, returned once current flow ceased. (c) The tether length and applied force during the tether extension depicted in (b). As the force increased, the membrane only slightly moved until a tether formed. At this time, L_t increased rapidly, moving toward the wire. As the distance to the wire decreased, the force correspondingly escalated in a non-linear fashion.

6.4 Results and Discussion

6.4.1 On the Dependence between Force Threshold and Rate of Applied Force

Extending work done previously in Section 5.4.3 on the applied force at which a tether forms, we have enlarged the dynamic range of the MFT from from a few $^{\mathrm{pN}}/_{\mathrm{s}}$ to over $10^4\,^{\mathrm{pN}}/_{\mathrm{s}}$. In order to vary the force ramps over this range, a variety of current ramps ($^{dI}/_{dt}$) and distances from the wire were selected. Such selection was based upon the force ramp $^{df}/_{dt}$ going as

$$\left|\frac{df}{dt}\right| = \frac{\mu_0 m}{2\pi y^2}\frac{dI}{dt} + \frac{\mu_0 m I}{\pi y^3}v, \tag{6.1}$$

where m is the magnetic moment of the bead as defined in Equations 5.5 and 5.7, and v is the velocity of the tether the instant a tether forms[†]. Force rates depended upon location, with slower force rates accessible far from the wire (see Figure 6.3a) and faster force rates accessible nearer to the wire (see Figure 6.3b). Taking advantage of the diversity of force rates accessible, the force ramps and tether formation forces of 170 tethers from 27 vesicle-bead combinations were determined. The results are plotted in Figure 6.4, and it is evident that the force threshold F_{th} depends monotonically on $^{df}/_{dt}$. Threshold forces rose from $\sim 5\,\mathrm{pN}$ at low force rates to threshold forces above 60 pN at force rates near $12000\,^{\mathrm{pN}}/_{\mathrm{s}}$. The magnitude of observed force thresholds observed for vesicles compare well to those calculated for human umbilical

[†]The velocity v was determined using the Stokes' Law as applied to the magnetic force the bead experiences. As the force the membrane exerted on the tether due to tension was on the scale of 1 pN, it was small compared to the magnetic force and was ignored.

(a)

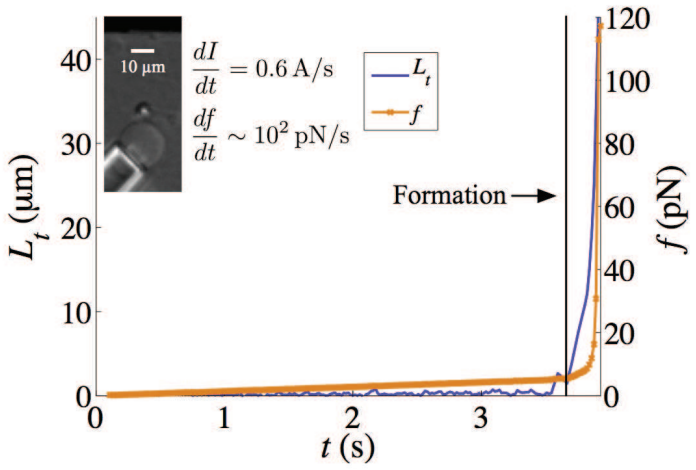

(b)

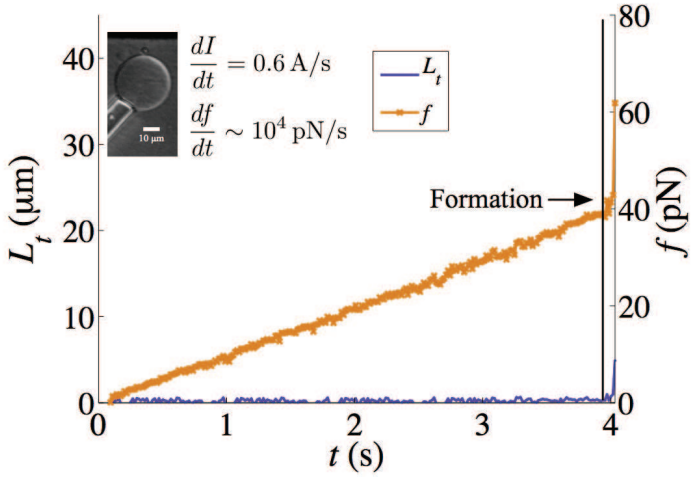

Figure 6.3 : Dependence of force rate on position. The current rate for both cases presented were 0.6 A/s. (a) As the vesicle was far from the wire, the force ramp was low ($\sim 10^2$ pN/s). The low force ramp led to a threshold force of ~ 10 pN (orange line with dots), which was indicated by the sudden increase in L_t (blue solid line). (b) Even with the same current rate, the force ramp experienced by this vesicle-bead combination was higher as it was closer to the microfabricated wire. At $\sim 10^4$ pN/s, a threshold force of ~ 40 pN initiated tether formation.

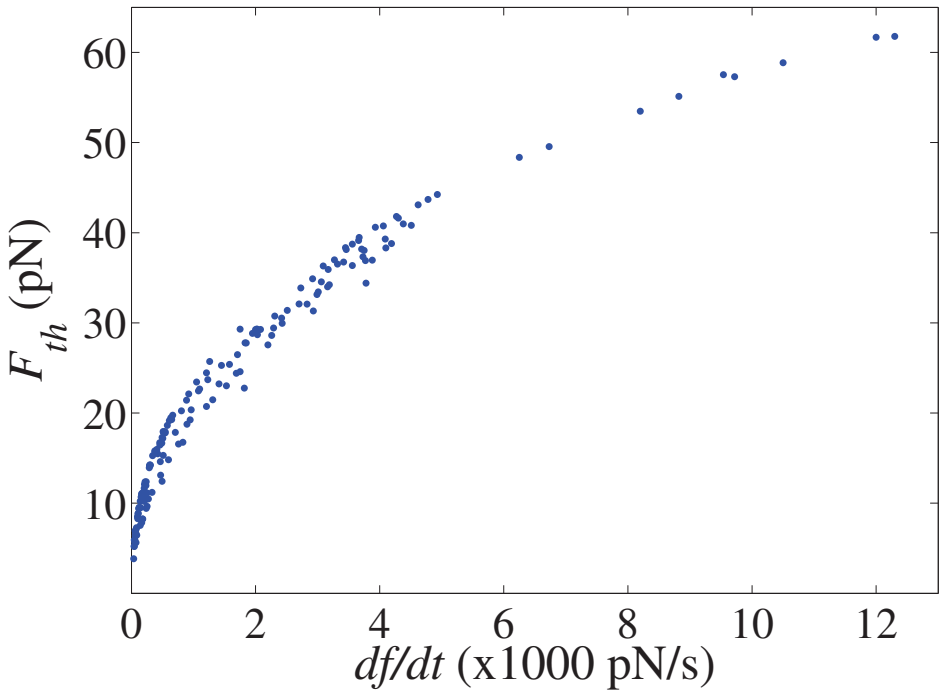

Figure 6.4 : Establishing dynamics of tether formation for SOPC vesicles containing 5 mol% Biotin. A tight relationship between the force threshold F_{th} and the applied force ramp $^{df}/_{dt}$ exists over a large range of force rates: $^{df}/_{dt}$ varies from $\sim 10^1$ pN/s to $\sim 10^4$ pN/s. An energetic model motivating the form of the dependence is developed in Section 6.4.4.

vein endothelial cells. Using only a micropipette, threshold forces for tether formation from these endothelial cells were reported as 55 pN as pressure decreased at a rate of $\sim 0.5\,{}^{\mathrm{pN}}/_{\mu\mathrm{m}^2\cdot\mathrm{s}}$ [13].

6.4.2 Verification of the Force Threshold-Force Rate Dependence

Systematics based on position, threshold current, and temperature will be investigated in this section to determine possible influence on the relationship between F_{th} and ${}^{df}/_{dt}$. To verify that the relation seen between F_{th} and ${}^{df}/_{dt}$ was not a result of some systematic dependence on location, the position y of each F_{th} corresponding to a datum in Figure 6.4 was determined and the result plotted in Figure 6.5a. A broad range of force thresholds was seen for each domain subset displayed. In some cases, particularly closer to the wire, the forces varied by several factors. The well defined maximum F_{th} at each y was the result of the current limit of a gold wire on the MFT. With this current limit, there was a maximum force each particular bead may experience when a certain distance from the wire. This systematic, nevertheless, did not explain the link between F_{th} and ${}^{df}/_{dt}$. There might have also been some interrelation between the current at which a tether forms I_{th} and the force ramp, and this could have led to the dependence seen in Figure 6.4. Plotting each pairing (see Figure 6.5b) revealed that much as F_{th} failed to vary tightly with y, I_{th} also did not depend tightly on ${}^{df}/_{dt}$. In particular, at force ramps below $5000\,{}^{\mathrm{pN}}/_{\mathrm{s}}$, the threshold current ranged from at least 1.5 A up to 3 A, which was half the available current

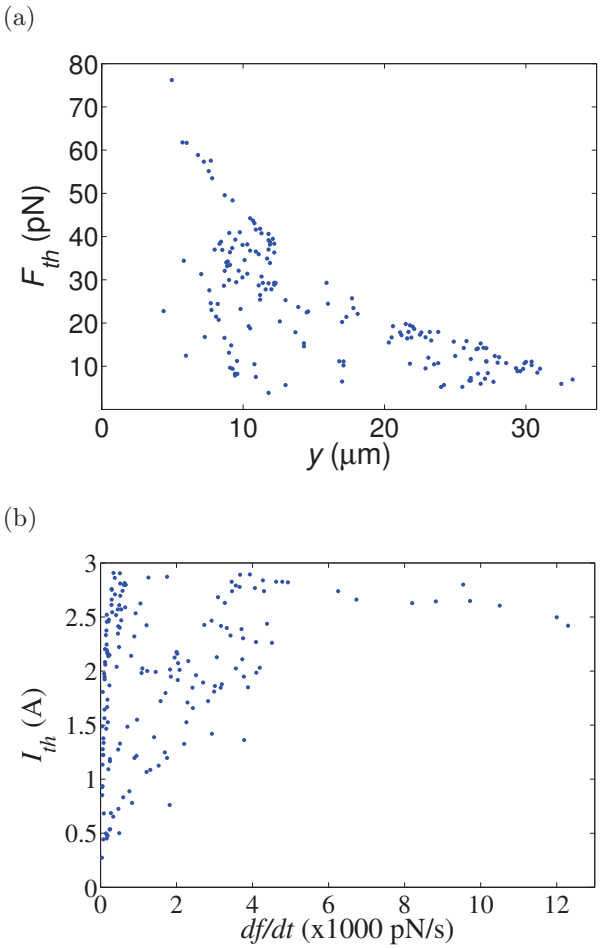

Figure 6.5 : Investigating the correlation of location and current thresholds on force thresholds and force ramps. (a) F_{th} did not systematically depend upon the distance to the wire y. While there appeared to be a maximum force that a tether will form at each y, there was no lower bound. (b) The current at which a tether forms I_{th} did not depend upon $^{df}/_{dt}$, but rather only had certain values that are accessible at each force ramp. As the force ramp increased, the envelope available to I_{th} narrowed to around 2.5 A for some, as yet unknown, reason.

range. At much lower force ramps ($^{df}/_{dt} \lesssim 10^2\,^{\mathrm{pN}}/_{\mathrm{s}}$), however, I_{th} varied across its entire range. The range in threshold current did narrow as the force ramp increased, indicating that at lower $^{df}/_{dt}$, a large phase space was accessible to I_{th}. Although such a narrowing appeared, the dependence of F_{th} on $^{df}/_{dt}$ did not purely derive from a systematic parallel between $^{df}/_{dt}$ and I_{th}.

The change in temperature in the system due to Joule heating also might have significantly influenced the link between force threshold and force ramp observed. As seen in Figure 6.1, the temperature increase in the system associated with this and later data modulated from below 12 °C (with a linear current ramp lasting 0.5 s up to 1.5 A) to over 27 °C (with a ramp lasting 10 s up to 3 A). To investigate the effect temperature might have had on the force threshold, we determined the temperature at which each thresholding event took place using the calculated COMSOL models. The spread seen in F_{th} over a temperature range of $\Delta T \sim 6\,\mathrm{K}$ to over $\Delta T \sim 30\,\mathrm{K}$ is given in Figure 6.6a. F_{th} ranged from $5 - 20\,\mathrm{pN}$ at $\Delta T \sim 6\,\mathrm{K}$ to $10 - 80\,\mathrm{pN}$ at $\Delta T \sim 30\,\mathrm{K}$. The greater spread at higher temperatures was a result of the increased heating that occurred at high force thresholds. Even though the spread in F_{th} widened at higher temperatures, the correlation between force thresholds and changes in temperature was weak ($R^2 < 0.25$ with a best-fit linear regression). While the change in temperature of the system affected the areal strain of vesicles (see Section 5.3.6), it did not significantly influence the threshold force of tether formation.

Systematics based on position, threshold current, and temperature have so far

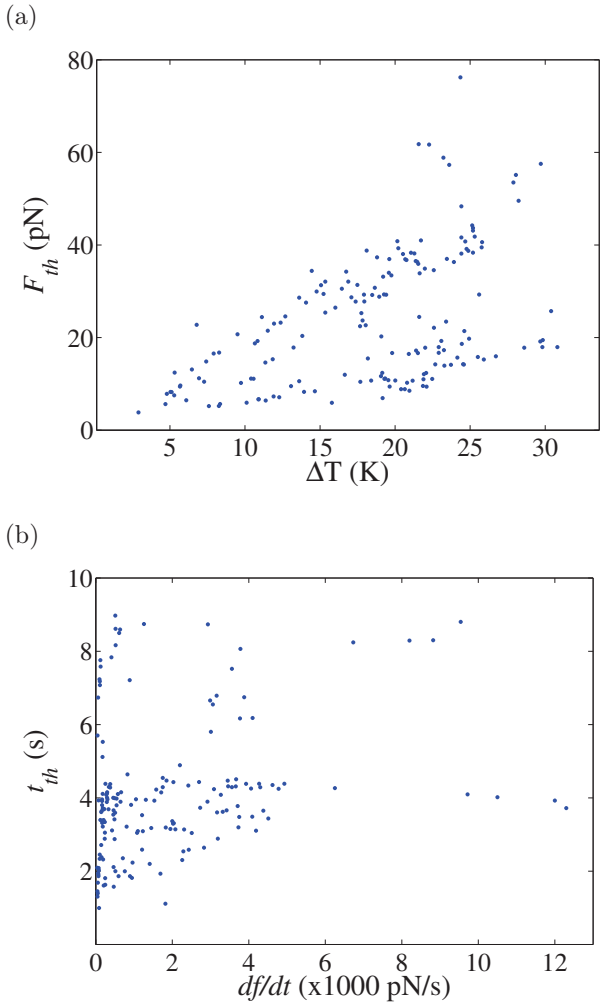

Figure 6.6 : The influence of temperature on threshold forces of tether formation and the correlation of the time to tether formation on applied force ramp. (a) Although the temperature change in the MFT might have been significant, there was only a weak correlation between F_{th} and ΔT. As evident by the spread in threshold forces at both low and high temperature changes, ΔT had little effect on the threshold force. The correlation observed was rather due to high F_{th} requiring more current, resulting in heating. (b) The rate of force application did not determine how long, t_{th}, it took a tether to form; there was a broad range of values of t_{th}.

been investigated and found to not influence the relationship between F_{th} and $^{df}/_{dt}$. As a final systematic, we examined how the time it takes a tether to form, t_{th}, depended on force ramp. As seen in Figure 6.6b, t_{th} ranged from 1 s to 9 s for the tethers pulled from the SOPC vesicles with 5 mol% biotinylated lipids even as $^{df}/_{dt}$ spanned from $10 - 10^4$ $^{\mathrm{pN}}/_{\mathrm{s}}$. At high force rates ($> 5x10^4$ $^{\mathrm{pN}}/_{\mathrm{s}}$), tethers pulled at the greatest extent of time possible for the respective ramp ($\sim$ 5 s or $\sim$ 10 s), but there was a bias at high force rates. The forces necessary to pull a tether only occurred at longer times. At lower force ramps with threshold forces accessible earlier, there appeared to be little correlation between t_{th} and $^{df}/_{dt}$. After having examined position, threshold current, temperature, and threshold time, the relationship between F_{th} and $^{df}/_{dt}$ did not depend upon any of these aforementioned systematics.

6.4.3 A One Barrier Energy Model

In this section, we examined the applicability of a one barrier energy model to describe the dependence of the observed threshold force of tether formation on the rate of applied force[‡].

The logarithmic-like growth of F_{th} with respect to $^{df}/_{dt}$ displayed in Figure 6.4 was reminiscent of the expected response of a system to a single energy barrier [14, 43–45] Assuming tether formation was characterized by an energy well and a single barrier, a possible energy landscape would be similar to the landscape seen in Figure 6.7a.

[‡]A model based upon Newtonian mechanics was developed in Appendix C. While initially promising, the Newtonian model was eventually discarded.

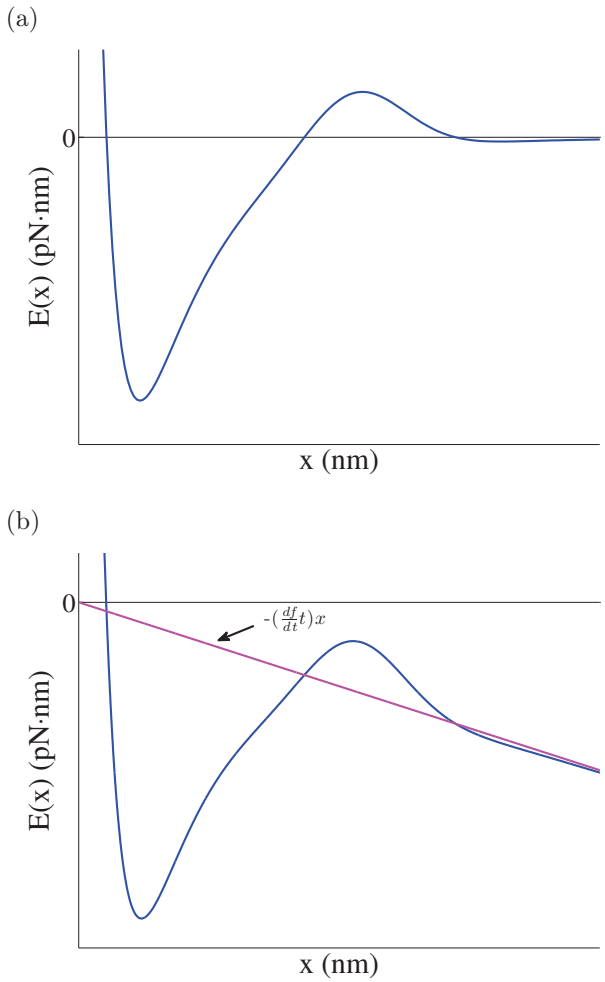

Figure 6.7 : A one barrier energy model. (a) The potential energy E (x) describing the tether system as a function of tether extension x when one energy barrier resists tether formation. (b) A force $(df/dt)\,t$ resulting from a ramp df/dt tilted the energy barriers, resulting in a decreased barrier height. These plots are based on those sketched out by Evans [44].

Normally, a membrane would sit in the energy well and only surmount the barrier to form a tether when thermal energy was high enough to surmount the barrier, as developed in Section 2.3. However, if a force was applied to the system, the energy barrier would decrease as displayed in Figure 6.7b, increasing the probability that a tether would form. Using the development of interpreting energy barriers presented in Section 2.3, the force threshold F_{th} while a constant force ramp $^{df}/_{dt}$ is being applied to a system consisting of a single energy barrier is

$$F_{th} = f_\beta \ln\left(\frac{t_{off}}{f_\beta}\frac{df}{dt}\right), \tag{6.2}$$

where t_{off} is the reciprocal of the barrier escape rate when F_{th} goes to zero, and f_β is the force scale determined by the ratio of the thermal energy to the location of the energy barrier [44]. Equation 6.2 shows that, if tether formation can be explained by a single energy barrier, then the force threshold goes as the natural log of the force ramp and would appear linear on a semilog plot. Figure 6.8 depicts the data given in Figure 6.4 on such a plot with a fit for the one barrier model. As is readily evident from the graph, the one barrier model does not describe the form of the force threshold-force ramp correspondence. A more involved model is needed to account for the more elaborate dependence between F_{th} and $^{df}/_{dt}$.

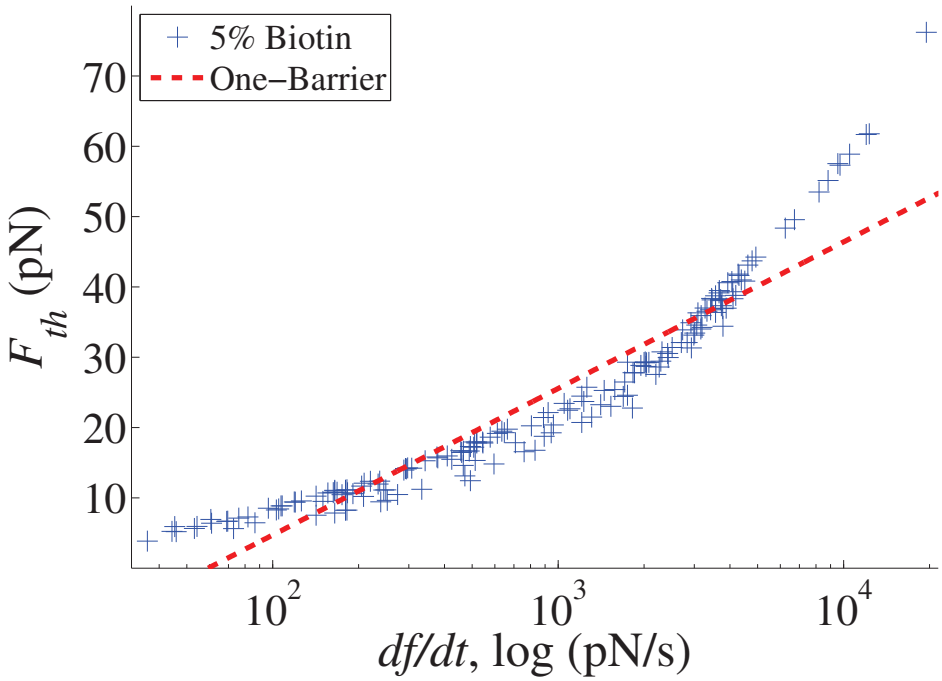

Figure 6.8 : Modeling the data of Figure 6.4 assuming a one barrier energy model. Using the development of Evans [44] for one barrier, the force threshold related logarithmically to the force ramp and appeared linear on a semilog plot (red dashed line). Comparing the one-barrier model to the 5 mol% biotin data (blue crosses) showed that a single barrier model did not describe the observed data well.

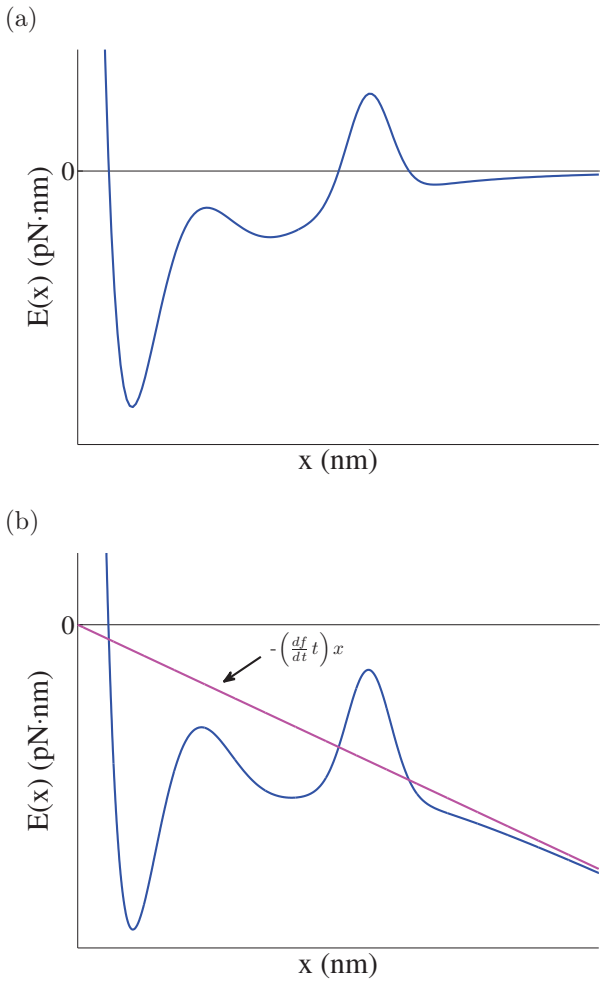

Figure 6.9 : Two barrier energy models for the tethering system. (a) An energy landscape with two barriers hinted at a more involved description of tether formation. (b) A ramp $^{df}/_{dt}$ tilted the energy landscape, resulting in decreased barrier heights and a reversal of which barrier dominated, yielding a two regime system. These plots are based on those sketched out by Evans [44].

6.4.4 A Two Well Energy Model

This section develops a more involved model to explain the correlation of F_{th} and $^{df}/_{dt}$. Assuming the separation of a biotinylated lipid and its immediate neighboring lipids from the membrane is analogous to the separation of a receptor from a ligand [44] or to the rupturing of vesicles with increasing tension [14], then the energetics of the separation may be explained with an energy well and associated barriers, as seen in Figure 6.9a. Barriers in the tether system could include the energy needed to bend a membrane, to cause the membrane to flow against drag, or to separate the outer leaflet from the inner before bending of both leaflets.

Regardless of the possible sources of the assumed barriers, the potential energy—well and barriers—could be lowered through the imposition of an externally applied force [43, 44]. A force that changes at a rate $^{df}/_{dt}$ would lower the potential energy with increasing extension of the membrane and increasing time, as seen in Figure 6.9b. Such lowering not only reduced the barrier heights, modifying which barrier dominated. Using Equation 2.40 with $n = 2$, the force ramp $^{df}/_{dt}$ can be related to tether thresholds F_{th} by

$$\frac{df}{dt} = \left(\frac{t_{off,1}}{f_{\beta,1}} e^{-F_{th}/f_{\beta,1}} + \frac{t_{off,2}}{f_{\beta,2}} e^{-F_{th}/f_{\beta,2}} \right)^{-1}, \tag{6.3}$$

where $t_{off,i}$ and $f_{\beta,i}$ are as defined in Section 6.4.3 for each respective barrier i. Equation 6.3can be understood intuitively as the formation of a tether occurring

when the inverse of the characteristic observation time as determined by the force ramp is equal to the transition rate [44].

Examining the system at high and low force ramp $^{df}/_{dt}$ for SOPC vesicles with 5 mol% biotinylated lipids yielded fit parameters given in Table 6.1. The parameters characterized each regime with the resulting fits plotted in Figure 6.10. At low $^{df}/_{dt}$, the system sampled a barrier, at $x_\beta = 1\,\text{nm}$, characterized by $f_\beta = 4\,\text{pN}$, while at high $^{df}/_{dt}$, a barrier with a displacement at $x_\beta = 0.2\,\text{nm}$, characterized by $f_\beta = 21\,\text{pN}$, was accessed. The reciprocal of the attempt rate t_{off} also dropped significantly at higher $^{df}/_{dt}$, which was expected as higher forces lead to lower lifetimes in the energetic framework presented [91]. While an energy barrier model has not before, to the best of our knowledge, been applied to studying tether formation from vesicles, it has been applied to biotin-streptavidin de-attachment [75] and membrane lysis with applied tension [14]. For receptor-ligand rupture, magnitudes for f_β of 8 pN and 34 pN were measured [75]. Likewise, the values of f_β for membrane lysis could be estimated from reported stresses and were 13 pN and $\sim 300\,\text{pN}$ [14]. These forces indicate that the reported levels of f_β in our system are of the general correct order of magnitude. t_{off} is related to the barrier height with no force applied and the attempt frequency. If we had information on one of these parameters, we could extract the other. The barrier height would in particular be very interesting to know, as it reveals the energy levels that govern the system. Attempt frequencies are difficult to estimate as they are determined by diffusive relaxation time, which is dependent upon the diffusion in the

Table 6.1 : Values corresponding to the fits presented in Figure 6.10. Errors are standard deviations.

	f_β (pN)	t_{off} (ms)
Barrier 1	4.3 ± 0.2	230 ± 12
Barrier 2	20.9 ± 1.3	34 ± 2

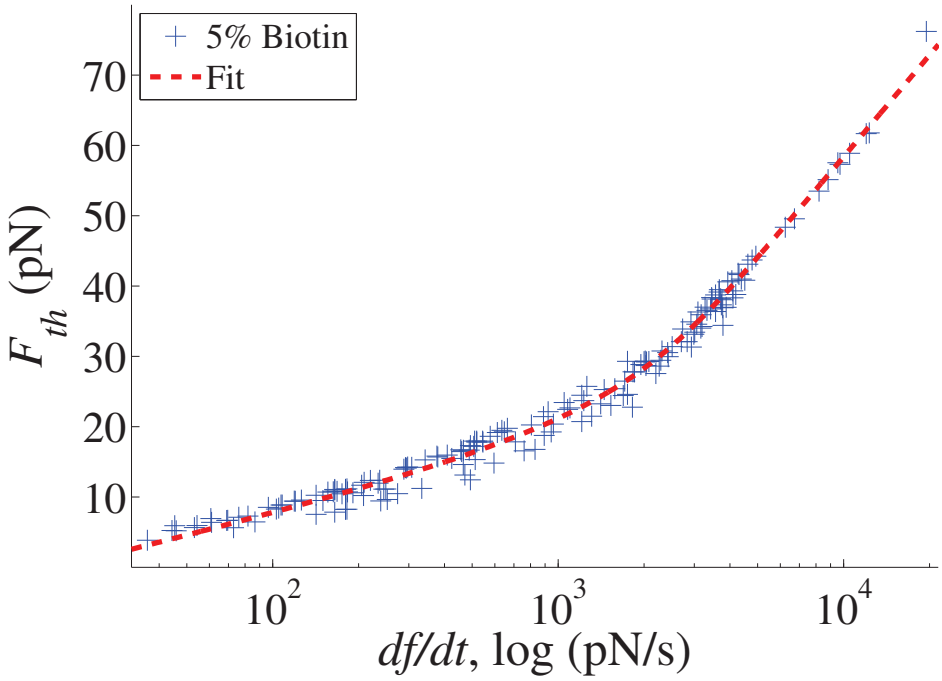

Figure 6.10 : Application of the two-barrier model to force ramp dependent thresholding events for 5 mol% biotinylated SOPC vesicles. The two-barrier model (red dashed line, $f_{\beta,1} = 4.3 \pm 0.2\,\mathrm{pN}$, $t_{off,1} = 230 \pm 12\,\mathrm{ms}$, $f_{\beta,2} = 20.9 \pm 1.3\,\mathrm{pN}$, $t_{off,2} = 34 \pm 2\,\mathrm{ms}$) fitted the observed data (blue crosses from 170 tethers, 27 vesicle-bead combinations) over several orders of magnitude and showed a transition between the two states at ${}^{df}/_{dt} \sim 760\,{}^{\mathrm{pN}}/_{\mathrm{s}}$.

system and the local curvature of the energy landscape. While the diffusion coefficient of the membrane can be approximated as $10^{-3} - 1\,{}^{\mu m^2}/_{s}$ [19], the local curvature of the energy landscape is unknown. The local curvature of energy can further adjust attempt frequencies by up to 6 orders of magnitude between diffusion relaxation and experimentally measured rates [44]! Even though the attempt frequency, and hence the energy barrier, can be difficult to determine, the values of t_{off} we obtained are one the scale of other mesoscopic systems. In delinking of receptor-ligand pairs, t_{off} varied from $10^{-5}\,s$ to $\sim 30\,s$ depending upon number of bonds involved with the coupling [44]. In membrane rupture experiments, t_{off} ranged from $0.125\,s$ to $\sim 11\,s$. Our report of the values of t_{off} are also reasonable in relation to other biophysical systems. Comparing F_{th} to ${}^{df}/_{dt}$ enables the study of the energy landscape of tether formation, and while the mechanisms for formation are still being investigate, this landscape appears to be a two barrier process

6.5 Improvements

While the combined magnetic force transducer-microaspirator system has formed a novel system and has been used to discover a relationship between the force threshold needed to pull a tether and the rate of force application, the system could be improved to allow yet a greater variety of experiments. These improvements are the implementation of higher forces further from the wire, increased camera capabilities, and improved adhesion rates between receptors and ligands. To pull tethers from

cells, forces on the order of tens of piconewtons must be applied [13, 103]. And in order to investigate the effect of curvature, especially the contribution of differential areas or non-local bending, tethers of several hundred microns must be formed [12]. Large forces far from the wire may be attained by using beads with increased magnetic content or larger volumes. A device with increased cross-sectional area of the gold wire would also allow augmented current flow with less heating, leading to escalated applied forces. Large and uniform forces may be achieved by using paramagnetic beads experiencing forces caused by a large uniform background field $\mathbf{B}_{bkgd}$ and a magnetic field caused by the gold wire $\mathbf{B}_{wire}$ with a high gradient. In this situation, the force a paramagnetic bead experiences due to a total magnetic field $\mathbf{B}_{total} = \mathbf{B}_{wire} + \mathbf{B}_{bkgd}$ with a magnetic moment $\mathbf{m} \propto \mathbf{B}$ would be

$$\begin{aligned}
\mathbf{F}_{para} &= \nabla\left(\mathbf{m}\cdot\mathbf{B_{tot}}\right) \propto \nabla\left(\left|\mathbf{B_{wire}}+\mathbf{B_{bkgd}}\right|^2\right) \\
&= 2\left|\mathbf{B}_{wire}+\mathbf{B}_{bkgd}\right|\cdot\nabla\left|\mathbf{B}_{wire}+\mathbf{B}_{bkgd}\right| \\
&\propto \mathbf{B}_{wire}\cdot\nabla\left|\mathbf{B}_{wire}\right| + \mathbf{B}_{bkgd}\cdot\nabla\left|\mathbf{B}_{bkgd}\right| \\
&+ \mathbf{B}_{wire}\cdot\nabla\left|\mathbf{B}_{bkgd}\right| + \mathbf{B}_{bkgd}\cdot\nabla\left|\mathbf{B}_{wire}\right| \\
&\approx \mathbf{B}_{bkgd}\cdot\nabla\left|\mathbf{B}_{wire}\right| \qquad (6.4)
\end{aligned}$$

since $\mathbf{B}_{wire} \ll \mathbf{B}_{bkgd}$ and $\nabla\mathbf{B}_{bkgd} \ll \nabla\mathbf{B}_{wire}$. As such, with a large background field and magnetic field gradient, a large force may be applied to a paramagnetic bead even far from the wire. These increased forces would facilitate experiments on cells

far from the wire, allowing long tethers to be pulled.

Increased camera capabilities entail increased spatial and temporal resolution. Augmented spatial resolution enables more accurate measurements of tether length, vesicle radius, and vesicle projection, improving error. Higher camera frame rates achieves greater temporal resolution. With such an improvement, the force threshold could be determined more accurately. Furthermore, the full trajectory during both extension and return would be more fully determined, enabling force-extension curve calculations and greater accuracy of dynamic parameters, such as interlayer drag. Greater spatial and temporal resolution, via an upgraded camera promotes more accurate measurements of several mechanical properties.

Tether experiments are tedious affairs due to the low success rate of forming the receptor-ligand bond between the streptavidin-coated magnetic bead and the biotinylated lipid. Using an alternate receptor-ligand combination, such as an antibody-antigen pair [12], may possibly improve success rates of binding, greatly increasing data collection times. However, biotin-streptavidin bonds are generally known as the strongest non-covalent bond, so other receptor-ligand combinations may not be very helpful. Nonetheless, increasing binding rates, if possible, would improve the system.

6.6 Outstanding Questions

The relation between threshold force and force ramp is quite tight but is not expected to be. For example, Evans estimated that the the minimum fluctuation in threshold

force for one energy barrier should be equal to f_β [44]. Extending to two dissimilar barriers, we estimated that the deviation in F_{th} should be on the order of $> 10\,\mathrm{pN}$ for the control data. However, observed deviations were on the order of a few piconewtons. Lower than expected noise has been seen in receptor-ligand de-binding events [44]. In the more related membrane lysis studies, however, observed noise matched theory [14]. The source of the tighter data in our system though remains unclear.

Although it has not been studied in this thesis, the effective success rate of tether formation under a certain set of conditions (pressure, location, current ramp, current strength, osmolarity, freshness of lipids) was less than 50%. However, when a tether does form, the observed force at which it forms, F_{th}, depends closely on $^{df}/_{dt}$. This implies some duality of configurations of the system. If the system were purely stochastic, a spread in F_{th}, at least above a minimum force threshold, would be expected. Further, greater variation in times to threshold when pulses were applied (see Appendix C) would have been expected. These results imply that there is some systematic that we are not controlling that can configure the system in such a way that tethers do not form. Possible systematics include beads pinning to the substrate or much larger contact areas between the bead and vesicle. However, beads were typically seen to move freely along the membrane, and intermediary contact areas would also be expected to be observed. It is unclear what this hidden systematic may be.

6.7 Summary

Tethers are increasingly being recognized as a vital structure for many biological functions, ranging from initiation of changes in cell morphology and function to the transfer of material from one cell to another. To understand this behavior further, many studies have been conducted, experimentally and theoretically, into the dynamics of tether motion and formation and into the adhesion sites that facilitate tether formation. However, no studies had yet examined the dependence of tether formation on force ramp from a simple model system: the vesicle. In this work we examined the link of the threshold force of tether formation on the time derivative of the applied force. We further examined the effect of several possible systematics on the relationship between force threshold and force ramp, including position, threshold current, temperature, and threshold time. However, none of these other variables correlated with the force threshold or force ramp. A two-barrier model was found to describe the observed behavior between threshold force and force ramp. Using this model, the dependence between threshold force and force ramp can be used as a means to investigate the energy landscape of tether formation. In the next chapter, we examine how membrane modulators, such as the presence of cholesterol in the membrane, affected the system.

Chapter 7

Investigating the Effect of Modifiers on Tether Formation Dynamics

All life is an experiment. The more experiments you make, the better. - Ralph Waldo Emerson [104]

In the previous chapter, a two barrier energy model was proposed and used to interpret the observed dependence of the threshold force of tether formation as a function of applied force rate in 1-stearoyl-2-oleoyl-*sn*-glycero-3-phosphatidylcholine (SOPC) vesicles. This interpretation led to possible information about the energy landscape of tether formation including the presence of two barriers and details of these barriers. To continue upon this development, we proposed several variations of the system that could expand on our understanding of this energy landscape. Below, we present preliminary studies of these variations. For the majority of the assays, the modifiers only subtly influenced the relationship between observed threshold force of tether formation and force ramp. One investigation on concentration of biotin-streptavidin bonds did show a more drastic result, but was difficult to reproduce from one lipid stock to another. Even with the difficulties though, the trends noted are suggestive and point to future work that may show the potential of the combined magnetic force transducer (MFT)-aspirator system to probe membrane mechanical and energetic behavior.

7.1 Introduction

The mechanical properties, such as bending modulus or interlayer drag coefficient, of a membrane tether are primarily determined by the properties of the dominant lipid constituent, such as SOPC. However, even small amounts of different lipid constituents may greatly affect membrane properties. In this chapter, we investigated how variation based upon cholesterol concentration, tension, biotinylated lipid concentration, and concentration of the charged lipid 1-stearoyl-2-oleoyl-*sn*-glycero-3-phospho-L-serine (SOPS) modulated the force threshold-force rate dependence for tether formation investigated previously (see Chapter 6).

Cholesterol modulates membrane mechanical properties by increasing the lipid structural order parameter, or the packing parameter (see Section 2.2.2). The increased packing effects the formation of phases, including liquid-disordered and liquid-ordered states [19]. At concentration of 25 mol% and 35 mol%, these phases were observed for vesicles similar in composition to those examined here [20]. These phases increase the bending modulus [35, 36] and the compressibility [36] of a membrane. We investigated below whether it also influenced tether formation.

In addition to influencing membrane mechanics through cholesterol, modifying the pressure difference applied to an aspirated vesicle directly adjusts the tension within a membrane, which may affect tether formation [29]. By using the microaspirator in the joint magnetic force transducer-aspirator system, the pressure can be easily modified to examine the threshold force of tether formation as the applied force ramp

varied.

Receptor-ligand concentrations, such as biotin-streptavidin bonds, are known to influence de-adhesion of cells and vesicles from surfaces [74] based upon contact area and bond strength. While strength of the streptavidin-biotin bond was not investigated in this work, a decrease in contact area would lead to fewer lipids being involved in tether formation. Such a reduction could reduce the energies required to pull a tether.

Phosphatidylserine is a singly charged lipid headgroup that increases the interfacial exclusion pressure of the membrane [105]. SOPS, whose head group is phosphatidylserine, may adjust the bending of the membrane, and so influence tether formation.

This chapter reviews the modifications to the materials and methods of previous studies in order to enable the assays outlined above. Initial results of each assay—cholesterol, tension, receptor-ligand, and phosphatidylserine—are then presented and reviewed in the context of the two barrier energy model. Finally, open questions and possible overall improvements to this system are discussed.

7.2 Materials and Methods

The majority of the materials and methods used in this chapter mirror those of Section 6.3. Modifications to the previous experiments included the use of cholesterol and SOPS, and the variations on the concentration of Biotin-X-DHPE (*N*-((6-(biotin-

oyl)amino)hexanoyl)-1,2-dihexadecanoyl*sn*-glycero-3-phosphoethanolamine, triethylammonium salt, Invitrogen, Carlsbad, CA). Further adjustments consisted of the introduction of a humidity chamber and the improvement of the solution chamber in order to stabilize neutral pressure drift.

7.2.1 Lipids

Cholesterol (25 mg powder from Avanti Polar Lipids, Alabaster, AL) was diluted to 1 $^{\text{mg}}/_{\text{mL}}$ using ACS grade chloroform and added to SOPC stock solution to concentrations of 25 mol%, 35 mol%, or 45 mol%. Similarly, SOPS (10 mg powder from Avanti Polar Lipids) was diluted to 1 $^{\text{mg}}/_{\text{mL}}$ and added to SOPC stock solution to a concentration of 10 mol%. Biotin-X-DHPE varied in concentration from 1 mol% to 5 mol% for biotin studies. Exact compositions are given in Appendix A, and all lipid stocks for a study were made at the same time to ensure evaporation of chloroform between stocks was kept to a minimum. Using the otherwise standard vesicle making protocol safeguarded uniformity between vesicle batches.

7.2.2 Humidity Chamber

A humidity chamber was constructed to reduce the changes in neutral pressure in the micropipette and in the osmolarity of the dextrose solution during experimentation. This humidity chamber was constructed from a commercially-available thick-walled storage plastic container; the container was machined to allow access to the solution chamber by the microaspirator and current wires. Drilling through the large flat

surface of plastic and bonding a coverslip atop facilitated optical visualization through the humidity chamber. One additional modification was made to the container to turn it into a humidity chamber; a port in the back of the chamber connected to three sequential bubblers filled with doubly-deionized water and fed with N_2 (g). The bubbling raised the relative humidity within the chamber consistently between 95 and 99%. Such high humidity lowered the rate of evaporation, leading to more stabile levels of neutral pressure—as seen in Figure 7.1—and solution osmolarity. An added benefit to using nitrogen gas in the humidity chamber was a general increase in the stability of vesicle integrity and the long-term strength of the biotin-streptavidin bond.

7.2.3 Solution Chamber

To further reduce the drift seen in the neutral pressure of the microaspirator, the PDMS chamber used in Chapter 5 was replaced with a plexiglass chamber. The new chamber had a larger volume at $\sim 1\,\text{mL}$ but was placed in a similar location. While the increased volume and the change in material properties of the chamber affected the thermal calculations expounded upon in Section 5.3.6, the relevant temperature within the system would have been lower due to the high heat capacity of water. As the temperatures would be lower than before, the temperatures calculated in Appendix B will be used as conservative estimates of the actual thermal state of the system for the following work. In addition to a change in heat distribution, the new

chamber introduced another change: the use of vacuum grease to adhere the chamber and coverslip. As vacuum grease is inert, no ionic contribution to the solution was expected or seen. Overall, no effects were seen in the experiments due to this new ingredient.

Even though the experiments were unaffected, care had to be taken when removing the grease in order to not harm the electromagnet. Dripping $\sim 10\,\mathrm{mL}$ chloroform on the grease while titled, followed by a clean with ethanol, methanol, and N_2 (g), cleaned the MFT sufficiently while leaving the wires intact. Wiping the grease with lens paper slightly damaged the wires while hexane spread the grease. Acetone had little effect as it evaporated too quickly to dissolve much grease, and letting chloroform sit on the transducer simply spread the grease around as little globules. Regardless of the extra care required to maintain the chamber and MFT, the drift of the neutral pressure reduced to between $1\,{}^{\mathrm{Pa}}/_{\mathrm{hr}}$ and $10\,{}^{\mathrm{Pa}}/_{\mathrm{hr}}$. Figure 7.1 depicts the change in neutral pressure Δp_0 over several hours over the course of a typical experiment. Over the course of over 3 hr, the rate of change in Δp_0 kept consistent at $3\,{}^{\mathrm{Pa}}/_{\mathrm{hr}}$. The increased stability greatly improved the length of time a vesicle-bead pair could be used.

7.2.4 Tension Determination

Most of the studies presented below focus on how the material composition of the membrane affected the force threshold-force rate relationship previously observed. One study, though, made use of the adjustability of the water reservoir to study

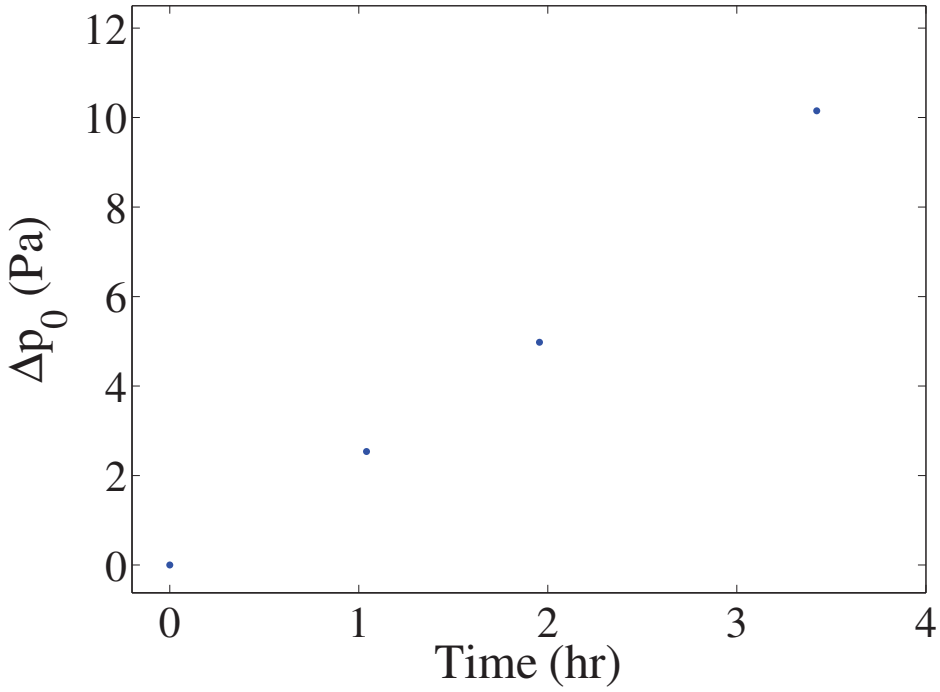

Figure 7.1 : Sample drift in the neutral pressure. With the addition of the humidity chamber and the modified solution chamber, the change in the neutral pressure, Δp_0, in this sample was a constant $3\,{}^{\mathrm{Pa}}/_{\mathrm{hr}}$ over 3.5 hr. Typical neutral pressure drifts ranged from $1\,{}^{\mathrm{Pa}}/_{\mathrm{hr}}$ to $10\,{}^{\mathrm{Pa}}/_{\mathrm{hr}}$.

membrane tension. Equation 2.14 gave a relationship between tension and pressure:

$$\tau = \frac{\Delta p}{2} \frac{R_p}{1 - {}^{R_p}/_{R_V}}. \tag{7.1}$$

By adjusting the pressure, the tension was proportionally adjusted. During tension studies, the position of the vesicle, rate at which the current increased in the electroplated gold wire, and the tension were adjusted until a tether formed. Once a tether formed, the position and current ramp would be held constant while the pressure was adjusted in $1 - 2\,\mathrm{Pa}$ increments.

7.2.5 Tethering Protocol

For the modifier studies, we implemented a standard method to obtain tethers. Once a vesicle-bead combination was brought to the wire, it would be placed $\sim 70\,\mu\mathrm{m}$ from the wire. The pressure would then be adjusted until the length of the projection was roughly equal to the diameter of the pipette. A current ramp of $0.6\,{}^{\mathrm{A}}/_{\mathrm{s}}$ would subsequently be applied for 5 s, reaching a maximum current of 3 A. If no tether formed, a lower current ramp would be applied ($0.3\,{}^{\mathrm{A}}/_{\mathrm{s}}$ for 10 s) or the pressure reduced by 1 Pa. If still no tether formed, the pressure would either be reduced further in 1 Pa increments until no more than $\sim$ 3 Pa above neutral pressure or the vesicle-bead combination would be moved $\sim 20\,\mu\mathrm{m}$ closer to the wire and the ramp and pressure protocol repeated. Once a tether formed and returned, at least 1 min passed before

the next attempt to pull a tether took place. A minimum of 3 tethers were taken at each condition. After forming at least 3 tethers, the location would then be varied for the vesicle-bead combination in order to access a variety of force ramps. If the tether stopped forming, the pressure would be reduced in 1 Pa increments or a lower current ramp used in order to try to form another tether. Finally, for the tension studies, the location of a vesicle-bead combination would not be varied (once tethering had commenced) until several pressures were set for each location (usually up to 6 Pa lower and $1 - 2$ Pa higher).

7.3 The Effects of Membrane Modifiers on Tether Formation

In this section, we examine how various modulations to the vesicle—cholesterol concentration, tension, biotin concentration, and phosphatidylserine concentration—influence tether formation. While these preliminary studies will show that many of the effects are subtle, the energetic model introduced in Chapter 6 may be used to suggest possible subtle trends in the modifiers' influence on the energy landscape of tether formation.

7.3.1 Cholesterol

Cholesterol is known to affect the mechanical properties of membranes. Cholesterol alters the lateral diffusion of phospholipids within the membrane [106], the development of phase separated states [20, 21], the bending elastic constant [107], the

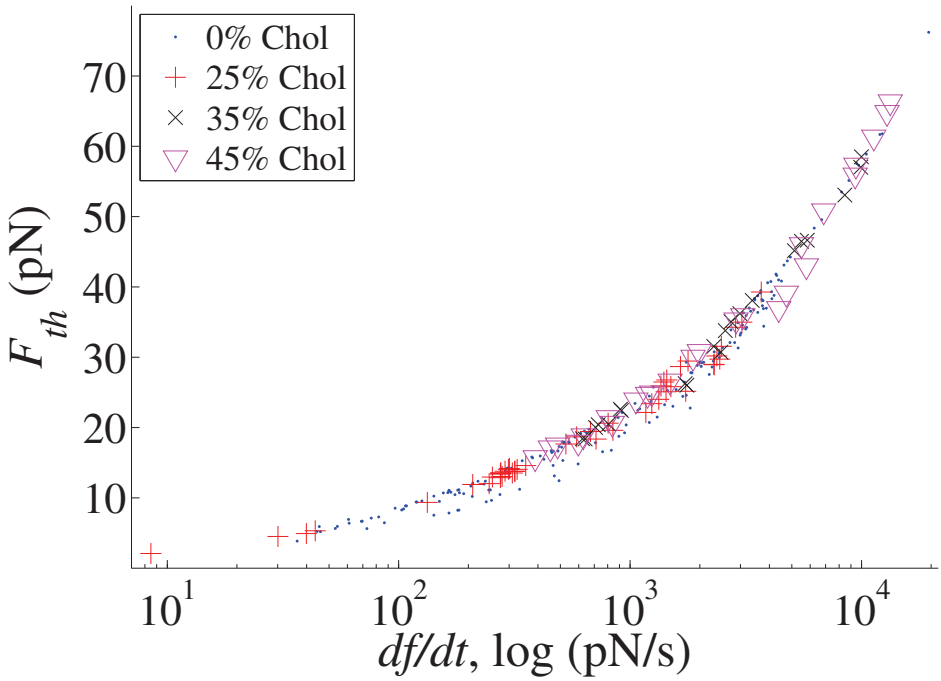

Figure 7.2 : The result of cholesterol on the dependence of observed force threshold on the force ramp. While the form of the relationship did not vary appreciably, fewer tethering events were noted at lower force ramps when cholesterol concentrations were 35 mol% or 45 mol%, indicating that other mechanisms not describable by the two-barrier model might influence tether formation. However, additional data is needed to verify this possibility.

elastic moduli [108], and the curvature [40, 109]. To study the perturbation caused by cholesterol on tether formation, the composition of the membrane was altered to include 25 mol%, 35 mol%, or 45 mol% cholesterol. The subsequent tether pulling experiments formed the basis of the force threshold-force ramp magnitude curves, which may be seen in Figure 7.3.

For 25 mol%, 35 mol%, and 45 mol% cholesterol, the form and magnitude between F_{th} and $^{df}/_{dt}$ reflected the control data strongly, indicating that cholesterol had no major effect on tether formation. Although the data did not differ appreciably from control data in Figure 7.3, the two-barrier model, as described in length in Sections 2.3 and 6.4.4, could still be applied to the data to ascertain if there were any possible subtle differences. Figure 7.3 depicts individual fits to the various cholesterol concentrations and Figure 7.4 displays all data with appropriate fits together with the fit to control. The fits matched near the transition ($\sim 2x10^3$ pN/s) but diverged at low and high force ramps. The ordering of the fits reflected the pattern observed for the fit parameters stated in Table 7.1. From 25 mol% to 45 mol%, f_β raised in both the low and high force ramp regimes. Likewise, t_{off} lowered with increasing cholesterol concentration. This pattern was reflected in Figure 7.4 with the 25 mol% fit being greater than the 35 mol% fit, which in turn was greater than the 45 mol% fit at force ramps on the order of $\sim 10^2$ pN/s. At force ramps on the order of $\sim 10^3$ pN/s, the trend reversed. Interestingly, the fit parameters for 35 mol% were similar to control, reflecting the similar fit displayed in Figure 7.4.

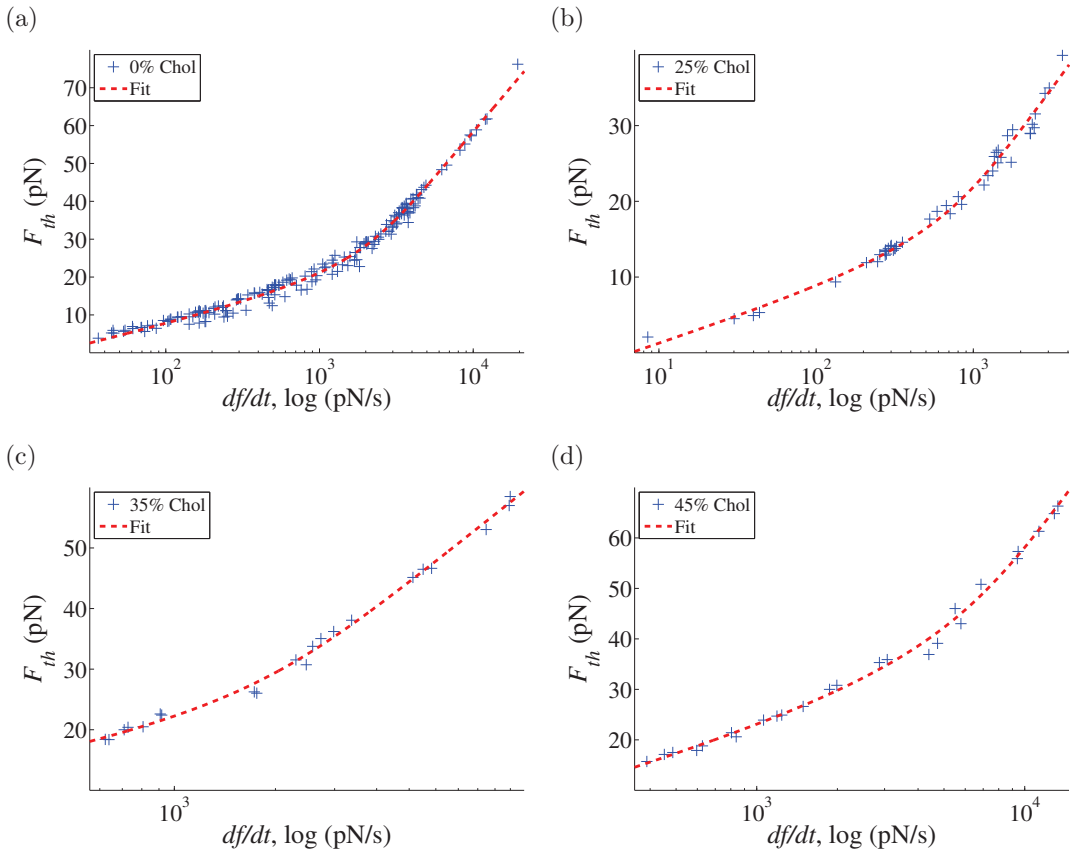

Figure 7.3 : Examination of the individual modifications seen in Figure 7.4 for the effect of varying cholesterol concentration on the relation between F_{th} and $^{df}/_{dt}$. (a) The control system for the cholesterol studies with 5 mol% biotinylated SOPC vesicles (blue crosses) with the two-barrier model fit (red dashed line). (b) Effect of the addition of 25 mol% cholesterol (N = 47, 7 vesicles) to the membrane. (c) 35 mol% (N = 22, 7 vesicles) cholesterol. (d) 45 mol% cholesterol data (N = 26, 9 vesicles). Fit parameters for all cases are given in Table 7.1.

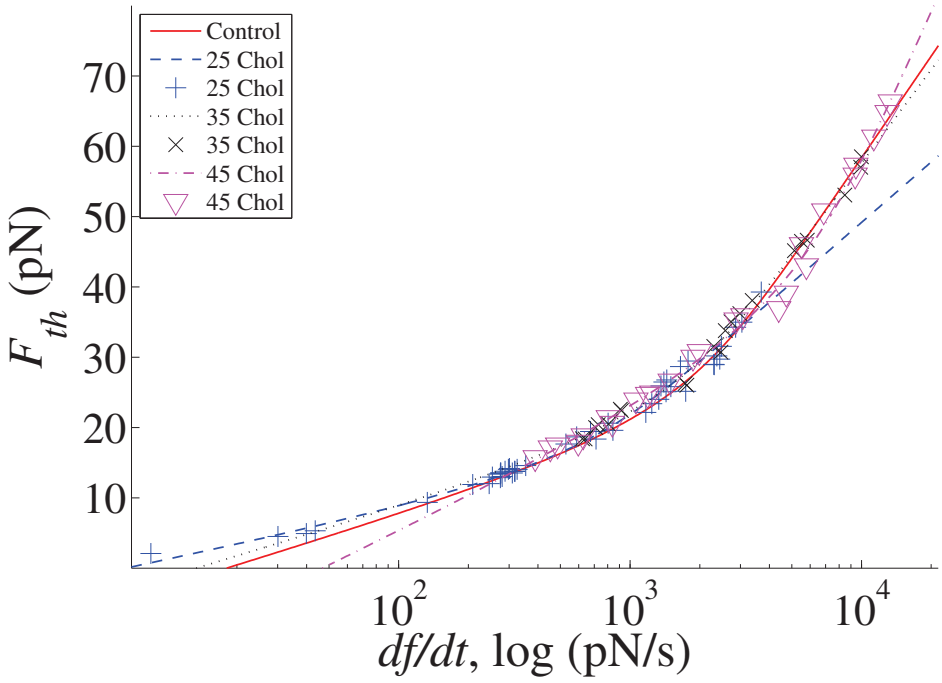

Figure 7.4 : A combined semilog plot of the cholesterol data (markers) with associated fits (lines) compared to control data (red solid line) with the fits extended to the full range of available data. The extended fits showed that as the cholesterol concentration increased (25 mol%, 35 mol%, to 45 mol%), the fits decreased at low force ramp but the fits increased at high force ramp. The control data, with 0 mol% cholesterol, fell between 35 mol% and 45 mol%. Fit parameters for all cases are given in Table 7.1.

Table 7.1 : Values to the fits of data presented in Figure 7.3. The fit parameters are displayed graphically in Figure 7.5. x_β was determined by $^{k_B T}/_{f_\beta} \approx {}^{4.1\,\mathrm{pN\cdot nm}}/_{f_\beta}$.

[Chol] (mol%)	$f_{\beta,1}$ (pN)	$x_{\beta,1}$ (nm)	$t_{off,1}$ (ms)	$f_{\beta,2}$ (pN)	$x_{\beta,2}$ (nm)	$t_{off,2}$ (ms)	Transition ($^{\mathrm{pN}}/_{\mathrm{s}}$)
0	4.3 ± 0.2	0.95 ± 0.04	230 ± 12	20.9 ± 1.3	0.20 ± 0.01	34 ± 2	760
25	3.0 ± 0.2	1.4 ± 0.1	430 ± 36	12.4 ± 1.2	0.33 ± 0.3	65 ± 9	270
35	4.2 ± 1.1	0.97 ± 0.24	310 ± 240	19.2 ± 1.9	0.21 ± 0.02	39 ± 6	690
45	6.9 ± 0.7	0.60 ± 0.06	140 ± 20	32.3 ± 7.7	0.13 ± 0.03	19 ± 4	2300

By examining the individual parameters (Figure 7.5), it was apparent that the trends observed were at most suggestive of subtle effects from cholesterol on the two-barrier energy landscape of tether formation. In order to ascertain if the noted trends do in fact occur, more data at the extremes of low and high force ramp regimes must be obtained to solidify the model fits. If the variation in fit parameters do hold up, the changes may be explained by the complicated phase state of the membrane caused by the increase in lipid packing parameter due to cholesterol. At 25 mol% and 35 mol% cholesterol, the vesicles might have existed in an unmixed liquid ordered-disordered phase (Veatch and Keller saw unmixed liquid:liquid coexistence for similar lipid systems at these concentrations [20]). Traversing the phase regime could explain the difference in behavior from 0 mol% to 25 mol% as opposed as that seen from 25 mol% to 45 mol%. Furthermore, the presence of a more packed membrane at high concentrations may explain the paucity of tethers observed at low force ramps; the greater cohesion and higher fluidity of the membrane [35, 107, 110] was able to withstand tether formation and respond within the time scales set by the low force ramps. A dependence of tether formation on the presence of different lipid phases, especially through lipid rafts—local regions of the membrane with significantly greater cholesterol concentration that are believed to influence membrane receptors [22] and membrane fusion [19], would be intriguing to the biological community, particularly concerning the applicability of the dependence to tether formation between white blood cells and blood vessel walls. While the trends observed with the presence of

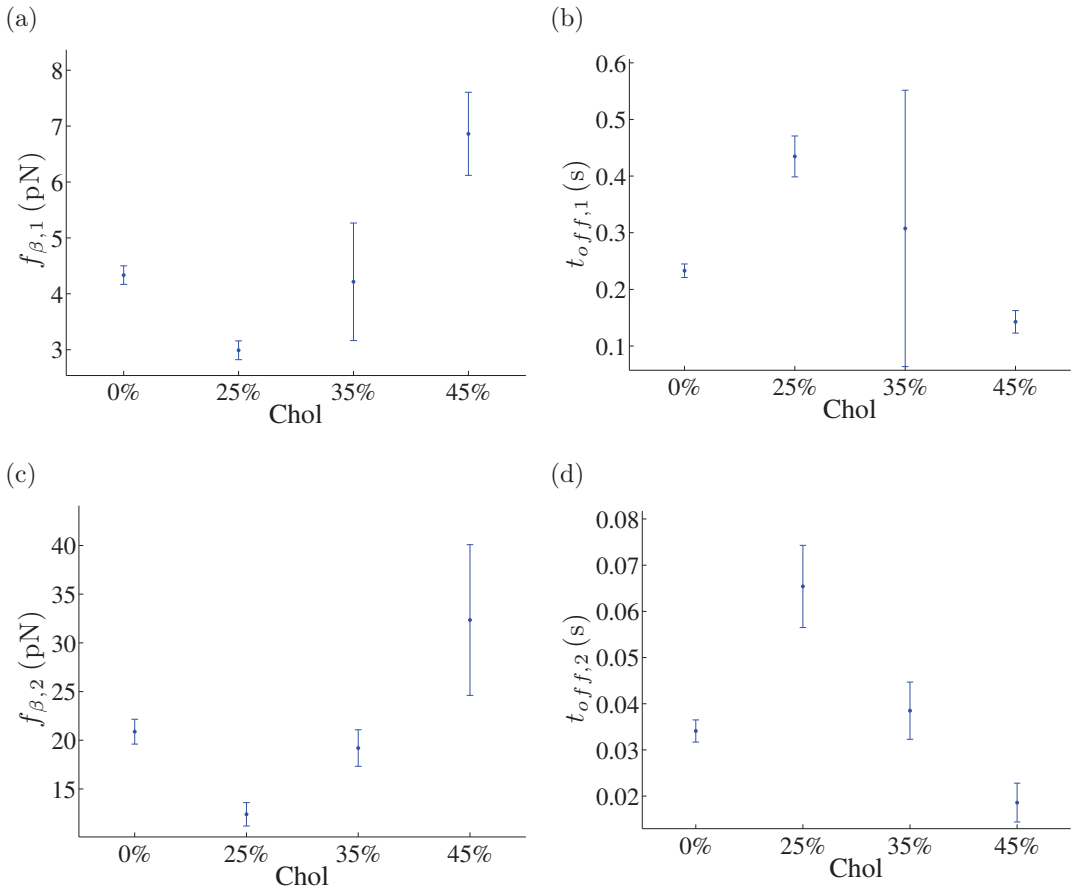

Figure 7.5 : Graphical representation of the fit values presented in Table 7.1. (a) $f_{\beta,1}$ lowered significantly from 0 mol% to 25 mol% cholesterol but augmented with cholesterol otherwise. (b) Reversing the trend seen in (a), $t_{off,1}$ grew from 0 mol% to 25 mol%, only to monotonically decrease thereafter. (c) Mirroring $f_{\beta,1}$, $f_{\beta,2}$ also increased from 25 mol% to 45 mol%. 25 mol% and 35 mol% were lower than 0 mol% control though. (d) $t_{off,2}$ monotonically reduced from 25 mol% to 45 mol% cholesterol after an initial rise from 0 mol% to 25 mol%. The relatively larger errors observed at 35 mol% was likely due to the fewer number of tethers obtained.

cholesterol in the SOPC vesicle are suggestive and could be interesting to a wide variety of biological fields, much more data, particularly away from the transition regime, must be obtain to substantiate any strong claims.

Interestingly, there might have been a force ramp range ($\lesssim 200\,\mathrm{pN/s}$) at which higher cholesterol tethers (35 mol% and 45 mol%) did not form, indicating a mechanism that affected tether formation that the two-barrier model failed to take into account.

It is natural to ask if there was a bias in the number of attempts to pull tethers at low ramp rates for various cholesterol concentrations. For the 0 mol%, 25 mol%, 35 mol%, and 45 mol% samples, there were 170, 47, 22, and 26 successful attempts to pull tethers. If we were to assume that the number of tethers pulled per attempt is independent of cholesterol, the successful pull rate from the 0 mol% data at low force ramp range (38 tethers, 22 % success) would predict 11, 5, and 6 tethers to form at low force ramps for 25 mol%, 35 mol%, and 45 mol% respectively. Additionally, all tether experiments started $\sim 70\,\mu$m away from the wire, where the expected force ramp would be low. As such, a large number of attempts were made to form tethers at the low range. Mere presence of cholesterol did not induce such behavior, however; at 25 mol%, tethers were found to form at even lower force ramps than the control. While this intriguing observation might have been a result of cholesterol on membrane behavior, it was not clear what this mechanism might have been and could simply have been a result of too few attempts at tether formation.

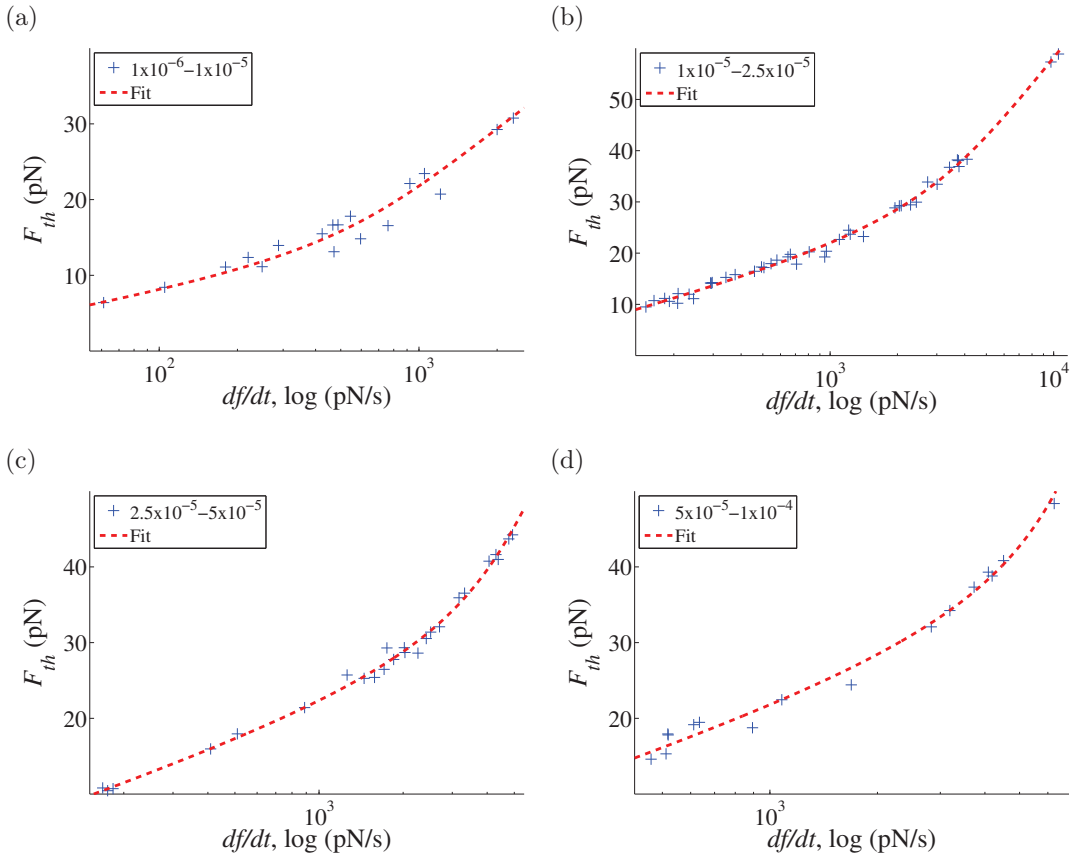

Figure 7.6 : The separated effects of varying tension on the relationship between F_{th} and $^{df}/_{dt}$ for Figure 7.7. (a) Tethering events with tensions ranging from $1x10^{-6} - 1x10^{-5}$ N/m (19 tethers from 6 vesicles). (b) Data for tensions ranging from $1x10^{-5} - 2.5x10^{-5}$ N/m (43 tethers from 7 vesicles). (c) $2.5x10^{-5} - 5x10^{-5}$ N/m tension data (26 tethers from 6 vesicles) (d) $5x10^{-5} - 1x10^{-4}$ N/m data (17 tethers from 4 vesicles).

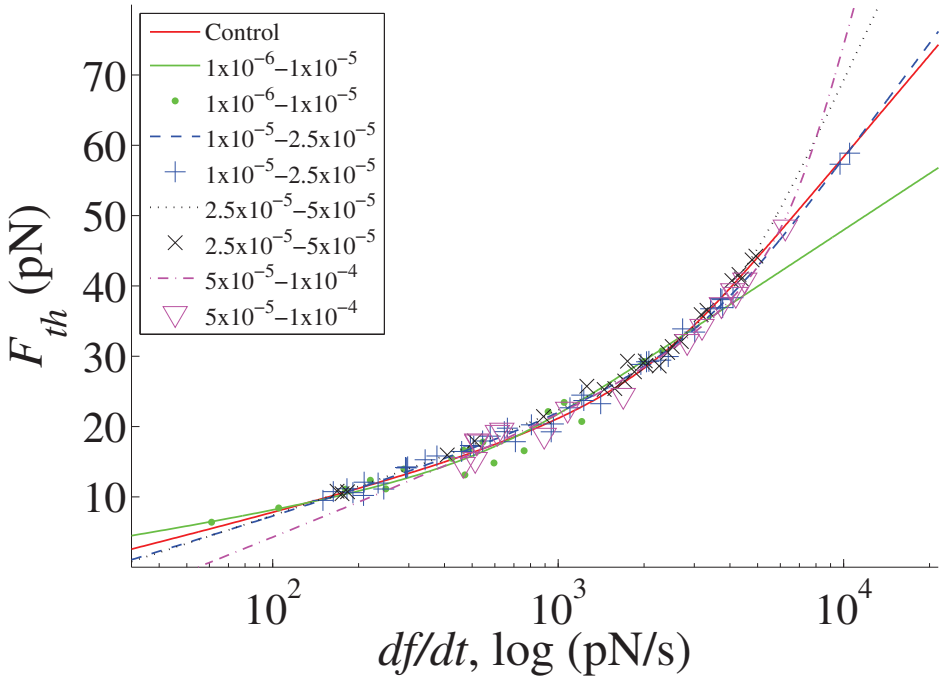

Figure 7.7 : A combined semilog plot of the tension data (markers) with associated fits compared to control data (red solid line). The two-barrier model fits (lines) imply a similar behavior as seen for the cholesterol study: increasing tension might have led to reduced force thresholds at low force ramps ($\sim 10^2$ pN/s) but higher force thresholds at high force ramps ($\sim 10^4$ pN/s). Much like the cholesterol studies, however, more data at both extremes in force ramp are needed to substantiate the implied dependence of tension on observed force thresholds given the subtle differences in data in the transition regime. Pressures in the legend are in units of N/m. Fit parameters for all cases are given in Table 7.2.

7.3.2 Tension

Many aspects of membrane mechanics, including tether behavior after being formed (Section 2.2.5), depend upon tension [12, 13, 31, 33, 41, 52]. To study the possible effects the tension τ of a vesicle might have had on the force threshold-force rate relationship, τ was varied from $1x10^{-6}$ N/m to $1x10^{-4}$ N/m* and the resulting F_{th} versus df/dt plots analyzed (see Figure 7.6). As seen in Figure 7.7, the connection between the observed force threshold and the applied force ramp did not significantly vary. The two-barrier model developed in Section 6.4.4 could be applied to determine if any understated patterns arose. Even though the data did not appear distinguishable in Figure 7.7, particularly in the transition regime, the deviation of the fit lines at the extremes of the force ramp range implies that there may be subtle differences. More data at these extremes would establish, instead of merely suggest, the validity of the variation depicted. Nonetheless, we will examine what trends we have observed.

Tension appeared to behave comparably to cholesterol, as can be seen in Figure 7.8. Like the increase of f_β with higher cholesterol concentrations (once above control), f_β rose monotonically by 2-3 fold as τ increased from $\sim 10^{-6}$ N/m (1 in Figure 7.8) to $\sim 1x10^{-4}$ N/m (4 in Figure 7.8, with values given in Table 7.2). f_β on the highest tension of $\lesssim 1x10^{-4}$ N/m had very large error for the high force ramp regime, indicating that at highest tension, the force threshold-force ramp behavior might be

*The tension study was conducted before the humidity and solution chambers detailed in Section 6.3 were constructed and the neutral pressure stabilized. Through multiple measurements of the neutral pressure, the neutral pressure at any time was extrapolated with errors no more than 10% expected.

Table 7.2 : Values to the fits of data presented in Figure 7.6. All errors are standard deviations. x_β was determined by ${k_B T}/{f_\beta} \approx {4.1\,\mathrm{pN{\cdot}nm}}/{f_\beta}$.

τ $({\mathrm{N}}/{\mathrm{m}})$	$f_{\beta,1}$ (pN)	$x_{\beta,1}$ (nm)	$t_{off,1}$ (ms)	$f_{\beta,2}$ (pN)	$x_{\beta,1}$ (nm)	$t_{off,2}$ (ms)	Transition $({\mathrm{pN}}/{\mathrm{s}})$
$1x10^{-6} - 1x10^{-5}$	2.9 ± 1.0	1.5 ± 0.5	380 ± 230	12 ± 4	0.35 ± 0.12	73 ± 34	200
$1x10^{-5} - 2.5x10^{-5}$	5.2 ± 0.4	0.79 ± 0.05	190 ± 16	24 ± 3	0.17 ± 0.02	27 ± 4	1100
$2.5x10^{-5} - 5x10^{-5}$	5.6 ± 0.5	0.73 ± 0.07	200 ± 16	37 ± 20	0.11 ± 0.06	24 ± 3	1600
$5x10^{-5} - 1x10^{-4}$	6.9 ± 2.4	0.60 ± 0.20	130 ± 40	65 ± 200	0.06 ± 0.20	20 ± 15	2600

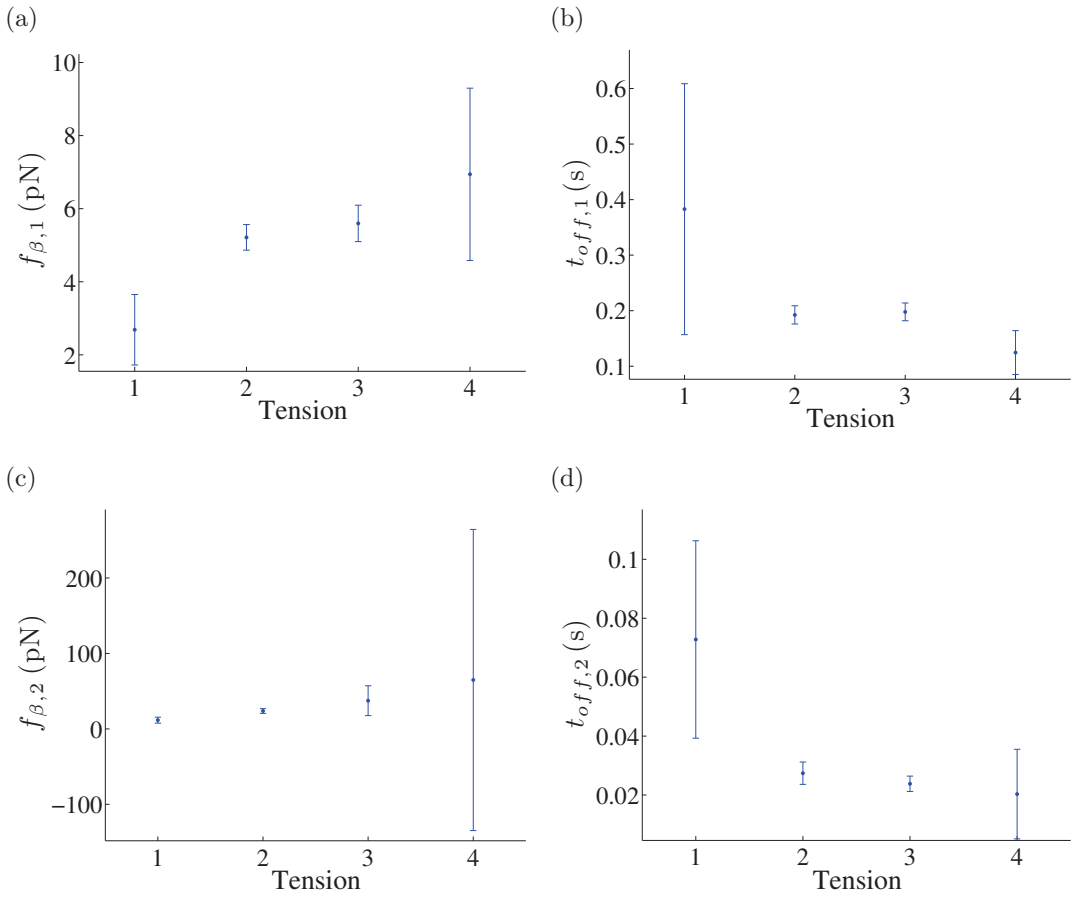

Figure 7.8 : Graphical representation of the fit values presented in Table 7.2. (a) $f_{\beta,1}$ appeared to rise with increasing tension from 1 ($1x10^{-6} - 1x10^{-5}$ N/m) to 4 ($5x10^{-5} - 1x10^{-4}$ N/m) with two similar intermediate values at 2 ($1x10^{-5} - 2.5x10^{-5}$ N/m) and 3 ($2.5x10^{-5} - 5x10^{-5}$ N/m). (b) With an increase in $f_{\beta,1}$, $t_{off,1}$ correspondingly lowered. (c) While the error at 4 was large for $f_{\beta,2}$, the other values increased monotonically (Table 7.2). The large error at 4 possibly indicated that tether formation was not well modeled by a two-barrier model at high tension. (d) $t_{off,2}$ monotonically reduced from 1 to 4 implying a possible reduction in one of the energy barriers at high force ramps.

better modeled by a single energy barrier, as opposed to two barriers. t_{off} also lowered as tension rose, much as it lowered for increasing cholesterol (except the control). t_{off} decreased by about a factor of 3 in both the low and high force ramp regimes, implying that increased tension may also reduce energy energy barrier heights. To be certain of any suggested relationship, however, more data at the low and high force ramp regimes are needed to reduce observed uncertainties, particularly in $f_{\beta,2}$ at high tension and in t_{off} at low tension. If the trends do hold up, an interesting analogy between tension and cholesterol might be asserted: an increase in cholesterol concentration increases packing within the membrane and an intensification of tension smooths thermal fluctuations, reducing membrane disorder. This hypothesis could be tested by controllably reducing the temperature of the MFT-aspirator device using a thermoelectric or water cooling to just above freezing. If the hypothesis holds, the reduced thermal fluctuations should lead to the removal of one of the barriers in the energy landscape of tether formation. The effect would be subtle, however, as temperature was not observed to greatly affect tether formation at room temperature and above (see Figure 6.6a).

The subtle influence of tension could also be investigated by incorporating salicylate into the membrane. Salicylate is known to disrupt the membrane [31] and should make it easier for tethers to form, resulting in a decrease in t_{off}. Further, the barrier dependent on tension would dominate at lower tensions as other, lower energy processes would also be disrupted, resulting in a decrease in energy barrier

height. Given the very small effect of tension suggested by the previous studies, large concentrations of salicylate of up to 5 mM or 10 mM should be used to obtain the largest possible changes in membrane properties.

7.3.3 Biotin Concentration

The number of receptor-ligand bonds in the adhesion between the membrane and bead is also expected to modulate tether response [74, 89][†]. To investigate the possible functional dependence on biotin concentration, vesicles containing 1 mol% biotinylated DHPE lipids were compared to those containing 5 mol% biotinylated lipids and plotted in Figure 7.9a with relevant fit parameters given by Table 7.3. While both the 1 mol% and 5 mol% biotinylated lipid data showed the presence of two force ramp regimes (Figure 7.9), indicating a two-barrier energy landscape, the fit for 1 mol% data altered much more between regimes. For all measured tether formation events, the observed threshold forces for 1 mol% biotin were lower than 5 mol%. However, at higher force ramps ($\gtrsim 2x10^3$ pN/s), the relation, according to the model fits, was expected to reverse. Investigating why this transition is suggested might illuminate what mechanisms lead to the two-barrier model, but it is currently unclear what these mechanisms might be.

Even with the intriguing behavior at high force ramps, the increase in t_{off} in both regimes (Table 7.3 and Figure 7.10) suggested that the energy barriers to tether

[†]The biotin study was conducted before the humidity and solution chambers detailed in Section 6.3 were constructed but extrapolated values of the neutral pressure were not expected to exceed 10%.

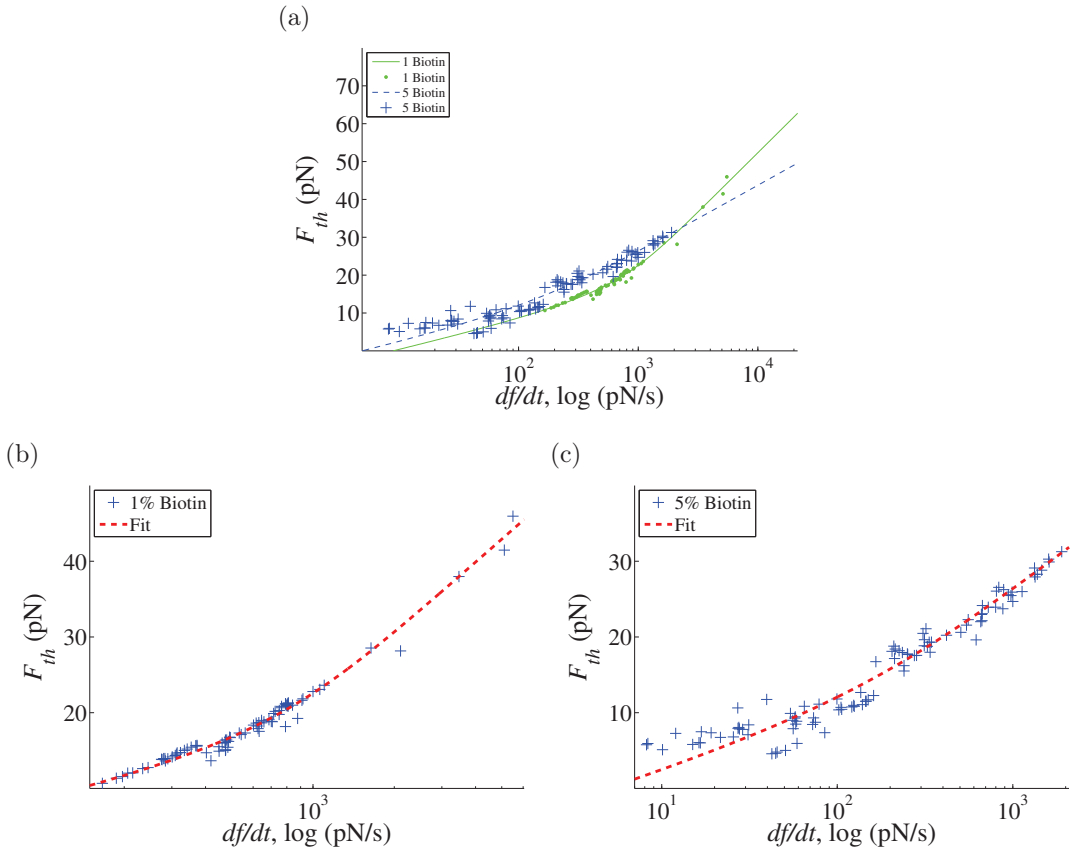

Figure 7.9 : The effect of biotinylated DHPE concentration on the relation between F_{th} and $^{df}/_{dt}$. (a) The observed force thresholds (markers) for 1 mol% biotinylated lipid (green) were lower than for 5 mol% (blue) until higher force ramps ($\sim 10^3$ $^{\mathrm{pN}}/_{\mathrm{s}}$) at which point the force threshold were higher than those predicted (lines) for 5 mol%. Using the two-barrier model, the change between the low and high force ramp regimes are greater for 1 mol% than for 5 mol%.(b) The 1 mol% biotin data. (c) The 5 mol% biotin was noisier than the 1 mol%. Both sets of data appeared to span only within the transition regime; however, both low and high force ramp regimes are present. The vesicles used in the biotin study were prepared from different stock than the vesicles used for the other studies in this chapter and so have slightly different values in fit parameters for 5 mol% biotin, as seen in Table 7.3.

Table 7.3 : Values to the fits of data presented in Figure 7.9. All errors are standard deviations. x_β was determined by ${k_B T}/{f_\beta} \approx {4.1\,\mathrm{pN{\cdot}nm}}/{f_\beta}$.

[Biotin] (mol%)	$f_{\beta,1}$ (pN)	$x_{\beta,1}$ (nm)	$t_{off,1}$ (ms)	$f_{\beta,2}$ (pN)	$x_{\beta,2}$ (nm)	$t_{off,2}$ (ms)	Transition (${\mathrm{pN}}/{\mathrm{s}}$)
1	3.3 ± 0.4	1.2 ± 0.2	350 ± 110	14 ± 1	0.30 ± 0.02	63 ± 8	290
5	3.2 ± 1.2	1.3 ± 0.5	550 ± 140	7.7 ± 2.3	0.5 ± 0.2	230 ± 190	57

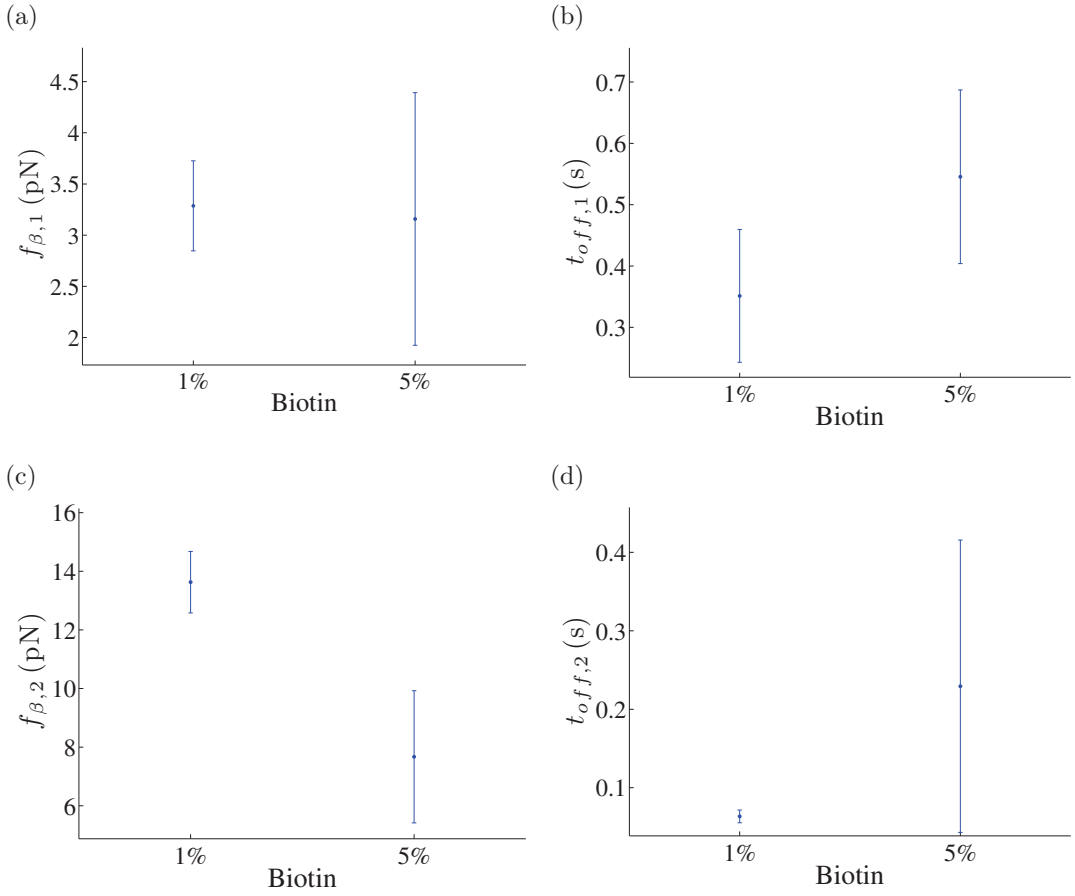

Figure 7.10 : Graphical representation of the fit values presented in Table 7.3. (a) No significant difference in $f_{\beta,1}$ between 1 mol% and 5 mol% biotinylated lipid was present. (b) $t_{off,1}$ slightly grew with greater biotin concentration. (c) Unlike $f_{\beta,1}$, $f_{\beta,2}$ reduced from 1 mol% to 5 mol%; it lowered by 6 pN. (d) $t_{off,2}$ augmented from 1 mol% to 5 mol%, but the large error at 5 mol% reduced the significance of any change.

formation might have increased with a greater concentration of binding sites. Contributions of the lipid DHPE itself, which has a slightly shorter tail length (17 carbons instead of 18) and no carbon double bonds in the tail, was not expected to contribute significantly to the change in tether formation as the shorter tail length was countered by the greater saturation of carbon bonds. If the relation were to hold, it would confirm the previously seen observations that the number of receptor-ligand bonds, corresponding to contact area, influence force response of membranes [74, 89]. The similarity of $f_{\beta,1}$ but distinguishability of $f_{\beta,2}$ at the two concentrations implied that tether formation is less sensitive to contact area at low force ramps than at high force ramps. However, until tether formation events at high force ramps ($> 10^4$ pN/s) for the 5 mol% biotin and at low force ramps ($< 10^2$ pN/s) for the 1 mol% biotin are obtained, such an implication is uncertain.

It is not demonstrated above, but the stability of the lipids was particularly important for biotin concentration studies. When attempting to reproduce the above effect with stock solutions derived from another batch of Biotin-X DHPE and SOPC, no variation was found between SOPC vesicles containing 0.5 mol%, 8 mol%, and 15 mol% Biotin-X DHPE. It should be noted though that few vesicles formed and fewer than 10 tethers were able to be formed from any of the three batches, even after varying PBS concentration (which affect biotin-streptavidin binding) and substantial cleaning of all components of the system. Furthermore, when comparing the 5 mol% biotinylated lipid assay presented in Figure 6.4 to that in Figure 7.9, there

is significant difference in magnitude ($\sim 25\%$) but not shape between the two. Since the stock for the vesicles used in this study were made a few weeks after aliquoting the original stock, the concentrations in this study were expected to be higher than reported. The relative concentration between the 1 mol% and 5 mol% biotinylated lipids were, however, correct. Reproduction of the interesting dependence on receptor-ligand concentration could illuminate a strong dependence of tether formation on contact area of the membrane involved. However, great care must be taken that all supplies are less than a few weeks old and were aliquoted into appropriate stock solutions immediately upon opening of the sample.

7.3.4 SOPS

So far we have examined the effects of cholesterol, tension, and biotin concentration on the relationship between observed tether formation force and applied force ramp. The influence of cholesterol and tension were suggested to be subtle. Biotin concentration had a significant effect on the form of the threshold force-force ramp relationship, but reproducibility from one stock solution of lipids to another was extremely limited. As a last study, we investigated how lipid headgroup structure might impact tether formation; we incorporated 10 mol% of of 1-stearoyl-2-oleoyl-*sn*-glycero-3-phospho-L-serine (SOPS), a charged lipid, into the membrane. Small amounts of SOPS stabilize vesicles, but upon the incorporation of 10 mol% SOPS into the membrane we observed reduction in not only the number of vesicles formed but also the effectiveness of bind-

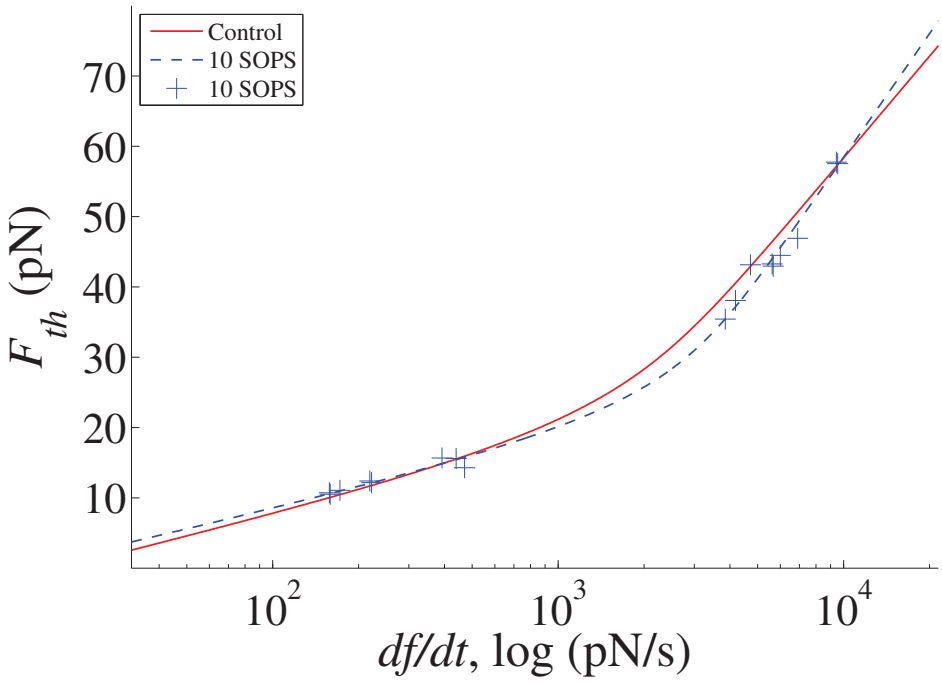

Figure 7.11 : The influence of SOPS on the force threshold-force ramp relationship. The effect of 10 mol% SOPS (blue markers, 17 tethers from 6 vesicles) on the relation between F_{th} and $^{df}/_{dt}$. While it was difficult to obtain tethers and data, a two regime system was evident. The two-barrier fit for 10 mol% SOPS (blue dashed line) followed the control data (red solid line) well in the low force ramp regime, and slightly less so in the high force ramp regime.

Table 7.4 : Values to the fits of data presented in Figure 7.11. All errors are standard deviations. x_β was determined by $k_BT/f_\beta \approx 4.1\,\mathrm{pN{\cdot}nm}/f_\beta$. These values are displayed graphically in Figure 7.12.

[SOPS] (mol%)	$f_{\beta,1}$ (pN)	$x_{\beta,1}$ (nm)	$t_{off,1}$ (ms)	$f_{\beta,2}$ (pN)	$x_{\beta,2}$ (nm)	$t_{off,2}$ (ms)	Transition (pN/s)
0	4.3 ± 0.2	0.95 ± 0.04	230 ± 12	20.9 ± 1.3	0.20 ± 0.01	34 ± 2	760
10	4.0 ± 0.5	1.0 ± 0.1	310 ± 70	25 ± 4	0.16 ± 0.03	25 ± 4	2400

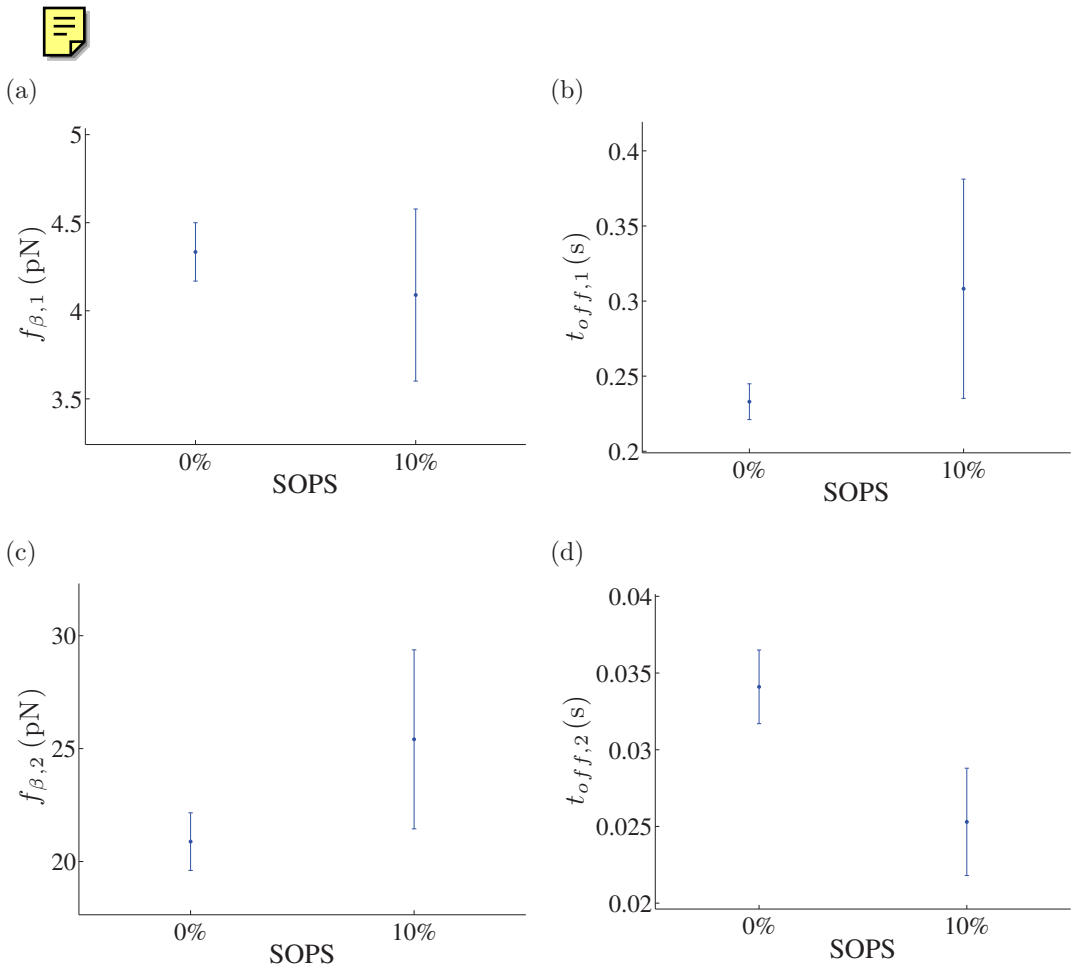

Figure 7.12 : Graphical representation of the fit values presented in Table 7.4. (a) No significant difference in $f_{\beta,1}$ between 1 mol% and 10 mol% SOPS was observed. (b) $t_{off,1}$ grew slightly with greater SOPS concentration. (c) The magnitude of $f_{\beta,2}$ raised from 1 mol% to 10 mol%; it augmented by $\sim$ 5 pN. (d) $t_{off,2}$ lowered with higher SOPS concentration.

ing between the biotin and streptavidin groups. Nonetheless, sufficient data was obtained to distinguish the existence of two regimes (see Figure 7.11). Considering the difficulty in forming vesicles with high concentrations of SOPS, the two-barrier fit to 10 mol% SOPS mirrored that of control data, with a slightly increased transition force ramp. As seen in Table 7.4, an increase of SOPS concentration from 0 mol% to 10 mol% led to no statistically significant change in $f_{\beta,1}$, and only a slight augmentation of $f_{\beta,2}$. Unlike the previous studies, which showed consistent behavior in t_{off} for both regimes, SOPS seemed to raise $t_{off,1}$ slightly with more SOPS but decrease $t_{off,2}$. This suggested effect may be exacerbated by adjusting the pH of the system, changing the charge state of the phosphatidylserine. Care must be taken to distinguish between the effect of pH on the mechanical properties of the membrane as the mechanical properties, such as bending elasticity, of phosphatidylcholine are also known to be influenced by pH [33]. Likewise, altering the strength of electrostatic screening may affect streptavidin-biotin binding. If the different effects are discerned, any electrostatic interactions that impact tether formation might be evaluated.

7.4 Improvements

As the threshold force depends upon the force ramp in a logarithmic-like manner, it is very insensitive to modifications in the membrane. Conversely, due to the exponentials of the two-barrier model, the fitting parameters are sensitive to the regime and quantity of the data collected. Using lipid stocks that are no more than a few weeks

old and have been properly aliquoted will ensure that data is still discernible between various assays, even with only slight differences in magnitude. Taking large data sets may not obtain the range in force rates desired to ensure an extremely accurate fit, but it does confirm reproducibility of studies. Pains should be taken to study as wide a range of applied force ramps as possible.

7.5 Summary

In this chapter, we investigated not only how cholesterol, but also tension, biotinylated lipids, and phosphatidylserine affected the behavior of the relationship between the force threshold of tether formation and the rate of applied force. We found that while cholesterol, tension, and phosphatidylserine influenced the system only subtly, the similarity in trends between cholesterol and tension are suggestive of similar mechanisms on the energy landscape of tether formation and an opposing trend in phosphatidylserine implies a possible electrostatic influence. The concentration of biotinylated lipids showed the greatest change on observed force threshold behavior, but was difficult to reproduce from one stock to the next, due to sensitivity of lipids to oxidation. The preliminary trends detailed may be substantiated by extending the range of data away from the transition point, where only one energy barrier dominates. The mechanisms dominating the energy landscape may also be further investigated by adjusting solution pH, lowering temperature, or adding salicylate. Finally, the joint magnetic force transducer-microaspirator system could be extended to

cells undergoing tether formation. Using the force threshold-force ramp relationship, the mechanics in the more complicated cellular system could be probed.

Chapter 8

Concluding Remarks and Future Work

When I examine myself and my methods of thought, I come to the conclusion that the gift of fantasy has meant more to me than any talent for abstract, positive thinking. - Albert Einstein [111]

THIS thesis details the fabrication of a joint magnetic force transducer-microaspirator. The magnetic force transducer-microaspirator system was designed to apply point forces to membranes using a well-controlled and well-characterized magnetic field. The well-controlled fields enabled force rates from 1 to $10^4 \mathrm{pN/s}$ and force pulses to be applied to membranes. Using the applied forces, a strong dependence of the threshold force for tether formation on the applied force ramp was discovered. To understand such dependence, we developed a two-barrier energetic model and applied it to the tether system under various perturbations: cholesterol concentration, tension, biotin-site concentration, phosphatidylserine concentration. Cholesterol, tension, and phosphatidylserine modified the system subtly, and trends were found that indicate cholesterol and tension may have modified the tether energy landscape in similar fashions. Both cholesterol and tension may have provided greater order to the system, but more studies at the low and high force ramp regime are needed to confirm the trends noted. Phosphatidylserine responded distinctly between the low and high force ramp regimes. The strongest change was seen with biotin-site concentration,

with higher force thresholds observed for higher concentration of biotin. The stability of the lipid system, however, precluded verification with another stock solution of lipids. While many of these studies still require verification, the implied trends indicated that the energy landscape of tether formation could be mapped out and the mechanisms governing tether formation determined. In addition to force threshold dynamics, the drag between bilayers was estimated to be $b = 1.1 \pm 0.6x10^{9}\,{}^{\mathrm{N\cdot s}}/_{\mathrm{m}^3}$. Finally, using the MFT in combination with a thorough COMSOL model led to the determination of the areal expansion of SOPC vesicles ($1.7 \pm 0.4x10^{-3}\,\mathrm{K}^{-1}$) due to temperature change.

This now-established technique may be used in the future to further study the influence of cholesterol on tether formation from cell membranes by exploring system response at extremely low force rates, where low energy barriers would become apparent. Further studies may also be conducted that further examine how other modifications to the membrane, such as membrane disruptors like salicylate, influence tether formation dynamics. Finally, a detailed examination of the response of force threshold to force ramp over many cholesterol concentrations would allow a comprehensive study of phase regimes on tether formation.

In order to study the energetics of tether formation off of cell membranes or cell blebs (portions of the cell membrane that have separated from the cell), the forces that magnetic beads in the magnetic force transducer device exerts must be raised by at least an order of magnitude [13]. Higher volume fraction of magnetic material in the

beads or volume of each bead raises the force. Furthermore, by using paramagnetic beads with a large consistent external magnetic field, large uniform forces far from the wire may be established. These considerations would drive any revisions of the device.

We have detailed the fabrication of a magnetic force transducer-microaspirator system. This new system was used to measure, for the first time, the dependence of the observed force threshold of tether formation on the applied force ramp. This dependence was modeled by a proposed two-barrier energy landscape. Finally, possible means to influence the relationship between force threshold and force ramp were investigated with cholesterol, tension, biotinylated lipid concentration, and SOPS; several trends were suggested but additional studies are required to verify them.

Bibliography

[1] *Ignatius Catholic Study Bible: New Testament.* Ignatius Press, 2010. v

[2] Brainy Quote, "Niccolo machiavelli quotes." Accessed Jul 24, 2011. `http://www.brainyquote.com/quotes/quotes/n/niccolomac131418.html`. 1

[3] P. G. de Gennes, "Soft matter.," *Science (New York, NY)*, vol. 256, pp. 495–497, Apr. 1992. 1, 12

[4] D. Schmidtke and S. Diamond, "Direct observation of membrane tethers formed during neutrophil attachment to platelets or P-selectin under physiological flow," *Journal of Cell Biology*, vol. 149, no. 3, pp. 719–729, 2000. 1, 106

[5] M. Furlow and S. Diamond, "Interplay between membrane cholesterol and ethanol differentially regulates neutrophil tether mechanics and rolling dynamics," *Biorheology*, vol. 48, no. 1, pp. 49–64, 2011. 1, 106

[6] B. Onfelt, S. Nedvetzki, R. K. P. Benninger, M. A. Purbhoo, S. Sowinski, A. N. Hume, M. C. Seabra, M. A. A. Neil, P. M. W. French, and D. M. Davis, "Structurally distinct membrane nanotubes between human macrophages support long-distance vesicular traffic or surfing of bacteria.," *Journal of immunology (Baltimore, Md. : 1950)*, vol. 177, pp. 8476–8483, Dec. 2006. 1, 106

[7] H.-H. Gerdes and R. N. Carvalho, "Intercellular transfer mediated by tunneling

nanotubes.," *Current opinion in cell biology*, vol. 20, pp. 470–475, Aug. 2008. 1, 106

[8] A. Chauveau, A. Aucher, P. Eissmann, E. Vivier, and D. M. Davis, "Membrane nanotubes facilitate long-distance interactions between natural killer cells and target cells.," *Proceedings of the National Academy of Sciences of the United States of America*, vol. 107, pp. 5545–5550, Mar. 2010. 1, 106

[9] G. Girdhar and J.-Y. Shao, "Simultaneous tether extraction from endothelial cells and leukocytes: observation, mechanics, and significance," *Biophysical Journal*, vol. 93, pp. 4041–4052, Dec. 2007. 1

[10] H. Lee, A. M. Purdon, and R. M. Westervelt, "Manipulation of biological cells using a microelectromagnet matrix," *Applied Physics Letters*, vol. 85, no. 6, pp. 1063–1065, 2004. 2, 51, 82, 95

[11] J. Fisher, J. Cribb, K. Desai, L. Vicci, B. Wilde, K. Keller, R. Taylor, J. Haase, K. Bloom, E. O'Brien, and R. Superfine, "Thin-foil magnetic force system for high-numerical-aperture microscopy," *Rev Sci Instrum*, vol. 77, p. 023702, Jan 2006. 2, 49, 81, 82

[12] R. M. Raphael and R. E. Waugh, "Accelerated interleaflet transport of phosphatidylcholine molecules in membranes under deformation," *Biophysical Journal*, vol. 71, pp. 1374–1388, sep 1996. 2, 81, 95, 102, 107, 132, 133, 155

[13] Y. Chen, D.-K. Yao, and J. Y. Shao, "The constitutive equation for membrane tether extraction," *Annals of biomedical engineering*, vol. 38, no. 12, pp. 3756–3765, 2010. 3, 34, 107, 119, 132, 155, 172

[14] E. Evans, V. Heinrich, F. Ludwig, and W. Rawicz, "Dynamic tension spectroscopy and strength of biomembranes," *Biophysical Journal*, vol. 85, pp. 2342–2350, Oct. 2003. 3, 41, 123, 128, 129, 134

[15] Brainy Quote, "Hermann von helmholtz quotes." Accessed Jul 9, 2011. `http://www.brainyquote.com/quotes/authors/h/hermann_von_helmholtz.html`. 6

[16] B. Alberts, A. Johnson, J. Lewis, M. Raff, K. Roberts, and P. Walter, *Molecular Biology of the Cell, Fourth Edition*. Garland Science, 4 ed., Mar. 2002. 7, 10

[17] H. T. McMahon and J. L. Gallop, "Membrane curvature and mechanisms of dynamic cell membrane remodelling.," *Nature*, vol. 438, pp. 590–596, Dec. 2005. 7

[18] K. Jacobson, O. Mouritsen, and R. Anderson, "Lipid rafts: At a crossroad between cell biology and physics," *Nature cell biology*, vol. 9, no. 1, pp. 7–14, 2007. 7

[19] G. Van Meer, D. Voelker, and G. Feigenson, "Membrane lipids: Where they are and how they behave," *Nature Reviews Molecular Cell Biology*, vol. 9, no. 2, pp. 112–124, 2008. 8, 9, 131, 137, 150

[20] S. L. Veatch and S. L. Keller, "Organization in lipid membranes containing cholesterol," *Physical Review Letters*, vol. 89, no. 26, pp. 268101/1–268101/4, 2002. 10, 19, 137, 144, 150

[21] S. L. Veatch and S. L. Keller, "Separation of liquid phases in giant vesicles of ternary mixtures of phospholipids and cholesterol," *Biophysical Journal*, vol. 85, pp. 3074–3083, Nov. 2003. 10, 19, 144

[22] D. Lingwood and K. Simons, "Lipid rafts as a membrane-organizing principle.," *Science (New York, NY)*, vol. 327, pp. 46–50, Jan. 2010. 10, 150

[23] W.-J. Sun, S. Tristram-Nagle, R. M. Suter, and J. F. Nagle, "Structure of gel phase saturated lecithin bilayers: Temperature and chain length dependence," *Biophysical Journal*, vol. 71, pp. 885–891, Jan. 1996. 10

[24] J. N. Israelachvili, *Intermolecular and Surface Forces, Third Edition*. Academic Press, 2nd ed., Nov. 1994. 10, 18, 21

[25] E. A. Evans, "A new material concept for the red cell membrane.," *Biophysical Journal*, vol. 13, pp. 926–940, Sept. 1973. 12

[26] M. Bloom, E. Evans, and O. Mouritsen, "Physical properties of the fluid lipid-bilayer component of cell membranes: a perspective.," *Quarterly reviews of biophysics*, vol. 24, pp. 293–397, Aug. 1991. 13

[27] W. Helfrich and R. M. Servuss, "Undulations, Steric Interaction and Cohesion

of Fluid Membranes," *Il Nuovo Cimento Della Societa Italiana Di Fisica D*, vol. 3, no. 1, pp. 137–151, 1984. 13, 107

[28] S. Singer and G. Nicolson, "The fluid mosaic model of the structure of cell membranes," *Science (New York, NY)*, vol. 175, no. 4023, pp. 720–731, 1972. 13

[29] R. Waugh and E. A. Evans, "Thermoelasticity of red blood cell membrane," *Biophysical Journal*, vol. 26, pp. 115–131, apr 1979. 13, 26, 28, 98, 137

[30] D. H. Boal, *Mechanics of the cell*. Cambridge University Press, 1 ed., 2002. 13, 14, 16, 17, 23, 24, 25

[31] Y. Zhou and R. M. Raphael, "Effect of salicylate on the elasticity, bending stiffness, and strength of SOPC membranes," *Biophysical Journal*, vol. 89, pp. 1789–1801, Sept. 2005. 14, 17, 23, 24, 25, 28, 84, 98, 107, 110, 155, 158

[32] R. M. Hochmuth, H. C. Wiles, E. A. Evans, and J. T. McCown, "Extensional flow of erythrocyte membrane from cell body to elastic tether. II. Experiment," *Biophysical Journal*, vol. 39, pp. 83–89, jul 1982. 14, 81

[33] Y. Zhou and R. M. Raphael, "Solution pH alters mechanical and electrical properties of phosphatidylcholine membranes: relation between interfacial electrostatics, intramembrane potential, and bending elasticity.," *Biophysical Journal*, vol. 92, pp. 2451–2462, Apr. 2007. 14, 17, 84, 90, 110, 155, 168, 214

[34] R. Phillips, J. Kondev, and J. Theriot, *Physical Biology of the Cell*. Garland Science, 1 ed., Nov 2008. 14, 15, 17, 18, 19, 23, 26, 30, 31, 33

[35] J. Song and R. E. Waugh, "Bending rigidity of SOPC membranes containing cholesterol," *Biophysical Journal*, vol. 64, pp. 1967–1970, June 1993. 17, 137, 150

[36] E. Evans and W. Rawicz, "Entropy-driven tension and bending elasticity in condensed-fluid membranes," *Physical Review Letters*, vol. 64, pp. 2094–2097, Apr. 1990. 17, 25, 137

[37] A. Tian, B. R. Capraro, C. Esposito, and T. Baumgart, "Bending stiffness depends on curvature of ternary lipid mixture tubular membranes.," *Biophysical Journal*, vol. 97, pp. 1636–1646, Sept. 2009. 17

[38] W. Rawicz, K. C. Olbrich, T. McIntosh, D. Needham, and E. Evans, "Effect of chain length and unsaturation on elasticity of lipid bilayers.," *Biophysical Journal*, vol. 79, pp. 328–339, July 2000. 17, 25

[39] D. Marsh, "Lateral pressure profile, spontaneous curvature frustration, and the incorporation and conformation of proteins in membranes.," *Biophysical Journal*, vol. 93, pp. 3884–3899, Dec. 2007. 18, 20

[40] T. Baumgart, S. T. Hess, and W. W. Webb, "Imaging coexisting fluid domains in biomembrane models coupling curvature and line tension.," *Nature*, vol. 425, pp. 821–824, Oct. 2003. 19, 22, 146

[41] E. A. Evans and A. Yeung, "Hidden dynamics in rapid changes of bilayer shape," *Chemistry And Physics Of Lipids*, vol. 73, pp. 39–56, jan 1994. 19, 32, 33, 81, 95, 102, 107, 155

[42] E. A. Evans, "New membrane concept applied to the analysis of fluid shear- and micropipette-deformed red blood cells.," *Biophysical Journal*, vol. 13, pp. 941–954, Sept. 1973. 26

[43] H. Kramers, "Brownian motion in a field of force and the diffusion model of chemical reactions," *Physica*, vol. 7, no. 4, pp. 284–304, 1940. 34, 123, 128

[44] E. Evans, "Probing the relation between force–lifetime–and chemistry in single molecular bonds," *Annual review of biophysics and biomolecular structure*, vol. 30, pp. 105–128, 2001. 34, 36, 37, 38, 124, 125, 126, 127, 128, 129, 131, 134

[45] G. Bell, "Models for the specific adhesion of cells to cells. A theoretical framework for adhesion mediated by reversible bonds between cell surface molecules," *Science (New York, NY)*, vol. 200, no. 4342, pp. 618–627, 1978. 36, 123

[46] Quote Sea, "Michael faraday quotes." Accessed Jul 26, 2011. `http://www.quotesea.com/quote/iambusyjustnowagainonelectromagnetism`. 43

[47] F. H. C. Crick and A. F. W. Hughes, "The Physical Properties of Cytoplasm - a Study by Means of the Magnetic Particle Method. Part 1: Experimental," *Experimental Cell Research*, vol. 1, no. 1, pp. 37–80, 1950. 43, 44, 45

[48] T. Strick, J.-F. Allemand, D. Bensimon, A. Bensimon, and V. Croquette, "The elasticity of a single supercoiled DNA molecule," *Science (New York, NY)*, vol. 271, no. 5257, pp. 1835–1837, 1996. 44

[49] K. Yagi, "Mechanical and Colloidal Properties of Amoeba Protoplasm and Their Relations to Mechanism of Amoeboid Movement," *Comparative Biochemistry and Physiology*, vol. 3, no. 2, pp. 73–91, 1961. 45

[50] M. Sato, T. Z. Wong, D. T. Brown, and R. D. Allen, "Rheological properties of living cytoplasm: a preliminary investigation of squid axoplasm (Loligo pealei).," *Cell motility*, vol. 4, no. 1, pp. 7–23, 1984. 45

[51] N. Wang, J. P. Butler, and D. E. Ingber, "Mechanotransduction across the cell surface and through the cytoskeleton.," *Science (New York, NY)*, vol. 260, pp. 1124–1127, May 1993. 46

[52] V. Heinrich and R. E. Waugh, "A piconewton force transducer and its application to measurement of the bending stiffness of phospholipid membranes," *Annals of biomedical engineering*, vol. 24, pp. 595–605, jan 1996. 46, 81, 94, 155

[53] A. R. Bausch, F. Ziemann, A. A. Boulbitch, K. Jacobson, and E. Sackmann, "Local measurements of viscoelastic parameters of adherent cell surfaces by magnetic bead microrheometry," *Biophys J*, vol. 75, pp. 2038–49, Oct 1998. 47

[54] H. Huang, C. Dong, H.-S. Kwon, J. Sutin, R. D. Kamm, and P. So, "Three-Dimensional Cellular Deformation Analysis with a Two-Photon Magnetic Manipulator Workstation," *Biophysical Journal*, vol. 82, no. 4, pp. 2211–2223, 2002. 47

[55] B. G. Hosu, K. Jakab, P. Bánki, F. I. Tóth, and G. Forgacs, "Magnetic tweezers for intracellular applications," *Rev Sci Instrum*, vol. 74, p. 4158, Aug 2003. 47

[56] B. G. Hosu, M. Sun, F. Marga, M. Grandbois, and G. Forgacs, "Eukaryotic membrane tethers revisited using magnetic tweezers," *Phys Biol*, vol. 4, pp. 67–78, Jun 2007. 47, 48, 81

[57] A. H. B. de Vries, B. E. Krenn, R. van Driel, and J. S. Kanger, "Micro magnetic tweezers for nanomanipulation inside live cells," *Biophys J*, vol. 88, pp. 2137–2144, Jan 2005. 49

[58] A. H. B. de Vries, B. E. Krenn, R. van Driel, and J. S. Kanger, "Micro magnetic tweezers for nanomanipulation inside live cells.," *Biophys J*, vol. 88, pp. 2137–2144, mar 2005. 49

[59] T. Henighan, A. Chen, G. Vieira, A. J. Hauser, F. Y. Yang, J. J. Chalmers, and R. Sooryakumar, "Manipulation of magnetically labeled and unlabeled cells with mobile magnetic traps," *Biophys J*, vol. 98, pp. 412–7, Feb 2010. 50, 82

[60] H. Lee, Y. Liu, D. Ham, and R. M. Westervelt, "Integrated cell manipulation system–cmos/microfluidic hybrid," *Lab Chip*, vol. 7, pp. 331–7, Mar 2007. 51

[61] S. S. Shevkoplyas, A. C. Siegel, R. M. Westervelt, M. G. Prentiss, and G. M. Whitesides, "The force acting on a superparamagnetic bead due to an applied magnetic field," *Lab Chip*, vol. 7, pp. 1294–302, Oct 2007. 52, 82, 92

[62] A. C. Siegel, S. S. Shevkoplyas, D. B. Weibel, D. A. Bruzewicz, A. W. Martinez, and G. M. Whitesides, "Cofabrication of electromagnets and microfluidic systems in poly(dimethylsiloxane)," *Angew Chem Int Ed Engl*, vol. 45, pp. 6877–82, Oct 2006. 52

[63] Brainy Quote, "Henry ford quotes." Accessed May 18, 2011. `http://www.brainyquote.com/quotes/authors/h/henry_ford_2.html`. 53

[64] D. J. Stark, "The use of a microelectroporator to study poration of jurkat cells," Master's thesis, William Marsh Rice University, Houston, Texas, USA, 2009. 53, 55, 56, 58, 59, 60, 62, 63, 66, 67, 68, 70, 73, 82, 110, 218, 220, 221

[65] B. Lev, *Magnetic Microtraps for Cavity QED, Bose-Einstein Condensates, and Atom Optics*. PhD thesis, California Institute of Technology, 2005. 55

[66] Microchem, "Su-8 2000: Permanent epoxy negative photoresist." Accessed Jul. 4, 2011. `http://www.microchem.com/pdf/SU-82000DataSheet2000_5thru2015Ver4.pdf`. 59

[67] K. R. Williams, K. Gupta, and M. Wasilik, "Etch rates for micromachining processing-part ii," *J Microelectromech S*, vol. 12, no. 6, pp. 761–778, 2003. 59

[68] APEX Microtechnology, "Application note 13: Voltage to current conversion - power operational amplifier." Accessed Apr 13, 2011. `http://www.cirrus.com/en/pubs/appNote/Apex_AN13U_D.pdf`. 73

[69] W. H. Cropper, *Great Physicists: The Life and Times of Leading Physicists from Galileo to Hawking*. Oxford University Press, USA, nov 2001. 78, 213

[70] D. E. Ingber, "Cellular mechanotransduction: putting all the pieces together again," *FASEB Journal*, vol. 20, pp. 811–827, may 2006. 79

[71] K. C. Neuman and A. Nagy, "Single-molecule force spectroscopy: optical tweezers, magnetic tweezers and atomic force microscopy," *Nature methods*, vol. 5, pp. 491–505, jun 2008. 79

[72] M. S. Rocha and O. N. Mesquita, "New tools to study biophysical properties of single molecules and single cells," *Anais da Academia Brasileira de Ciências*, vol. 79, pp. 17–28, mar 2007. 80

[73] K. C. Neuman and S. M. Block, "Optical trapping," *Review Of Scientific Instruments*, vol. 75, pp. 2787–2809, sep 2004. 80

[74] A.-S. Smith and U. Seifert, "Vesicles as a model for controlled (de-)adhesion of cells: A thermodynamic approach," *Soft Matter*, vol. 3, pp. 275–289, jan 2007. 80, 101, 108, 138, 159, 163

[75] R. Merkel, P. Nassoy, A. Leung, K. Ritchie, and E. Evans, "Energy landscapes

of receptor-ligand bonds explored with dynamic force spectroscopy," *Nature*, vol. 397, pp. 50–53, jan 1999. 80, 101, 108, 129

[76] R. M. Hochmuth, N. Mohandas, and P. L. Blackshear, "Measurement of the elastic modulus for red cell membrane using a fluid mechanical technique," *Biophysical Journal*, vol. 13, pp. 747–762, aug 1973. 80

[77] R. M. Hochmuth and R. E. Waugh, "Erythrocyte membrane elasticity and viscosity," *Annual Review of Physiology*, vol. 49, pp. 209–219, jan 1987. 81

[78] R. E. Waugh, J. Song, S. Svetina, and B. Zeks, "Local and nonlocal curvature elasticity in bilayer membranes by tether formation from lecithin vesicles," *Biophysical Journal*, vol. 61, pp. 974–982, apr 1992. 81

[79] C. R. de Vries, J. Kanger, B. Krenn, and R. van Driel, "Patterned electroplating of micrometer scale magnetic structures on glass substrates," *Journal of Microelectromechanical Systems*, vol. 13, no. 3, pp. 391–395, 2004. 82

[80] M. Drndic, *Micro-Electromagnets for Particle Control*. PhD thesis, Harvard University, may 2000. 82

[81] C. Behrend, J. Anker, B. McNaughton, and R. Kopelman, "Microrheology with modulated optical nanoprobes (MOONs)," *J Magn Magn Mater*, vol. 293, pp. 663–670, jan 2005. 86, 94

[82] A. C. M. Kuo, "Poly(dimethylsiloxane)," in *Polymer Data Handbook* (J. E. Mark, ed.), pp. 411–435, Oxford University Press, 1999. 90, 206

[83] R. Kwok and E. Evans, "Thermoelasticity of large lecithin bilayer vesicles," *Biophysical Journal*, vol. 35, pp. 637–652, sep 1981. 90, 98, 214

[84] E. Glassinger, A. C. Lee, and R. M. Raphael, "Electromechanical effects on tether formation from lipid membranes: a theoretical analysis," *Physical Review E (Statistical, Nonlinear, and Soft Matter Physics)*, vol. 72, no. 4 Pt 1, p. 041926, 2005. 95

[85] E. J. G. Peterman, F. Gittes, and C. F. Schmidt, "Laser-induced heating in optical traps," *Biophysical Journal*, vol. 84, pp. 1308–1316, feb 2003. 95, 97

[86] Z. Li, B. Anvari, M. Takashima, P. Brecht, J. H. Torres, and W. E. Brownell, "Membrane tether formation from outer hair cells with optical tweezers," *Biophysical Journal*, vol. 82, pp. 1386–1395, mar 2002.

[87] P. M. Celliers and J. Conia, "Measurement of localized heating in the focus of an optical trap," *Applied optics*, vol. 39, pp. 3396–3407, jul 2000. 97

[88] H. Mao, J. R. Arias-Gonzalez, S. B. Smith, I. Tinoco, and C. Bustamante, "Temperature control methods in a laser tweezers system," *Biophysical Journal*, vol. 89, pp. 1308–1316, aug 2005. 95

[89] G. Koster, A. Cacciuto, I. Derényi, D. Frenkel, and M. Dogterom, "Force barri-

ers for membrane tube formation," *Physical Review Letters*, vol. 94, p. 068101, feb 2005. 101, 159, 163

[90] S. A. Nowak and T. Chou, "Models of dynamic extraction of lipid tethers from cell membranes," *Physical biology*, vol. 7, p. 026002, jan 2010. 101

[91] E. A. Evans and D. A. Calderwood, "Forces and bond dynamics in cell adhesion," *Science (New York, NY)*, vol. 316, pp. 1148–1153, may 2007. 101, 108, 129

[92] E. Evans and A. Yeung, "Apparent viscosity and cortical tension of blood granulocytes determined by micropipet aspiration," *Biophysical Journal*, vol. 56, pp. 151–160, jul 1989. 102

[93] Great Quotes, "Science quotes." Accessed Jul 23, 2011. `http://www.great-quotes.com/quotes/category/Science/pg/2`. 105

[94] S. Leitenberger, E. Reister-Gottfried, and U. Seifert, "Curvature coupling dependence of membrane protein diffusion coefficients," *Langmuir : the ACS journal of surfaces and colloids*, vol. 24, no. 4, pp. 1254–1261, 2008. 107

[95] W. Häckl, U. Seifert, and E. Sackmann, "Effects of Fully and Partially Solubilized Amphiphiles on Bilayer Bending Stiffness and Temperature Dependence of the Effective Tension of Giant Vesicles," *Journal de Physique II*, vol. 7, pp. 1141–1157, 1997. 107

[96] H.-G. Döbereiner, "Properties of giant vesicles," *Current Opinion in Colloid and Interface Science*, vol. 5, no. 3-4, pp. 256–263, 2000. 107

[97] U. Seifert, "Configurations of fluid membranes and vesicles," *Advances in Physics*, vol. 46, no. 1, pp. 13–137, 1997. 107

[98] N. Maeda, T. J. Senden, and J.-M. di Meglio, "Micromanipulation of phospholipid bilayers by atomic force microscopy.," *Biochimica et biophysica acta*, vol. 1564, pp. 165–172, Aug. 2002. 107

[99] T. R. Powers, G. Huber, and R. E. Goldstein, "Fluid-membrane tethers: minimal surfaces and elastic boundary layers.," *Physical Review E (Statistical, Nonlinear, and Soft Matter Physics)*, vol. 65, p. 041901, Apr. 2002. 107

[100] I. Derényi, F. Jülicher, and J. Prost, "Formation and interaction of membrane tubes.," *Physical Review Letters*, vol. 88, p. 238101, June 2002. 108

[101] A.-S. Smith, E. Sackmann, and U. Seifert, "Pulling tethers from adhered vesicles," *Physical Review Letters*, vol. 92, p. 208101, May 2004. 108

[102] M. K. Pospieszalska, I. Lasiecka, and K. Ley, "Cell Protrusions and Tethers: A Unified Approach," *Biophysical Journal*, vol. 100, pp. 1697–1707, Apr. 2011. 108

[103] W. Brownell, F. Qian, and B. Anvari, "Cell Membrane Tethers Generate Me-

chanical Force in Response to Electrical Stimulation," *Biophysical Journal*, vol. 99, pp. 845–852, Aug. 2010. 132

[104] Brainy Quote, "Ralph waldo emerson quotes." Accessed Jul 28, 2011. `http://www.brainyquote.com/quotes/quotes/r/ralphwaldo101056.html`. 136

[105] Nylund, Fortelius, Palonen, Molotkovsky, and Mattjus, "Membrane Curvature Effects on Glycolipid Transfer Protein Activity," *Langmuir : the ACS journal of surfaces and colloids*, Oct. 2007. 138

[106] J. L. Rubenstein, B. A. Smith, and H. M. McConnell, "Lateral diffusion in binary mixtures of cholesterol and phosphatidylcholines," *Proceedings of the National Academy of Sciences of the United States of America*, vol. 76, pp. 15–18, Jan. 1979. 144

[107] L. R. Arriaga, I. López-Montero, F. Monroy, G. Orts-Gil, B. Farago, and T. Hellweg, "Stiffening effect of cholesterol on disordered lipid phases: a combined neutron spin echo + dynamic light scattering analysis of the bending elasticity of large unilamellar vesicles," *Biophysical Journal*, vol. 96, pp. 3629–3637, May 2009. 144, 150, 193

[108] W. Rawicz, B. A. Smith, T. J. McIntosh, S. A. Simon, and E. Evans, "Elasticity, strength, and water permeability of bilayers that contain raft microdomain-forming lipids," *Biophysical Journal*, vol. 94, no. 12, pp. 4725–4736, 2008. 146

[109] R. Parthasarathy, C.-h. Yu, and J. T. Groves, "Curvature-modulated phase separation in lipid bilayer membranes," *Langmuir : the ACS journal of surfaces and colloids*, vol. 22, pp. 5095–5099, May 2006. 146

[110] D. Needham and R. S. Nunn, "Elastic deformation and failure of lipid bilayer membranes containing cholesterol," *Biophysical Journal*, vol. 58, pp. 997–1009, Oct. 1990. 150

[111] Brainy Quote, "Albert einstein quotes." Accessed Jul 23, 2011. `http://www.brainyquote.com/quotes/quotes/a/alberteins133826.html`. 171

[112] Brainy Quote, "Chemistry quotes." Accessed May 9, 2011. `http://www.brainyquote.com/quotes/keywords/chemistry.html`. 193

[113] R. C. MacDonald, R. I. MacDonald, B. P. Menco, K. Takeshita, N. K. Subbarao, and L. R. Hu, "Small-volume extrusion apparatus for preparation of large, unilamellar vesicles.," *Biochimica et biophysica acta*, vol. 1061, pp. 297–303, jan 1991. 193

[114] A. Samad, Y. Sultana, and M. Aqil, "Liposomal drug delivery systems: An update review," *Current Drug Delivery*, vol. 4, no. 4, pp. 297–305, 2007. 193

[115] Brainy Quote, "Mathematics quotes." Accessed May 12, 2011. `http://www.brainyquote.com/quotes/keywords/mathematics.html`. 201

[116] *COMSOL Multiphysics User's Guide*. COMSOL AB, 2007. 202, 204

[117] Swiss Jewel, "Properties of synthetic sapphire." Accessed Jul. 4, 2011. http://www.swissjewel.com/images/uploads/Properties%20of%20Sapphire(2).pdf. 206

[118] A. Steel, 2010. Email correspondence with Swiss Jewel on Sep 8, 2010. 206

[119] Brainy Quote, "Brian greene quotes." Accessed Aug 4, 2011. http://www.brainyquote.com/quotes/authors/b/brian_greene.html. 207

[120] H. Kotani, H. Kawaguchi, T. Shimoaka, M. Iwasaka, S. Ueno, H. Ozawa, K. Nakamura, and K. Hoshi, "Strong static magnetic field stimulates bone formation to a definite orientation in vitro and in vivo," *Journal of bone and mineral research : the official journal of the American Society for Bone and Mineral Research*, vol. 17, pp. 1814–1821, oct 2002. 213

[121] K.-H. Chiu, K.-L. Ou, S.-Y. Lee, C.-T. Lin, W.-J. Chang, C.-C. Chen, and H.-M. Huang, "Static magnetic fields promote osteoblast-like cells differentiation via increasing the membrane rigidity," *Annals of biomedical engineering*, vol. 35, pp. 1932–1939, nov 2007. 213

[122] Brainy Quote, "Samuel johnson quotes." Accessed Jul 3, 2011. http://www.brainyquote.com/quotes/quotes/s/samueljohn101039.html. 218

[123] Shipley, "Microposit s1800š series photo resists." Accessed Jul. 4, 2011. http://www.nanophys.kth.se/nanophys/facilities/nfl/resists/S1813/s1800seriesDataSheet.pdf. 219

[124] G. Room, "Photolithography." Accessed Jul. 23, 2009. http://www.ece.gatech.edu/research/labs/vc/theory/photolith.html. 220

Appendix A

Vesicle Making Protocol

Chemistry has been termed by the physicist as the messy part of physics, but that is no reason why the physicists should be permitted to make a mess of chemistry when they invade it. - Frederick Soddy [112]

This appendix explains how to grow polydisperse giant unilamellar vesicles by electroformation. The vesicles may grow up to a diameter of up to $\sim 30\,\mu$m, but the majority of vesicles are only a few microns in diameter. Monodisperse vesicles may be formed using the extrusion method [107, 113, 114], but will not be covered here. The necessary stock solutions will, however, be discussed. Additionally, the cleaning, desiccation, electroformation, and storage procedures will be given below.

A.1 Stock solutions

Standard lipid stock solutions that have been used in the author's doctoral work have included components consisting of 18:0-18:1 PC 1-stearoyl-2-oleoyl-*sn*-glycero-3-phosphocholine (SOPC, $M_w = 788\,\mathrm{g/mol}$), 16:0-18:1 PC 1-palmitoyl-2-oleoyl-*sn*-glycero-3-phosphocholine (POPC, $M_w = 760.\,\mathrm{g/mol}$), *N*-((6-(biotinoyl)amino)hexanoyl)-1,2-dihexadecanoyl*sn*-glycero-3-phosphoethanolamine, triethylammonium salt (biotin-X DHPE, $M_w = 1133\,\mathrm{g/mol}$), 18:0-18:1 PC 1-stearoyl-2-oleoyl-*sn*-glycero-3-phospho-L-serine (SOPS, $M_w = 812\,\mathrm{g/mol}$), and cholesterol ($M_w = 386\,\mathrm{g/mol}$). SOPC and POPC

Table A.1 : Solution recipes for SOPC–Biotin-X lipids

% by mole	Material	Volume (μL)
0.5	Biotin-X	7.2
99.5	SOPC	1000
1	Biotin-X	14.5
99	SOPC	1000
5	Biotin-X	75.6
95	SOPC	1000
8	Biotin-X	125
92	SOPC	1000

Table A.2 : Solution recipes for POPC–Biotin-X lipids

% by mole	Material	Volume (μL)
0.5	Biotin-X	7.5
99.5	POPC	1000
1	Biotin-X	15.1
99	POPC	1000
5	Biotin-X	78.5
95	POPC	1000
8	Biotin-X	129.7
92	POPC	1000

Table A.3 : Solution recipes for SOPC–Biotin-X–SOPS lipids

% by mole	Material	Volume (μL)
0.5	SOPS	5.4
5	Biotin-X	76
94.5	SOPC	1000
1	SOPS	11
5	Biotin-X	76.4
94	SOPC	1000
5	SOPS	57.2
5	Biotin-X	79.8
90	SOPC	1000
8	SOPS	94.7
5	Biotin-X	82.6
87	SOPC	1000

Table A.4 : Solution recipes for SOPC–Biotin-X–Cholesterol lipids

% by mole	Material	Volume (μL)
5	Cholesterol	27.3
5	Biotin-X	79.8
90	SOPC	1000
15	Cholesterol	92
5	Biotin-X	89.8
80	SOPC	1000
25	Cholesterol	175.2
5	Biotin-X	102.6
70	SOPC	1000
35	Cholesterol	286.2
5	Biotin-X	119.8
60	SOPC	1000
45	Cholesterol	441.5
5	Biotin-X	143.7
50	SOPC	1000

have the proper spontaneous curvature to form bilayer vesicles. Biotin-X DHPE consists of biotinylated lipids that provide adhesion sites, and SOPS disrupts membranes. Cholesterol is a sterol that provides long range order to membranes. All stock solutions should be stored in *amber* (brown) glass vials in the $-20\,^{\circ}\mathrm{C}$ freezer. Stock solutions for SOPC–Biotin-X (Table A.1), POPC–Biotin-X (Table A.2), SOPC–SOPS–Biotin-X (Table A.3) and SOPC–Biotin-X–Cholesterol (Table A.4) vesicles are given below with all concentrations of source material at $1\,{}^{\mathrm{mg}}/_{\mathrm{mL}}$.

A.2 Cleaning

The first step in forming vesicles is to clean the electrodes and chamber in order to ensure there is no contamination in the sample. Contamination may lead to vesicles forming improperly or not at all.

1. Rinse the electrodes with pure ethyl alcohol,
2. Soak the electrodes in chloroform in a clean beaker until steps 3. and 4. are completed,
3. Rinse the chamber with pure ethyl alcohol, while making sure to also rinse out the electrode holes,
4. Dry the chamber, including electrode holes, with nitrogen,
5. Rinse the electrodes with *clean* chloroform,
6. Dry the electrodes with nitrogen,

7. Place electrodes in the chamber and place the chamber in the vacuum desiccator.

A.3 Lipid Desiccation

Lipids are stored in chloroform. In order for the vesicles later to form in aqueous solution, the chloroform must be removed. Vacuum desiccation accomplishes this task.

1. Clean the 50 μL Hamilton syringe with *clean* chloroform,
2. Sonicate the lipid solution for 2 min,
3. Place 15 μL of lipid solution on each electrode *evenly*,
4. Seal the chamber, electrode, and lipid solution in the vacuum desiccator,
5. Desiccate for at least 2 hr,
6. Purge the vial containing the lipid solution with nitrogen,
7. Secure the lid of the vial with parafilm,
8. Cover the entire vial with aluminum foil if the lipids are fluorescent,
9. Place lipids back in $-20\,^{\circ}$C freezer.

A.4 Electroformation

After waiting at least 2 hr in order for the chloroform to desiccate, the resulting lipid-covered electrodes may be used to form vesicles. Growing the vesicles in a sugar

solution, such as in a sucrose solution, facilitates viewing vesicle membranes in the future via a difference in index of refraction between the internal solution of the vesicle and a separate external solution, such as 120 mM dextrose solution (0.216 g dextrose in 10 mL DI water). Further, with a difference in the osmolarity of the solutions inside and outside the vesicle, excess surface area area may be adjusted. Finally, a longer exposure to a low frequency signal, *i.e.* 150 min in step 4(g), creates an increased number of vesicles.

1. Make 10 mL of 100 mM sucrose solution, or 0.342 g sucrose in 10 mL DI water,
2. Place the sucrose solution in a 10 mL syringe with a filter,
3. Cut a pipet tip to fit the filter and place on the filter,
4. Make sure LabView Program is set to correct settings:
   (a) 250 mV amplitude, 10 Hz, 10 min
   (b) 500 mV amplitude, 10 Hz, 10 min
   (c) 750 mV amplitude, 10 Hz, 10 min
   (d) 1000 mV amplitude, 10 Hz, 10 min
   (e) 750 mV amplitude, 6.6 Hz, 10 min
   (f) 500 mV amplitude, 3.3 Hz, 10 min
   (g) 250 mV amplitude, 1.1 Hz, $90 - 150$ min,
5. Remove the chamber from the vacuum desiccator,

6. Secure both sides of the chamber with cover slips to keep fluid from leaking (making sure to leave some access to the chamber),
7. Fill the chamber with sucrose solution,
8. Place the chamber securely on the microscope stage and attach alligator clips,
9. Use the microscope to watch the vesicle formation, if desired,
10. LabView program will cease running on its own.

A.5 Storage

Proper storage of the vesicles prolongs the stability of the biotin groups on the Biotin-X DHPE lipids. The biotin groups are necessary to adhere the magnetic beads to the vesicle.

1. Drain the solution from the chamber, using a glass Pasteur pipet,
2. Release the back into the chamber,
3. Repeat step 1.,
4. Place the solution in an *amber* vial,
5. Purge the vial using nitrogen,
6. Parafilm and foil the vial,
7. Label with substance, date, and initials,

8. Place in the 4 °C refrigerator,

9. Rinse the chamber and electrodes briefly with pure ethyl alcohol.

Appendix B

Numerical Modeling with COMSOL

As far as the laws of mathematics refer to reality, they are not certain, and as far as they are certain, they do not refer to reality. - Albert Einstein [115]

DUE to the complicated geometry and large differences in material properties of components of the magnetic force transducer (MFT), ascertaining its thermal response analytically is strenuous, and possibly unfeasible. However, the thermal response may still be calculated using numerical methods. In particular, the thermal characteristics have been modeled using the commercial package COMSOL. COMSOL is a graphical user interface that allows the user to develop pictorially a three dimensional model of a system with defined governing equations and conditions; COMSOL then uses finite element methods to solve the system, either in a static or a dynamic state. The material model governing the system is presented below. This presentation will be followed by a discussion of the material properties of each of the components. Specifics necessary for numerical evaluation ends the development in this appendix.

B.1 Governing Relations

The high current density, up to $\sim 10^9\,{}^{\mathrm{A}}/_{\mathrm{m}^2}$ (corresponding to $\sim 3\,\mathrm{A}$), that passes through the wire generates much heat. The heat is dissipated by diffusion through connected material, or in other words, via conduction. In particular, the sapphire substrate dominates the heat dissipation process (as discussed below). Surprisingly, convection plays little role at the current densities used in this thesis. This may be due to geometric constraints limiting fluid flow. Regardless, the heat transfer within the system at temperature, T, spreads the power density, $\dot{q}$, according to the heat conduction equation [116]

$$\rho C_p \frac{\partial T}{\partial t} = \dot{q} + \nabla \cdot (k \nabla T)\,, \tag{B.1}$$

where ρ is the relevant density, C_p is the heat capacity, t is the time, and k is the thermal conductivity. The first right hand term in Equation B.1 states that a source of heat may cause an increase in temperature; the second right hand term behaves as a diffusion term that is scaled by the thermal conductivity, which is isotropic for all components of the MFT system. Finally, the density and heat capacity, which scale the temperature rate, determine how quickly the system responds.

B.2 Material Properties

The COMSOL model is composed of a graphical representation of the three dimensional geometry of the MFT system. The representation consists of blocks correspond-

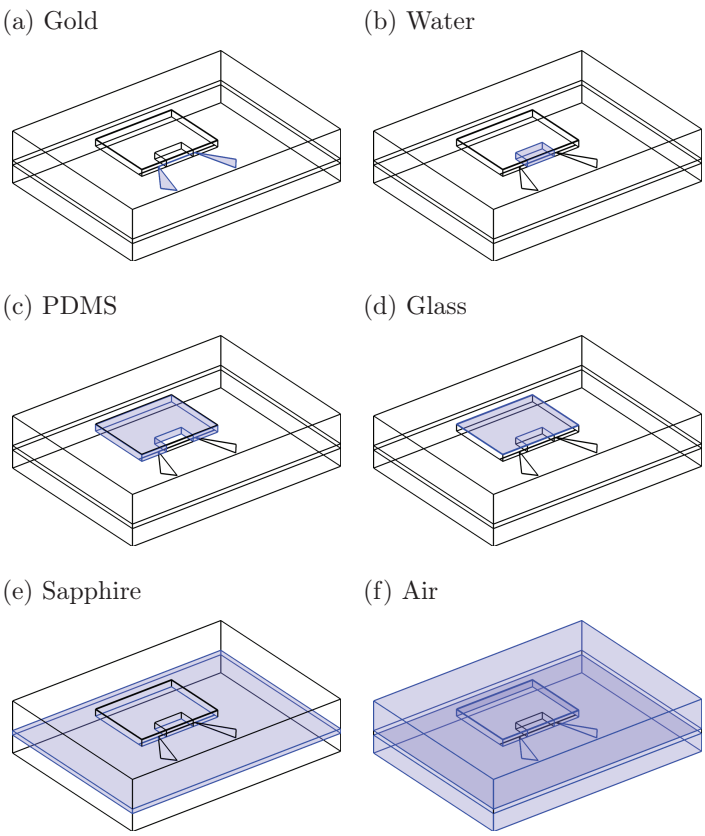

Figure B.1 : The geometric regions of the MFT. Each subfigure depicts one of the main material types used in the COMSOL simulation. The blue shading highlights the selected material. (a) The blue shading indicates the gold pads and gold wire, but only the wire is assumed to generate heat. (b) Water surrounds the gold wire and dissipates heat. (c) PDMS creates a chamber that contains the water. (d) A glass coverslip provides the top of the chamber and contributes to containing the water through capillary action. (e) Sapphire serves not only to provide support to the substrate but to act as a heat sink, spreading much of the power away from the wire. (f) A layer of air several millimeters thick also slightly attenuate temperature increases by removing heat from the sapphire substrate through convection.

ing to each material (see Figure B.1), each with its own set of material properties. The materials modeled for this work are gold wires and pads (Figure B.1a), water that surrounds the gold and dissipates heat (Figure B.1b), a polydimethylsiloxane chamber to contain the water (PDMS, Figure B.1c), a glass coverslip on top of the PDMS to provide capillary action in holding the solution (Figure B.1d), a sapphire substrate and heat sink (Figure B.1e), and air surrounding the entire device (Figure B.1f).

The thermally relevant properties for these materials is enumerated in Table B.1. The power density, $\dot{q}_{gold}$, for the gold wire is scaled by the Heaviside function, $H\left(t_{stop} - t\right)$, where t_{stop} is the time that the current stops flowing through the wire*. The magnitude for $\dot{q}_{gold}$ was experimentally determined using a four-point probe method to determine the current passing through the device and its respective voltage drop; the power was taken as $P = IV$. Additionally, the density, ρ_{air}, of air was determined using the ideal gas law (assuming standard pressure). As can be see in Table B.1, the thermal conductivity of sapphire, k_{sapph}, is several orders of magnitude larger than glass. It is also significantly larger than the conductivity of water at the relevant temperatures for this experiment ($0.6062\,{}^{\mathrm{W}}/_{\mathrm{m\cdot K}}$). As such, the sapphire substrate is the main component dissipating the Joule heat generated by the microfabricated gold wire.

*The particular function is flsmhs, "a smoothed Heaviside function with a continuous first derivative and overshoot on both sides of the step." [116]

B.3 Numerical Considerations

In addition to correct material properties, COMSOL must have proper boundary and initial conditions in order to converge. All initial temperatures were set at $T = 293.15\,\mathrm{K}$, as were all outer boundaries. Boundaries between one component and another obeyed continuity. Within all the components, 184,833 mesh points—the maximum the computer could handle without freezing—determined spatial evaluation locations. Temporal evaluation took time steps of no larger than 0.1 sec with an initial time step of 0.001 sec, which was automatically determined by COMSOL.

Table B.1 : Material Constants for the MFT COMSOL model. T denotes the magnitude of temperature in Kelvin. The values for water are not included as its material properties relevant for this work came from involved built-in functions in the COMSOL library. All other values were from the COMSOL 3.4 Materials Library included with the program, unless otherwise noted.

Material	k ($\mathrm{W/m{\cdot}K}$)	ρ ($\mathrm{kg/m^3}$)	C_p ($\mathrm{J/kg{\cdot}K}$)	$\dot{q}$ ($\mathrm{W/m^3}$)
Gold	318	19300	128	1.65×10^{11} (wire) 0 (pads)
PDMS [82]	0.15	0.97	1460	0
Glass	1.05	2500	840	0
Sapphire [117]	32.5 [118]	3980	757.2	0
Air	$(T - 3.7142)^{0.8616}$	$\frac{351}{T}$	$0.0769T + 1076.9$	0

Appendix C

A Newtonian Explanation of Tether Formation?

If the theory turns out to be right, that will be tremendously thick and tasty icing on the cake. - Brian Greene [119]

A possible model to explain the dependence of the force threshold to pull a tether to the force ramp, as seen in Figure 6.4, is a purely Newtonian model that assumes that any energetic barriers or topological reorganization of the membrane could be combined together into a distance L such that a tether would form once the membrane had extended this distance. This section develops the Newtonian model and compares it to the observed relationship of Figure 6.4 and to force threshold studies conducted with pulsed, instead of ramped, current.

Given that the magnetic bead that provided the point force to the membrane was in the low Reynolds number regime, the velocity of membrane motion at the point of force application is given by

$$\dot{x} = \frac{f}{\beta}, \tag{C.1}$$

where β is the drag constant and $f = \left({}^{df}/_{dt}\right) t$, with ${}^{df}/_{dt}$ as the force ramp. After a time t, the membrane would move a distance

$$x\left(t\right) = \int_0^t \dot{x}\left(t'\right) dt' = \int_0^t \frac{\left({}^{df}/_{dt}\right) t'}{\beta} dt' = \frac{1}{2} \frac{\left({}^{df}/_{dt}\right)}{\beta} t^2, \tag{C.2}$$

leading to a time taken until a tether formed as

$$t_{th,ramp} = \sqrt{\frac{2\beta L}{{}^{df}/_{dt}}}, \tag{C.3}$$

and finally a threshold force was given by

$$F_{th,ramp} = \left({}^{df}/_{dt}\right) t_{th} = \sqrt{2\beta L}\left({}^{df}/_{dt}\right)^{1/2}. \tag{C.4}$$

This exponent of 0.5 for ${}^{df}/_{dt}$ was similar to the exponent of 0.42 observed for SOPC vesicles with 5 mol% biotinylated lipids when experiencing a force ramp (see Figure C.1) and so suggests that this Newtonian model explains the force threshold-force rate dependence observed .

Applying the same logic to a pulse of constant force f,

$$x\left(t\right) = \int_0^t \dot{x}\left(t'\right) dt' = \int_0^t \frac{f}{\beta} dt' = \frac{f}{\beta} t. \tag{C.5}$$

This led to a expected t_{th} of

$$t_{th,pulse} = \frac{\beta L}{f}. \tag{C.6}$$

This model predicted that if a force pulse equal to $F_{th,ramp}$ was applied to a magnetic bead attached to a vesicle, a tether would form in less time than it would during a ramp but it would not form instantaneously. Further, the time taken to form a tether with a pulse t_{th} should be inversely proportional to the applied force.

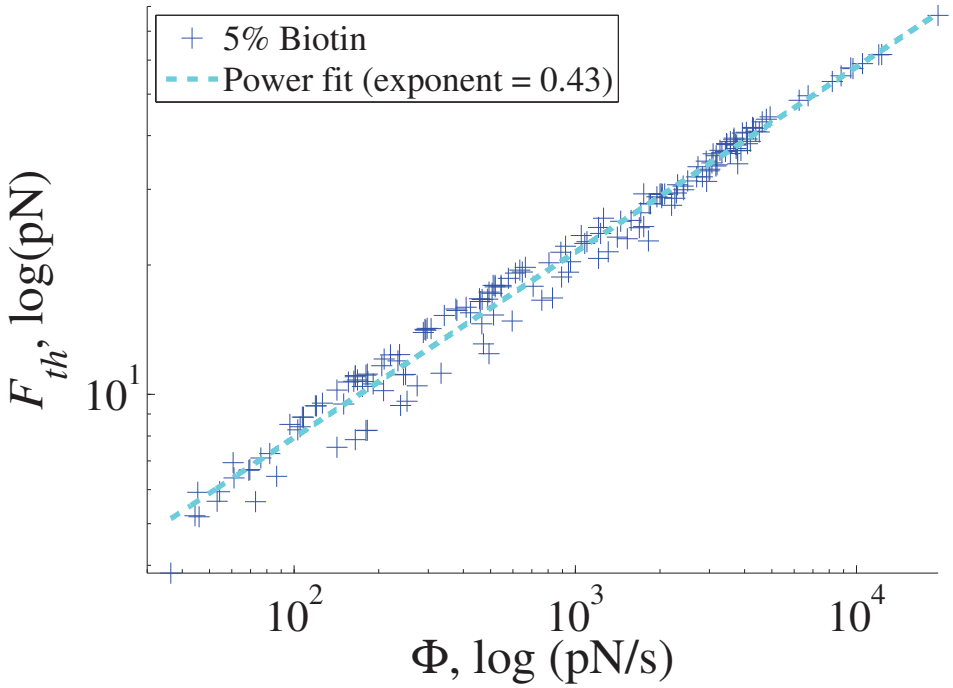

Figure C.1 : Log-log plot of F_{th} against $^{df}/_{dt}$ for standard SOPC vesicles with 5 mol% biotinylated lipids. A power law with exponent 0.43 fitted the data.

To test this model and demonstrate the versatility of the transducer, square pulse studies were conducted by first pulling tethers from a vesicle using the standard ramp protocol to establish a control. Second, current pulses of varying magnitude were applied. The time taken to form a tether t_{th} and the normalized force deviation from force threshold during a ramp $\overline{\Delta f}$ were determined for each tether formed during a pulse. $\overline{\Delta f}$ is defined as

$$\overline{\Delta f} \equiv \frac{F_{th,pulse} - F_{th,ramp}}{F_{th,ramp}}. \tag{C.7}$$

Figure C.2 depicts the spread of t_{th} with assorted $\overline{\Delta f}$. As can be viewed in Figure C.2a, the majority of tethers formed within 200 ms, even as $\overline{\Delta f}$ varied up to 20%. Longer times indicated either the presence of an energy barrier, in contradiction to the Newtonian model, or anomalous stickiness of the membrane. Furthermore, there was little correlation between the two observables (see Figure C.2b). Finally, as βL was the same between whether the force was ramped or pulsed,

$$F_{th,ramp} t_{t,pulse} = \frac{\left({}^{df}/_{dt}\right) t_{th,ramp}^2}{2}. \tag{C.8}$$

From Figure C.2b, $t_{th,pulse}$ was a fraction of a second. From Figure C.1, $F_{th,ramp}$ was on the order of $\sim 10^1$ pN. Further, ${}^{df}/_{dt}$ was on the order of $10^2 - 10^3$ ${}^{\text{pN}}/_{\text{s}}$ and $t_{th,ramp}$ was several seconds. So the right hand side was several orders of magnitude less than the right hand side.

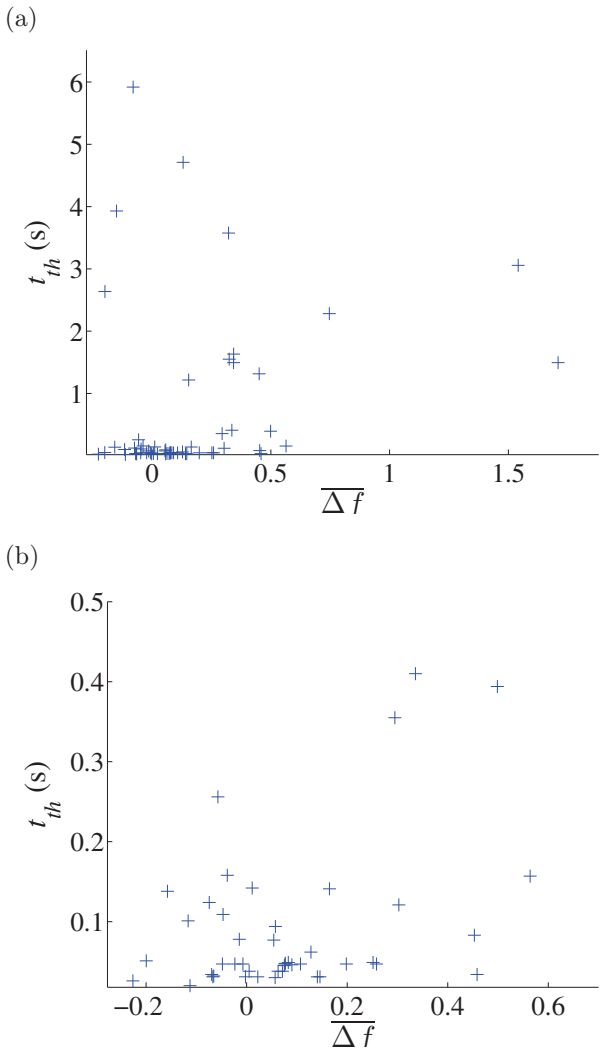

Figure C.2 : The time until a tether forms t_{th} after a force is applied as a function of the normalized applied force difference $\overline{\Delta f}$. The normalized force is the ratio of the force difference at which a tether forms for a pulse and a ramp to the force at which a tether forms for the corresponding ramp. (a) Most tethers pulled within 20% of $\overline{\Delta f} = 0$ (40 of 62 tethers from 11 vesicles), and 49 of 62 tethers took less than 0.5 s after application of force to initiate formation. Even though the tethers are concentrated at short times and near $\overline{\Delta f} = 0$, some tethers formed over 150% higher. Other tethers took up to 6 s to initiate, possibly due to anomalous stickiness. (b) Even at low t_{th}, there is little correlation between t_{th} and $\overline{f}$.

The lack of correlation, the typically low times observed during a pulse protocol, and the contradiction in determination of βL between the two models indicated that the Newtonian model, in fact, did not hold up to scrutiny.

Appendix D

Magnetic Field Effect On Lipids

I am no poet, but if you think for yourselves, as I proceed, the facts will form a poem in your minds. - Michael Faraday [69, p. 145]

Heat dominated the growth of the projection of an aspirated giant unilamellar vesicle (GUV), as discussed in Section 5.4.2 with experimental work presented in Section 5.3.6 and modeling in Appendix B. However, recent work suggests that the magnetic field may affect membrane mechanical properties through increased magnetic flux density or due to an imbalance in the transmembrane hydrostatic pressure [120, 121]. These works examined the effects of a static magnetic field. As noted above, this thesis has already addressed the reaction of the GUV to a static applied current. The case of an alternating current (AC), though, is presented below*.

D.1 Methods

To examine the consequence of an AC field on the mechanical behavior of a GUV, alternating currents at various frequencies flowed through the magnetic force transducer near an aspirated GUV. Vesicle were generated via electroformation as outlined in Section 5.3.2 and aspirated as covered in Section 5.3.4. Briefly, 1-stearoyl-2-oleoyl-

*The experiments conducted to obtain the results presented here were done, under the guidance of the author, by Shinji Strain of the University of Texas during his participation in a Research Experience for Undergraduates program at Rice University.

sn-glycero-3-phosphatidylcholine (SOPC) lipids were desiccated onto two platinum electrodes. Under a multi-step alternating voltage, the lipids spontaneously self-assembled in a sucrose solution. Aspiration pipettes were fabricated using a puller and cut cleanly on a custom-built microforge.

D.2 Results and Discussion

As the vesicle responded slowly to an AC magnetic field, the maximum areal strain was used to determine the influence of the field at multiple frequencies. The areal strain, α, may be determined using Equation 5.3, which is

$$\alpha = \frac{2R_P\Delta L\,(1 - {}^{R_P}\!/_{R_V})}{4R_V^2 - R_P^2 + 2R_P L_0}, \tag{D.1}$$

where R_P is the pipette radius, R_V is the vesicle radius, ΔL is the change in projection length, and L_0 is the initial projection length [33, 83]. As seen in Figure D.1, α lowers from 1.34 % at 1 Hz to 0.9 % by 100 Hz. This change may be due to a varying magnetic response; however, two features indicate that a magnetic response may not be the explanation. First, above 100 Hz, no significant reduction in maximum areal strain occurs. Second, the areal strain at low frequency (1 Hz) is close to $\sqrt{2}$ higher than that at high frequency (100 Hz). Rather than the magnetic field causing the feedback seen, heating may account for the effect.

In order to separate heating on the system from the frequency of the field, a multiple segment current was passed through the MFT and the reaction of an aspirated

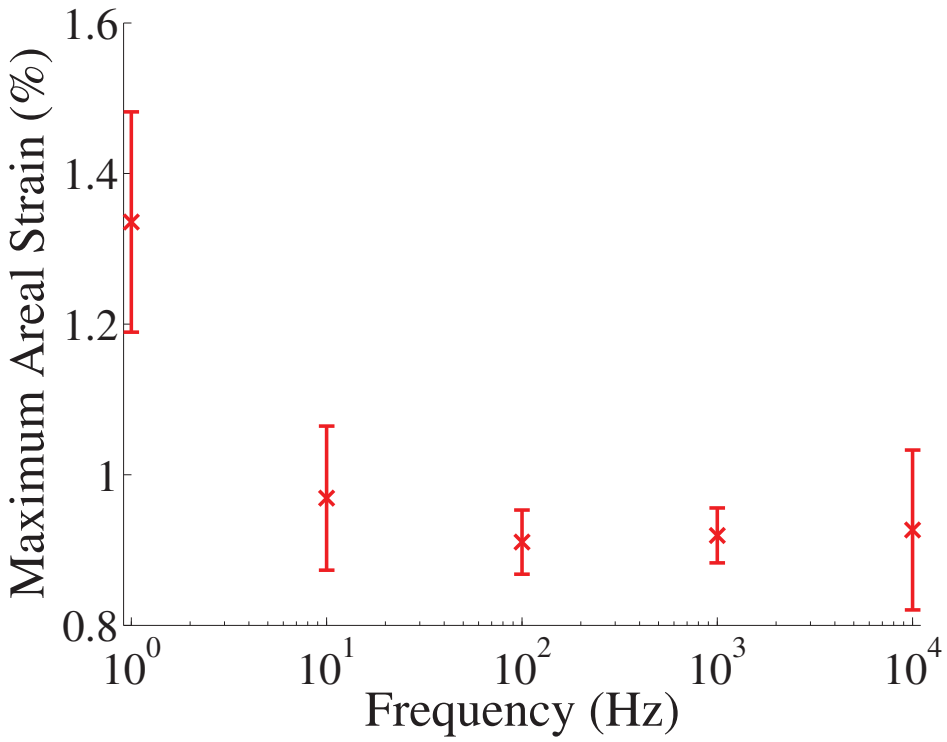

Figure D.1 : Areal strain, α, as a function of frequency of applied magnetic field. The maximum areal strain decreases with increasing frequency at or below 100 Hz. Above 100 Hz, there appears to be no dependence of α on frequency. The magnitude at 1 Hz is $\sqrt{2}$ higher than the magnitude observed at higher frequency, indicating heating—rather than magnetic fields—may be the dominate mechanism when the MFT generates oscillatory fields.

(a)

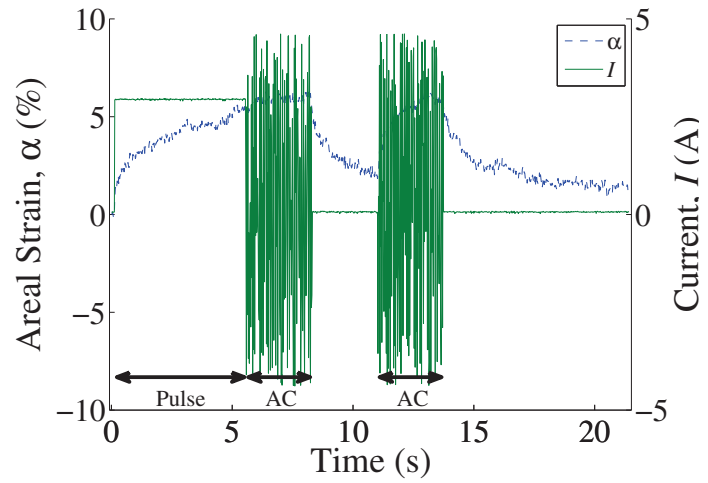

(b)

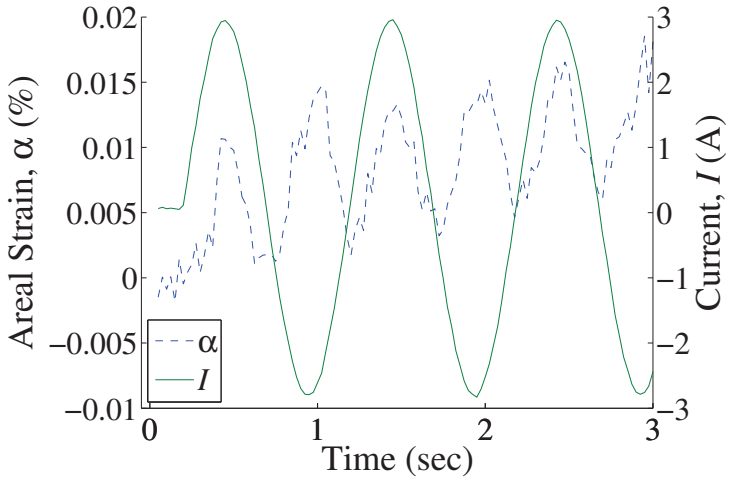

Figure D.2 : Sample areal strains with various pulse and alternating current waveforms. (a) Areal strain (dashed blue line) under a constant current pulse (solid green line) followed by AC segments. The areal strain does not change form between the applied current pulse and the AC segments. Likewise, the second AC segment instigates an increase of the same form as the constant applied current pulse. (b) The areal strain following the current at low frequency. The areal strain always increases, even when the current is negative, as the voltage also goes negative, leaving the power (IV) positive. The power drives the thermal response of the vesicle.

GUV was observed. The current consisted of a constant pulse for 6 sec followed directly by a sinusoidal pulse of 2 sec at 1000 Hz and an amplitude $\sqrt{2}$ higher than the constant pulse, which can be seen in Figure D.2a. A second sinusoidal pulse then came a few seconds later. The amplitude of α and its growth against time did not vary while the constant pulse was replaced by the AC segment. Further, the behavior of α during the second AC segment mimics that seen during the constant pulse. The consistency between the two very different waveforms is describable using the thermal response of the system, given a response time, T_r, on the order of $\frac{1}{10^1}$ sec (as determined from Figure D.1). With frequencies corresponding to below T_r, the vesicle is able to follow the waveform precisely (see Figure D.2b); the maximum extension corresponds to the power output (IV). With frequencies corresponding to times above T_r, however, the vesicle experiences a time average of the power, namely

$$\frac{1}{T_{AC}} \int_0^{T_{AC}} IV \, \sin^2\left(\frac{2\pi t}{T_r}\right) dt \approx \frac{IV}{2}, \tag{D.2}$$

where T_{AC} is some time much greater than T_r during the AC pulse. With an increase of the voltage V by $\sqrt{2}$ and a corresponding increase in I, the power output is the same as at lower frequencies. Thus, a thermal reaction, not a magnetic one, explains the response of vesicles to the current.

Appendix E

Fabricating with S1813

Knowledge is of two kinds. We know a subject ourselves, or we know where we can find information upon it. - Samuel Johnson [122]

As alluded to in Chapter 4, there are alternative materials and methods that one may want to use in the microfabrication process*. This appendix begins by examining the use of S1813, a common photoresist, in the creation of microfabricated devices. In particular, the spinning, soft-baking, developing, and lifting-off of the photolithography process will be detailed.

E.1 Overview

In addition to the SU-8 series photoresists, S1813 (Microchem, Newton, MA) is a very common photoresist when one wants a thin resist for higher resolution patterns. S1813 is a positive resist; the resulting pattern matches the mask used during UV exposure. S1813 requires no priming coat on the substrate in order to bond to the substrate, and no spreading cycle during spinning is necessary [64]. As only a few milliliters are used each time, the bulk resist in storage generally expires before it has been used. As it ages, it thickens. Finally, S1813 reacts with certain plastics, so long-term storage in plastic flasks is not advised. The procedure below was adapted

*Much of this appendix is based upon Stark [64].

from the datasheet for S1813 provided by Microchem [123].

E.2 Spinning

For a 1.3-micron-thick film of S1813, a very similar procedure as for SU-8 2015 may be followed. However, as S1813 is not as viscous, a spreading cycle is not necessary as long as the entire substrate is covered before spinning. A spinning cycle of 2000 rpm for 30 seconds with a 500 rpm/s ramp will form the necessary film. If the film is not completely covered, one may clean the substrate and spin again.

While seemingly simple, Stark has explained that spinning does require some care. First, photoresist may accumulate on the substrate edge–particularly for non-circular substrates–as the extra resist is not flung off the substrate but sticks. A bead may be up to a few hundred microns thick, leading to a gap between the resist and the mask during aligning and exposing. Extra space between the resist and mask can lead to improper exposure of resist at pattern boundaries, causing structures to form improperly. The bead edge may be removed chemically using either Bead Edge Remover (Microchem) or mechanically by carefully wiping the resist with a clean room cloth soaked with acetone. Another concern is if a substrate is not clean, the resist may not stick or be evenly spread. If this complication occurs, the substrate may simply be cleaned using a 20-minute acetone bath in an ultrasound, followed by residue removal with isopropyl alcohol and deionized (DI) water or methanol. Baking the substrate on a hotplate may be required to remove adherent water. Thereafter,

the resist may be reapplied. Further, if S1813 does not adhere, and cleaning the substrate as already described is not sufficient, applying a coat of MCC Primer acts as an adhesion layer for S1813. And as should be noted for every fabrication step, times and temperatures of any step vary depending on desired thickness [64].

E.3 Soft-baking

Soft-baking S1813 consists of heating the substrate to 115 °C for one minute. When heating, resist can withdraw from the edges of the substrate as the solvent evaporates away [64]. If it does so, then either clean the resist off the substrate, spin and soft-bake again, or use the pattern as it is and accept that some portions of the pattern will not be present. Also, the Georgia Tech clean room manual [124] states:

> Oversoft-baking will degrade the photosensitivity of resists by either reducing the developer solubility or actually destroying a portion of the sensitizer. Undersoft-baking will prevent light from reaching the sensitizer. Positive resists are incompletely exposed if considerable solvent remains in the coating. This undersoft-baked positive resist is then readily attacked by the developer in both exposed and unexposed areas, causing less etching resistance.

Note that no post-exposure bake is needed for S1813.

E.4 Developing

The substrate should be swirled for thirty seconds in MF-319 (Microchem). The substrate should then be washed for one minute in DI water. For S1813, exposed resist dissolves, leaving a positive pattern [64]. If resist had been improperly exposed, then the developer will eat away an improper amount of resist. This likewise occurs when under- or overdeveloping. One should also be aware that while the development rate for cross-linked resist is low compared to that for non-cross-lined resist, it is nonetheless non-zero.

E.5 Lift-off

S1813 is simple to remove. Setting the substrate for five minutes in acetone removes the resist. If the resist is still not removed, put the substrate in a sonicator with acetone for an additional five minutes. To remove the acetone, clean the substrate with IPA, DI water, and N_2 (g). Due to harshness on the remaining pattern, sonicating should not be used while removing resist except as a last resort. Sonicating too long may remove metal in addition to resist [64].

Index

B

Biotin, 129, 137, 158

C

Curvatures

- Gaussian, 16
- Mean, 16
- Principal, 16

E

Electronics

- Electroplating supply, 72

Energetics

- Bending, 30
- Bending Modulus, 17
- Energy Landscape, 34
- Escape Rate, 36
- Gaussian bending rigidity, 17
- Helfrich Energy Densities, 17
- Kramers Model, 34
- Loading, 30
- Loading Rate, 36
- P-V, 30
- Stretching, 30
- Two-Barrier Model, 145, 154

Etches

- *Aqua regia*, 75
- Piranha etch, 59, 82
- Potassium gold etch, 73, 83

Exposure

- Alignment Marks, 66
- Over-cutting, 68
- Undercutting, 68
- Weight Error Correction, 66

F

Force Applicators

- Atomic Force Microscopy, 79
- Magnetic, 79
  - Macroscopic Permanent, 43
  - Macroscopic Tweezers, 45, 81
  - Microfabricated Electromagnets, 51, 82

Microfabricated Tweezers, 48, 81, 82
Optical Tweezers, 79
Force ramp, 101
Force threshold, 99

I

Interactions
Electrostatic, 18
Hydrophobic, 18
Steric, 18
Interlayer Drag, 33
Interlayer drag coefficient, 102

L

Laplace-Young Law, 26, 31
Lipid
Biotin-X DHPE, 12, 85, 111, 138, 158, 191
Cholesterol, 8, 17, 25, 136, 191
Fat Acyls, 8
Glycerolipids, 8
Phospholipids, 8
POPC, 10, 85, 191
SOPC, 10, 17, 85, 110, 138, 191, 212
SOPS, 10, 137, 163, 191
Sphingolipids, 8
Sterol Lipids, 8
Lipid Phases
Liquid Disordered, 8
Liquid Ordered, 8
Solid Gel, 8
Lipids
Phospholipids, 10

M

Magnetic Beads
Ferromagnetic, 85, 92, 111
Paramagnetic, 85, 92, 131
Material Properties
List of Densities, ρ, 204
List of Heat Capacities, C_p, 204
List of Power Densities, $\dot{q}$, 204
List of Thermal Conductivities, k,

204

Of Air, 204

Of Glass, 204

Of Gold, 204

Of PDMS, 204

Of Sapphire, 204

Membranes

Magnetic Effects, 211

Thermal Effects, 23, 212

Microaspiration, 86, 212

Microscope Settings, 90

Modeling

Classical, 205

COMSOL, 112

Heaviside Function, 202

Time Average, 215

Modulators

Cholesterol, 136

Tension, 136

Modulus

Bending, 17, 30

Compressibility, 24, 30

Gaussian, 17

P

PDMS

In MFT COMSOL Model, 204

Photoresists, 54, 216

S1813, 216

SU-8 2015, 54, 63, 64, 68, 70, 73, 83, 110

Principle Curvature, 16

R

Receptor-Ligand Interactions, 80, 129, 137, 158

S

Salicylate, 25, 157

Solutions

BSA, 86, 112

PBS, 85

POPC-Biotin-X, 192

SOPC-Biotin-X, 192, 193

100 mM Sucrose, 196

120 mM Dextrose, 196

210 mM glucose, 86, 111

Streptavidin, 85, 91, 111, 129, 137, 158

Systematics

Temperature, 120

Time Threshold, 120

T

Tension, 23, 26, 33, 136